

University of Windsor

Scholarship at UWindor

Electronic Theses and Dissertations

Theses, Dissertations, and Major Papers

2013

Multi-scale Characterization of Hyperplasticity and Failure in Dual Phase Steels Subject to Electrohydraulic Forming

Javad Samei
University of Windsor

Follow this and additional works at: <https://scholar.uwindsor.ca/etd>

Recommended Citation

Samei, Javad, "Multi-scale Characterization of Hyperplasticity and Failure in Dual Phase Steels Subject to Electrohydraulic Forming" (2013). *Electronic Theses and Dissertations*. 4929.
<https://scholar.uwindsor.ca/etd/4929>

This online database contains the full-text of PhD dissertations and Masters' theses of University of Windsor students from 1954 forward. These documents are made available for personal study and research purposes only, in accordance with the Canadian Copyright Act and the Creative Commons license—CC BY-NC-ND (Attribution, Non-Commercial, No Derivative Works). Under this license, works must always be attributed to the copyright holder (original author), cannot be used for any commercial purposes, and may not be altered. Any other use would require the permission of the copyright holder. Students may inquire about withdrawing their dissertation and/or thesis from this database. For additional inquiries, please contact the repository administrator via email (scholarship@uwindsor.ca) or by telephone at 519-253-3000ext. 3208.

Multi-scale Characterization of Hyperplasticity and Failure in Dual Phase Steels Subject to Electrohydraulic Forming

By

Javad Samei

A Dissertation Submitted to the Faculty of Graduate
Studies through Materials Engineering in Partial
Fulfillment of the Requirements for the Degree of
Doctor of Philosophy at the University of Windsor

Windsor, Ontario, Canada

©2013 Javad Samei

Multi-scale Characterization of Hyperplasticity and Failure in Dual Phase Steels Subject to Electrohydraulic Forming

by

Javad Samei

APPROVED BY:

Dr. A.K. Pilkey, External Program Reader
Department of Mechanical and Materials Engineering
Queen's University, ON, Canada

Dr. S. Das, Outside Program Reader
Civil & Environmental Engineering

Dr. S. Golovashchenko, Industrial Advisor
Ford Research and Advanced Engineering, Dearborn, Michigan, USA

Dr. D.O. Northwood, Program Reader
Mechanical, Automotive, & Materials Engineering

Dr. A. Edrisy, Program Reader
Mechanical, Automotive, & Materials Engineering

Dr. V. Stoilov, Co-Advisor
Mechanical, Automotive, & Materials Engineering

Dr. D. Green, Co-Advisor
Mechanical, Automotive, & Materials Engineering

September 6, 2013

Declaration of Co-Authorship and Previous Publication

I hereby declare that this thesis incorporates material that is the result of joint research, as follows:

This dissertation incorporates the outcome of joint research undertaken in collaboration with Dr. Sergey Golovashchenko, Mr. Amir Hassannejdasl and Mr. Iman Sari Sarraf under the supervision of Prof. Dr. Daniel E. Green. The collaboration is covered in Chapters 6 and 7 of the dissertation. As the industrial partner, Dr. Sergey Golovashchenko contributed the electrohydraulic forming of DP500, DP780, and DP980 steel sheets at Ford Research and Advanced Engineering, Dearborn, MI, USA. Mr. Amir Hassannejdasl provided a description of electrohydraulic forming process in terms of mechanical engineering. Also, Mr. Iman Sari Sarraf collaborated in performing hardness tests on DP500 and DP780 steels. In all cases, the key ideas, primary contributions, experimental designs, data analysis and interpretation, were performed by the author.

I am aware of the University of Windsor Senate Policy on Authorship and I certify that I have properly acknowledged the contribution of other researchers to my thesis, and have obtained written permissions from each of the co-authors to include the above materials in my thesis.

I certify that, with the above qualification, this thesis, and the research to which it refers, is the product of my own work.

This dissertation includes two original papers that have been previously published/submitted for publication in peer reviewed journals and two conference proceedings, as follows:

Chapter	Publication title/full citation	Publication status
Chapters 6 and 7	J. Samei, D.E. Green, S. Golovashchenko, A. Hassannejdasl, "Quantitative Microstructural Analysis of Formability Enhancement in Dual Phase Steels Subject to Electrohydraulic Forming", Journal of Materials Engineering and Performance, vol. 22(7), 2013, pp. 2080-2088.	Published
Chapter 7	J. Samei, D.E. Green, S. Golovashchenko, Quantitative Analysis of the Voids in Dual Phase Steel Sheets Formed under Quasi-Static Conditions, Materials Science & Technology, Conference & Exhibition, October 27-31, 2013, Montreal, Quebec Canada	Accepted for publication
Chapter 6	I. Sari Sarraf, J. Samei, D.E. Green, S. Golovashchenko, "Strain Hardening in Dual Phase Steels Formed into a Conical Die Using an Electrohydraulic Forming Process", Materials Science & Technology, Conference & Exhibition, October 27-31, 2013, Montreal, Quebec Canada	Accepted for publication
Chapter 6	J. Samei, D.E. Green, S. Golovashchenko, "Metallurgical Characterization of Hyperplasticity in Dual Phase Steels", Journal of Manufacturing Science and Engineering: ASME.	Submitted on Aug. 26, 2013

I certify that I have obtained written permissions from the copyright owners to include the above published materials in my dissertation. I certify that the above material describes work completed during my registration as graduate student at the University of Windsor.

I declare that, to the best of my knowledge, my dissertation does not infringe upon anyone's copyright nor violate any proprietary rights and that any ideas, techniques, quotations, or any other material from the work of other people included in my dissertation, published or otherwise, are fully acknowledged in accordance with the

standard referencing practices. Furthermore, to the extent that I have included copyrighted material that surpasses the bounds of fair dealing within the meaning of the Canada Copyright Act, I certify that I have obtained a written permission from the copyright owners to include such materials in my dissertation.

I declare that this is a true copy of my dissertation, including any final revisions, as approved by my dissertation committee and the Graduate Studies office, and that this dissertation has not been submitted for a higher degree to any other University or Institution.

Abstract

In this research, three commercial dual phase steel sheets, i.e. DP500, DP780 and DP980, were formed under quasi-static and high strain rate conditions using the Nakazima test and Electrohydraulic Forming (EHF), respectively. In EHF, as a result of a high-voltage electrical discharge between two electrodes in a water chamber, a shock wave was produced which travelled through the water and formed the sheet into the final shape. When a 34° conical die was used in EHF, significant formability improvement, known as hyperplasticity, was achieved in the specimens compared to the specimens formed in the Nakazima test. In this research, hyperplasticity as well as failure in the specimens were characterized at different scales of observation. Quantitative metallography showed relative deformation improvement of around 20% in ferrite and 100% in martensite when formed under EHF. Dislocations in ferrite and deformation twinning in martensite were found to be responsible for the significant improvements of deformation in the constituents under EHF. As a mechanism of failure, voids were found to nucleate in the ferrite/martensite interface due to decohesion. However, under EHF, the significant deformation improvement of martensite enhanced the plastic compatibility between ferrite and martensite. Consequently, the strain gradient across the ferrite/martensite interface, i.e. decohesion, was reduced and nucleation and growth of the interfacial voids was suppressed. Furthermore, quantitative analysis of the voids showed that void growth in the specimens formed under EHF was slower than in the specimens formed in the Nakazima test. The reason was attributed to impact of the sheet against the die that generates significant compressive and shear stresses which act against void growth. Therefore, under EHF, coalescence of the voids to form micro-cracks was postponed to higher levels of strains which resulted in suppression of failure. Fractography of the specimens showed ductile fracture as the dominant type of fracture under both quasi-static and high strain rate forming conditions. In addition, limited quasi-cleavage fracture was observed in DP780 and DP980 specimens. Shear fracture was also observed in the specimens formed under EHF.

Table of Contents

DECLARATION OF CO-AUTHORSHIP AND PREVIOUS PUBLICATION	III
ABSTRACT	VI
LIST OF TABLES	IX
LIST OF FIGURES	X
LIST OF SYMBOLS	XIV
1 INTRODUCTION.....	1
1.1 MOTIVATIONS FOR DUAL PHASE STEELS.....	1
1.2 HIGH STRAIN RATE FORMING OF DUAL PHASE STEELS.....	3
1.3 OBJECTIVE OF THE RESEARCH	5
1.4 THE STRUCTURE OF DISSERTATION	6
2 LITERATURE SURVEY	7
2.1 DUAL PHASE STEELS.....	7
2.1.1 <i>Processing of Dual Phase Steels.....</i>	7
2.1.2 <i>Alloying Elements in Dual Phase Steels.....</i>	10
2.1.3 <i>Microstructure Banding in Dual Phase Steels.....</i>	11
2.1.4 <i>Strengthening Mechanisms of Ferrite in Dual Phase Steels.....</i>	13
2.1.5 <i>Martensite in Dual Phase Steels</i>	17
2.1.6 <i>Yield Behaviour of Dual Phase Steels.....</i>	21
2.1.7 <i>Work Hardening in Dual Phase Steels.....</i>	22
2.1.8 <i>Failure in Dual Phase Steels</i>	24
2.2 HIGH ENERGY RATE FORMING TECHNOLOGIES.....	26
2.2.1 <i>Explosive forming.....</i>	27
2.2.2 <i>Electromagnetic forming</i>	28
2.2.3 <i>Electrohydraulic forming</i>	29
2.3 HYPERPLASTICITY	32
2.3.1 <i>Incremental Sheet Forming.....</i>	32
2.3.2 <i>High Strain Rate Forming.....</i>	33
2.3.3 <i>Mechanisms of Hyperplasticity in High Strain Rate Forming.....</i>	37
2.4 DISLOCATION MOTION IN BCC MATERIALS AT HIGH STRAIN RATE	41
3 EXPERIMENTAL PROCEDURE.....	44
3.1 METAL FORMING PROCEDURE.....	44
3.2 MACRO-STRAIN MEASUREMENT.....	46
3.3 METALLOGRAPHY	47
3.4 QUANTITATIVE METALLOGRAPHY.....	49
3.4.1 <i>Micro-strain Measurement.....</i>	49
3.4.2 <i>Martensite Content.....</i>	50
3.4.3 <i>Analysis of the Voids.....</i>	50
3.5 MICROHARDNESS TEST	51
3.6 FRACTOGRAPHY.....	52

3.7	NANO-SCALE OBSERVATIONS	52
4	MATERIALS CHARACTERIZATION	53
4.1	TENSILE PROPERTIES.....	53
4.2	CHEMICAL COMPOSITION	54
4.3	X-RAY ANALYSIS	56
4.4	GENERAL MICROSTRUCTURE	56
4.5	CARBON CONTENT AND CRYSTALLOGRAPHY OF MARTENSITE.....	61
5	INVESTIGATIONS ON THE FORMABILITY OF NAKAZIMA AND EHF SPECIMENS.....	62
5.1	NAKAZIMA SPECIMENS.....	62
5.2	EHF SPECIMENS	65
5.3	DISTRIBUTION OF EQUIVALENT STRAIN IN THE SPECIMENS	69
6	CHARACTERIZATION OF HYPERPLASTICITY IN DUAL PHASE STEELS.....	73
6.1	MACRO-SCALE CHARACTERIZATION OF HYPERPLASTICITY	74
6.2	MICRO-SCALE CHARACTERIZATION OF HYPERPLASTICITY	78
6.2.1	<i>Micro-strain in Ferrite and Martensite</i>	<i>78</i>
6.2.2	<i>Correlation of Macro-strain and Micro-strains.....</i>	<i>83</i>
6.3	NANO-SCALE CHARACTERIZATION OF HYPERPLASTICITY	86
6.3.1	<i>Bending Contours in TEM Images.....</i>	<i>86</i>
6.3.2	<i>Dislocations under Nakazima test and EHF</i>	<i>90</i>
6.3.3	<i>Deformation Twinning under Nakazima test and EHF</i>	<i>93</i>
6.4	ENHANCED PLASTIC COMPATIBILITY BETWEEN FERRITE AND MARTENSITE IN EHF	96
6.5	CORRELATION OF WORK HARDENING AND HYPERPLASTICITY.....	98
6.6	ADIABATIC SHEAR BANDS	103
7	CHARACTERIZATION OF FAILURE IN DUAL PHASE STEELS SUBJECT TO EHF	104
7.1	NUCLEATION AND GROWTH OF VOIDS	104
7.1.1	<i>Nucleation of Voids due to Cracking of the Martensite Band.....</i>	<i>105</i>
7.1.2	<i>Nucleation of Voids inside the Martensite Islands and Band</i>	<i>105</i>
7.1.3	<i>Nucleation of Voids at the Ferrite/Martensite Interface</i>	<i>106</i>
7.2	QUANTITATIVE ANALYSIS OF THE VOIDS	108
7.3	FRACTOGRAPHY OF DUAL PHASE STEELS SUBJECT TO EHF.....	114
8	CONCLUSIONS.....	120
8.1	MACRO-SCALE CONCLUSIONS.....	120
8.2	MICRO-SCALE CONCLUSIONS.....	121
8.3	NANO-SCALE CONCLUSIONS.....	122
8.4	RECOMMENDATIONS FOR FUTURE RESEARCH.....	123
	REFERENCES	124
	VITA AUCTORIS	139

List of Tables

TABLE 1-1 SIGNIFICANT RESEARCH CONDUCTED ON HIGH STRAIN RATE FORMING OF DUAL PHASE STEELS SINCE 2000	4
TABLE 2-1 EQUILIBRIUM PARTITION RATIOS FOR SOME OF THE ALLOYING ELEMENTS IN STEEL [66]	13
TABLE 2-2 CHARACTERISTICS OF HERF TECHNOLOGIES [136]	31
TABLE 3-1 INPUT VOLTAGE AND CORRESPONDING ENERGY IN EHF TESTS	44
TABLE 3-2 CONDITIONS FOR THE MICROHARDNESS TEST	52
TABLE 4-1 CHARACTERISTICS OF THE AS-RECEIVED DUAL PHASE STEEL SHEETS.....	53
TABLE 4-2 CHARACTERISTICS OF THE AS-RECEIVED DUAL PHASE STEEL SHEETS.....	54
TABLE 6-1 FERRITE GRAIN AND MARTENSITE ISLAND SIZES IN DP500 AND DP780 STEELS AFTER DEFORMATION.....	80

List of Figures

FIGURE 1-1 RELATIONSHIP BETWEEN TOTAL ELONGATION OF STEELS AND (A) YIELD STRENGTH AND (B) ULTIMATE TENSILE STRENGTH. HSS: HIGH STRENGTH STEEL; AHSS: ADVANCED HIGH STRENGTH STEEL; IF: INTERSTITIAL FREE; BH: BAKE HARDENED; HSLA: HIGH STRENGTH LOW ALLOY; TRIP: TRANSFORMATION-INDUCED PLASTICITY; DP: DUAL PHASE; MS: MARTENSITIC STEEL. [4]	2
FIGURE 1-2 ENERGY ABSORPTION OF DUAL PHASE AND TRIP STEELS BELOW 10% STRAIN AS A FUNCTION	2
FIGURE 1-3 ULSAB-AVC: APPLICATION OF DIFFERENT STEELS IN AUTOBODY STRUCTURE [5].....	3
FIGURE 2-1 SCHEMATIC PRESENTATION OF THE STEEL MICROSTRUCTURE IN HYPOEUTECTIC REGION OF Fe-Fe ₃ C PHASE DIAGRAM [46].....	8
FIGURE 2-2 MICROSTRUCTURE OF DUAL PHASE STEEL PRODUCED BY (A) INTERCRITICAL ANNEALING AND (B) SEQUENTIAL QUENCHING METHODS [48].....	9
FIGURE 2-3 MANGANESE ENRICHMENT IN A MARTENSITE PARTICLE AFTER AUSTENITE TO MARTENSITE TRANSFORMATION [49].....	10
FIGURE 2-4 MICROSTRUCTURE BANDING IN DUAL PHASE STEEL (015C–2.0Mn–0.2Si); AUSTENITIZING AT 875 °C FOR 1 H, FURNACE COOLING TO 720 °C (3 K MIN ⁻¹), WATER QUENCHING [30]	12
FIGURE 2-5 VARIATION OF STRAIN HARDENING RATE AS A FUNCTION OF FERRITE GRAIN SIZE IN DUAL PHASE STEELS WITH DIFFERENT MARTENSITE CONTENTS (A) A ₁ –A ₆ : F _M ≈0.25, (B) B ₁ –B ₆ : F _M ≈0.35, AND (C) C ₁ –C ₆ : F _M ≈0.45 [75].....	15
FIGURE 2-6 DISLOCATION SUBSTRUCTURE IN FERRITE GRAINS OF A C-MN-SI DUAL PHASE STEEL FORMED UNDER QUASI-STATIC UNIAXIAL TENSILE TEST. DISLOCATION TANGLES AT (A) E=0.01 AND (B) E=0.02, AND DISLOCATION CELLS AT (C) E=0.07 AND (D) E=0.14. [76].....	16
FIGURE 2-7 (A) LATTICE PARAMETERS OF MARTENSITE VERSUS CARBON CONTENT OF MARTENSITE IN Fe-C STEELS [78], AND (B) TETRAGONALITY OF MARTENSITE AS A FUNCTION OF CARBON CONTENT [79]	17
FIGURE 2-8 HARDNESS OF MARTENSITIC STEEL AS A FUNCTION OF CARBON CONTENT [80]	18
FIGURE 2-9 EFFECT OF CARBON CONTENT ON M _S TEMPERATURE IN STEELS [81].....	19
FIGURE 2-10 UPPER AND LOWER YIELD STRENGTH OF MARTENSITE AS A FUNCTION OF CARBON CONTENT [59]	19
FIGURE 2-11 MOBILE DISLOCATIONS IN THE VICINITY OF FERRITE/MARTENSITE INTERFACE CAUSES CONTINUOUS YIELDING BEHAVIOUR OF DUAL PHASE STEELS [99]	22
FIGURE 2-12 TRUE STRESS-STRAIN CURVE OF A FERRITE-MARTENSITE STEEL WITH 1.5 WT% Mn AND DIFFERENT CARBON CONTENTS ANNEALED AT 760 °C [10]	23
FIGURE 2-13 CRUSSARD-JAOUL PLOT OF SEVERAL DUAL PHASE STEELS [119].....	24
FIGURE 2-14 TRUE FRACTURE STRAINS OF DUAL PHASE STEELS WITH 0.066-0.13% CARBON WITH DIFFERENT MARTENSITE VOLUME FRACTION AND SIZE [15].....	26
FIGURE 2-15 TYPICAL EXPLOSIVE FORMING OPERATIONS. (A) SIZING WITH A WATER-FILLED DIE CAVITY, (B) FOR FORMING A FLAT PANEL, (C) USE OF DETONATION CORD TO PRESCRIBE THE PRESSURE DISTRIBUTION IN AN OPEN FORMING SYSTEM, AND (D) USE OF DETONATION CORD TO FORM A CYLINDER [135]	27
FIGURE 2-16 BASIC CIRCUIT AND MAGNETIC FIELD PATTERNS FOR ELECTROMAGNETIC COMPRESSION FORMING OF A TUBULAR WORKPIECE, (A) FIELD PATTERN IN ABSENCE OF WORKPIECE, (B) FIELD PATTERN WITH WORKPIECE IN FORMING COIL, AND (C) FIELD PATTERN WHEN FIELD SHAPER IS USED. A, HIGH PRESSURE; B, LOW PRESSURE.[135]	28
FIGURE 2-17 SCHEMATIC ELECTROHYDRAULIC FORMING SETUP (A) UNDER FREE-FORMING, AND (B) INSIDE A CONICAL DIE [148]	30
FIGURE 2-18 INCREMENTAL SHEET FORMING PROCESS, (A) SPIF, (B) SPIF WITH COUNTER TOOL, (C) TPIF WITH A PARTIAL DIE, AND (D) TPIF WITH A FULL DIE. [150]	32

FIGURE 2-19 FORMED SPECIMENS OF (A) AL 6061 T4 [178], (B) OFHC COPPER[178], AND (C) IRON [177], UNDER QUASI-STATIC (LEFT) AND HIGH STRAIN RATE CONDITIONS USING ELECTROHYDRAULIC FORMING (RIGHT)	34
FIGURE 2-20 FORMING LIMIT DIAGRAMS OF (A) AL 6061 T4 [181], (B) OFHC COPPER [182] AT LOW AND HIGH STRAIN RATES. FORMABILITY IMPROVEMENT WAS OBSERVED IN HIGH STRAIN RATE FORMING.....	35
FIGURE 2-21 FORMING LIMIT DIAGRAMS OF (A) AL 6061 T6, AND (B) AISI 1045 STEEL AT LOW AND HIGH STRAIN RATES [183]. FORMABILITY IMPROVEMENT WAS OBSERVED IN HIGH STRAIN RATE FORMING.	36
FIGURE 2-22 OPTICAL MICROGRAPHS OF SHEAR ZONES IN S15C STEEL SPECIMENS FORMED AT (C) $5.0 \times 10^4 \text{ s}^{-1}$ AND (D) $2.0 \times 10^5 \text{ s}^{-1}$	41
FIGURE 2-23 DEPENDENCE OF THE LOWER YIELD STRESS ON THE STRAIN RATE IN A 0.12 WT% C STEEL [230].....	43
FIGURE 3-1 SCHEMATIC OF THE NAKAZIMA TEST	45
FIGURE 3-2 SCHEMATIC OF EHF PROCESS.....	45
FIGURE 3-3 ELONGATED CIRCLES ON THE SPECIMENS USED FOR DETERMINATION OF MAJOR AND MINOR STRAINS.	46
FIGURE 3-4 (A) THE PATTERN OF CUTTING THE SAMPLES FOR METALLOGRAPHY, AND (B) MOUNTING OF THE THREE SAMPLES OF THE SAME REGION INTO ONE DIE.	48
FIGURE 3-5 SEQUENCE FOR THE QUANTITATIVE ANALYSIS OF VOIDS, 1: MICROGRAPH OF TD PART, 2: ENHANCEMENT OF CONTRAST OF THE MICROGRAPH, 3: MICROGRAPH IN THE IMAGE ANALYSIS SOFTWARE	51
FIGURE 3-6 FRACTOGRAPHY OF THE SPECIMEN AT DIFFERENT MAGNIFICATIONS.....	52
FIGURE 4-1 DISTRIBUTION OF SOME ALLOYING ELEMENTS IN DP780 CAPTURED BY X-RAY MAPPING	55
FIGURE 4-2 X-RAY DIFFRACTION PATTERNS OF THE DUAL PHASE STEELS INCLUDE FERRITE AND MARTENSITE PEAKS.....	57
FIGURE 4-3 MICROSTRUCTURE OF DP500: (A) NORMAL DIRECTION, AND (B) THROUGH THICKNESS. THE DARKER PHASE IS FERRITE AND THE LIGHT GRAY PHASE IS MARTENSITE. SMALL PARTICLES OF CARBIDES ARE DISTRIBUTED IN FERRITE GRAINS.	58
FIGURE 4-4 MICROSTRUCTURE OF DP780: (A) NORMAL DIRECTION, AND (B) THROUGH THICKNESS. THE DARKER PHASE IS FERRITE AND THE LIGHT GRAY PHASE IS MARTENSITE. SMALL PARTICLES OF CARBIDES ARE DISTRIBUTED IN FERRITE GRAINS.	59
FIGURE 4-5 MICROSTRUCTURE OF DP980: (A) NORMAL DIRECTION, AND (B) THROUGH THICKNESS. THE DARKER PHASE IS FERRITE AND THE LIGHT GRAY PHASE IS MARTENSITE. SMALL PARTICLES OF CARBIDES ARE DISTRIBUTED IN FERRITE GRAINS.	60
FIGURE 5-1 NAKAZIMA SPECIMENS FORMED WITHOUT LUBRICANT: (A) DP500, (B) DP780, AND (C) DP980. THE ROLLING DIRECTION AND CRACKING ARE SHOWN BY THE RED AND BLUE ARROWS, RESPECTIVELY.	63
FIGURE 5-2 NAKAZIMA SPECIMENS FORMED WITH LUBRICANT: (A) DP500, (B) DP780, AND (C) DP980. THE ROLLING DIRECTION AND CRACKING ARE SHOWN BY THE RED AND BLUE ARROWS, RESPECTIVELY.	64
FIGURE 5-3 SPECIMENS FORMED UNDER EHF USING THE CONICAL DIE SHOWING A CRACK ON THE TIP OF THE CONE: (A) DP500 FORMED AT 8.0 kV, (B) DP780 FORMED AT 13.4 kV, AND (C) DP980 FORMED AT 13.3 kV. THE ROLLING DIRECTION IS SHOWN BY THE BLUE ARROW.....	66
FIGURE 5-4 SPECIMENS FORMED UNDER EHF USING THE CONICAL DIE SHOWING REBOUNDING ON THE TIP OF THE CONE: (A) DP500 FORMED AT 9.5 kV, (B) DP780 FORMED AT 13.4 kV, AND (C) DP980 FORMED AT 13.7 kV. THE ROLLING DIRECTION IS SHOWN BY THE BLUE ARROW.....	67
FIGURE 5-5 (A) DP500 AND (B) DP780 SPECIMENS FORMED UNDER EHF WITHOUT USING A DIE.	68
FIGURE 5-6 DISTRIBUTION OF EFFECTIVE STRAIN ACROSS THE DIAMETER OF THE SPECIMENS IN ROLLING DIRECTION: DP500 FORMED UNDER (A) NAKAZIMA TEST, (B) EHF.....	70
FIGURE 5-7 DISTRIBUTION OF EFFECTIVE STRAIN ACROSS THE DIAMETER OF THE SPECIMENS IN ROLLING DIRECTION: DP780 FORMED UNDER (A) NAKAZIMA TEST, (B) EHF.....	71

FIGURE 5-8 DISTRIBUTION OF EFFECTIVE STRAIN ACROSS THE DIAMETER OF THE SPECIMENS IN ROLLING DIRECTION: DP980 FORMED UNDER (A) NAKAZIMA TEST, (B) EHF.....	72
FIGURE 6-1 (A) TRUE MAJOR VS. MINOR STRAIN ACROSS THE DP500 SPECIMENS, AND (B) QUASI-STATIC FORMING LIMIT DIAGRAM OF THE DP500 INCLUDING THE GREATEST SAFE ENGINEERING STRAIN IN DP500 FORMED UNDER EHF USING A CONICAL DIE. THE QUASI-STATIC FLD IS REPORTED BY GOLOVASHCHENKO ET AL. [236]	75
FIGURE 6-2 (A) TRUE MAJOR VS. MINOR STRAIN ACROSS THE DP780 SPECIMENS, AND (B) QUASI-STATIC FORMING LIMIT DIAGRAM OF THE DP780 INCLUDING THE GREATEST SAFE ENGINEERING STRAIN IN DP780 FORMED UNDER EHF USING A CONICAL DIE. THE QUASI-STATIC FLD IS REPORTED BY GOLOVASHCHENKO ET AL. [236]	76
FIGURE 6-3(A) TRUE MAJOR VS. MINOR STRAIN ACROSS THE DP980 SPECIMENS, AND (B) QUASI-STATIC FORMING LIMIT DIAGRAM OF THE DP980 INCLUDING THE GREATEST SAFE ENGINEERING STRAIN IN DP980 FORMED UNDER EHF USING A CONICAL DIE. THE QUASI-STATIC FLD IS REPORTED BY GOLOVASHCHENKO ET AL. [236]	77
FIGURE 6-4 TRUE MAJOR VS. MINOR MICRO-STRAINS IN (A) MARTENSITE ISLANDS, AND (B) FERRITE GRAINS; FROM THE EDGE TO THE CENTRE OF THE SPECIMENS FORMED UNDER QUASI-STATIC AND HIGH STRAIN RATE CONDITIONS. NOTE THAT THE VOLUME FRACTION OF MARTENSITE IN DP500 AND DP780 WAS 10% AND 23%, RESPECTIVELY.....	81
FIGURE 6-5 (A) THE GREATEST TRUE MAJOR VS. MINOR MICRO-STRAINS OF THE CONSTITUENTS IN THE SAFE ZONE OF THE SPECIMENS, AND (B) RELATIVE DEFORMATION IMPROVEMENT OF THE CONSTITUENTS UNDER EHF.....	82
FIGURE 6-6 TRUE MACRO AND MICRO MINOR VS. MAJOR STRAINS IN DP500 AND DP780 UNDER (A) QUASI-STATIC AND (B) EHF CONDITIONS.....	84
FIGURE 6-7 DP780 STEEL FORMED UNDER EHF (A) SAFE MARTENSITE ISLANDS IN THE VICINITY OF THE MARTENSITE BAND AND (B) NANO-SCALE VOIDS IN THE MARTENSITE BAND.	85
FIGURE 6-8 BRIGHT FIELD IMAGE OF A BEND CONTOUR IN A BUCKLED SPECIMEN [239].....	86
FIGURE 6-9 BEND CONTOURS IN DP500 FORMED IN THE (A) NAKAZIMA TEST, AND (B) IN EHF.....	87
FIGURE 6-10 BEND CONTOURS IN DP780 FORMED IN THE (A) NAKAZIMA TEST, AND (B) IN EHF.	88
FIGURE 6-11 BEND CONTOURS IN DP980 FORMED IN THE (A) NAKAZIMA TEST, AND (B) IN EHF.	89
FIGURE 6-12 DP780 NAKAZIMA SPECIMEN: (A) ACCUMULATION OF DISLOCATIONS SHOWN BY “X” AT THE FERRITE/MARTENSITE INTERFACE, AND (B) DISLOCATION CELLS IN THE VICINITY OF FERRITE/MARTENSITE INTERFACE.	90
FIGURE 6-13 EVOLUTION OF STRAIN RATE ACROSS A DP590 SPECIMEN FORMED UNDER EHF USING THE 34° CONICAL DIE. R IS THE RADIAL DISTANCE FROM THE SYMMETRY AXIS IN MM [236].	92
FIGURE 6-14 DISLOCATION MULTIPLICATION INSIDE A FERRITE GRAIN IN (A) AND (B) DP500, AND (C) AND (D) DP780, FORMED IN EHF PROCESS.	93
FIGURE 6-15 DEFORMATION TWINNING IN MARTENSITE DEFORMED BY EHF IN (A) DP780, AND (B) DP980. THE SAD IS SHOWN BY THE YELLOW BOX.	95
FIGURE 6-16 PLASTIC DEFORMATION IN SPECIMENS AT APPROXIMATELY 0.30 STRAIN: (A) DP980-EHF, (B) DP980-NAKAZIMA, (C) DP500-EHF, AND (D) DP780-EHF.	96
FIGURE 6-17 (A) CONICAL SPECIMEN FORMED BY EHF, AND MARTENSITE TO FERRITE (B) MINOR AND (C) MAJOR STRAIN RATIO UNDER QUASI-STATIC (QS) AND HIGH STRAIN RATE (EHF) FORMING CONDITIONS. NOTE THAT THE VOLUME FRACTION OF MARTENSITE IN DP500 AND DP780 WAS 10% AND 23%, RESPECTIVELY.	98
FIGURE 6-18 HARDNESS OF FERRITE IN DP500 AS A FUNCTION OF EFFECTIVE STRAIN. THE ARROW SHOWS THE INFLECTION POINT OF THE HARDNESS CURVE AT WHICH THE HARDNESS RATE STARTED TO INCREASE IN EHF.	100
FIGURE 6-19 HARDNESS OF FERRITE IN DP780 AS A FUNCTION OF EFFECTIVE STRAIN. THE ARROW SHOWS THE INFLECTION POINT OF THE HARDNESS CURVE AT WHICH THE HARDNESS RATE STARTED TO INCREASE IN EHF.	100
FIGURE 6-20 HARDNESS OF FERRITE IN DP980 AS A FUNCTION OF EFFECTIVE STRAIN. THE ARROW SHOWS THE INFLECTION POINT OF THE HARDNESS CURVE AT WHICH THE HARDNESS RATE STARTED TO INCREASE IN EHF.	101

FIGURE 6-21 INCREASE IN HARDNESS OF FERRITE GRAINS IN DUAL PHASE STEELS UP TO AN EQUIVALENT STRAIN OF 0.20 (MM/MM).	101
FIGURE 6-22 HARDNESS OF DUAL PHASE STEELS FORMED BY EHF AS A FUNCTION OF EFFECTIVE STRAIN. ARROWS SHOW THE INCREASE IN THE HARDNESS OF THE STEELS DUE TO THE NUCLEATION OF DISLOCATIONS.	103
FIGURE 7-1 NUCLEATION OF VOIDS AS A RESULT OF CRACKING AND SEPARATION IN THE MARTENSITE BANDS IN (A) DP500, AND (B) DP780 NAKAZIMA SPECIMENS, AND (C) DP500, AND (D) DP780 EHF SPECIMENS.....	105
FIGURE 7-2 VOIDS INSIDE MARTENSITE ISLANDS IN (A) DP500 FORMED BY EHF, (B) DP780 FORMED BY EHF, (C) DP980 BY THE NAKAZIMA TEST, AND (D) DP980 FORMED BY EHF.....	106
FIGURE 7-3 TEM IMAGE OF DP780 SPECIMEN FORMED BY EHF. DISLOCATION ACCUMULATION AT THE FERRITE/MARTENSITE INTERFACE RESULTED IN LOCAL STRAIN GRADIENT AND DECOHESION AT THE INTERFACE. AS A RESULT OF DECOHESION, NUCLEATION AND GROWTH OF NANO-VOIDS OCCURRED.	107
FIGURE 7-4 MICRO-CRACKS AT THE FERRITE/MARTENSITE INTERFACE OF (A) DP780 NAKAZIMA SPECIMENS, (B) DP780 EHF SPECIMEN, AND (C) DP980 NAKAZIMA SPECIMENS.	108
FIGURE 7-5 VOIDS IN DP500 EHF SPECIMEN AT STRAIN: (A) 0.1, (B) 0.2, (C) 0.3, (D) 0.4, (E) 0.5, AND (F) 0.6 (MM/MM). BLACK SPOTS ARE THE VOIDS IN THE WHITE MATRIX.	109
FIGURE 7-6 VOID VOLUME FRACTION AS A FUNCTION OF STRAIN IN (A) DP500, (B) DP780, AND (C) DP980, FORMED IN A NAKAZIMA TEST (QS) AND BY EHF.	111
FIGURE 7-7 VOID AREA AS A FUNCTION OF STRAIN IN (A) DP500, (B) DP780, AND (C) DP980, FORMED IN A NAKAZIMA TEST (QS) AND BY EHF.....	112
FIGURE 7-8 DUCTILE FRACTURE IN (A) DP500, AND (B) DP780 FORMED IN THE NAKAZIMA TEST.	115
FIGURE 7-9 DUCTILE FRACTURE IN DP980 FORMED IN THE NAKAZIMA TEST (A) GENERAL VIEW, AND (B), (C), AND (D) DETACHED MARTENSITE ISLANDS.	116
FIGURE 7-10 DUCTILE FRACTURE IN (A) DP500, (B) DP780, AND (C) DP980 FORMED BY EHF.	117
FIGURE 7-11 QUASI-CLEAVAGE FRACTURE IN DP780 FORMED IN THE (A) NAKAZIMA TEST, AND (B) BY EHF.	118
FIGURE 7-12 SHEAR FRACTURE IN (A) DP500, (B) DP500 WITH GREATER MAGNIFICATION, (C) DP780, AND (D) DP980 FORMED BY EHF.....	119

List of Symbols

%RA	Relative Accuracy percent
<i>b</i>	Burgers vector
<i>C%</i>	carbon content of dual phase steel
<i>C_F</i>	carbon content of ferrite
<i>CI</i>	Confidence Intervals
<i>C_L</i>	solute concentration in liquid
<i>C_M</i>	carbon content of martensite
<i>C_S</i>	solute concentration in solid
<i>d</i>	grain size
<i>d_{as-rolled}</i>	diameter of ferrite grain or martensite island before forming
<i>d_{avg}</i>	average of the two pyramidal lengths in Vickers hardness test
<i>d_f</i>	diameter of ferrite grain of martensite island after forming
<i>d_{Major}</i>	diameter of circles in major direction
<i>d_{Minor}</i>	diameter of circles in minor direction
<i>e</i>	engineering strain
<i>ε</i>	true strain
<i>ε_{Major}</i>	major strain
<i>ε_{Minor}</i>	minor strain
<i>e_T</i>	engineering through-thickness strain
<i>ε_T</i>	true through-thickness strain
<i>ε̇</i>	strain rate
<i>ε̄</i>	von Mises effective strain
<i>F</i>	force
<i>G</i>	shear modulus
<i>H</i>	hardness
<i>HV</i>	Vickers hardness
<i>k</i>	equilibrium partition ratio

M	Taylor factor
m	strain rate sensitivity
m^*	orientation factor
M_S	martensite start temperature
n	strain hardening exponent
N	number of the measured grains
s	standard deviation
$T_{as-rolled}$	thickness of as-rolled sheet
T_f	thickness of formed specimen
v	dislocation velocity
V_F	volume fraction of ferrite
V_M	volume fraction of martensite
Δx	the average dislocation displacement
ρ	dislocation density
$\dot{\rho}$	the rate of increase of the dislocation density
σ	flow stress
σ_0	friction stress opposing the movement of dislocations
σ_{DSL}	flow stress associated with dislocation density
σ_{SSS}	flow stress associated with solid solution strengthening
σ_y	yield strength
τ_{PN}	Peierls-Nabarro shear stress
$\dot{\gamma}$	shear strain rate
\bar{X}	mean size of the grain

CHAPTER 1

1 Introduction

1.1 Motivations for Dual Phase Steels

Dual phase steels were introduced during the 1960s [1]; however, there was no notable industrial application for them until the 1970s. During the 1970s, the oil crisis encouraged researchers to do comprehensive research on reducing the weight of vehicles in order to decrease fuel consumption. Since a significant portion of the total weight of a vehicle is made of steel, an effective way to reduce the weight of the body was to use thinner steel sheets without compromising strength and crashworthiness. Reducing the gauge of sheet metal components and simultaneously preserving the safety of vehicles demanded a grade of steel with greater combination of strength and formability. These criteria made dual phase steels an ideal substitute for conventional steels due to their superior combination of strength and ductility compared to the precipitation hardened and solid solution hardened steels [2].

The advantages of dual phase steels can be seen in Figure 1-1 which shows the relationship between yield and ultimate tensile strength and elongation for different steels. As can be seen, dual phase steels and transformation-induced plasticity (TRIP) steels show a wide range of strength and ductility. During a car crash, the maximum allowable deformation is considered to be 10% strain [3]. Hence, the energy absorption of the automotive body at 10% strain is an important parameter. Figure 1-2 shows that, compared to the TRIP steels with the same strength, dual phase steels have greater energy absorption at 10% strain. This means that the application of dual phase steels can enhance the safety of the cars in case of accidents. The significant implementation

of dual phase steels in autobody structures is reported by UltraLight Steel Auto Body (ULSAB-a consortium of steel producers and cars manufactures from around the world) for 2009 and can be seen in Figure 1-3.

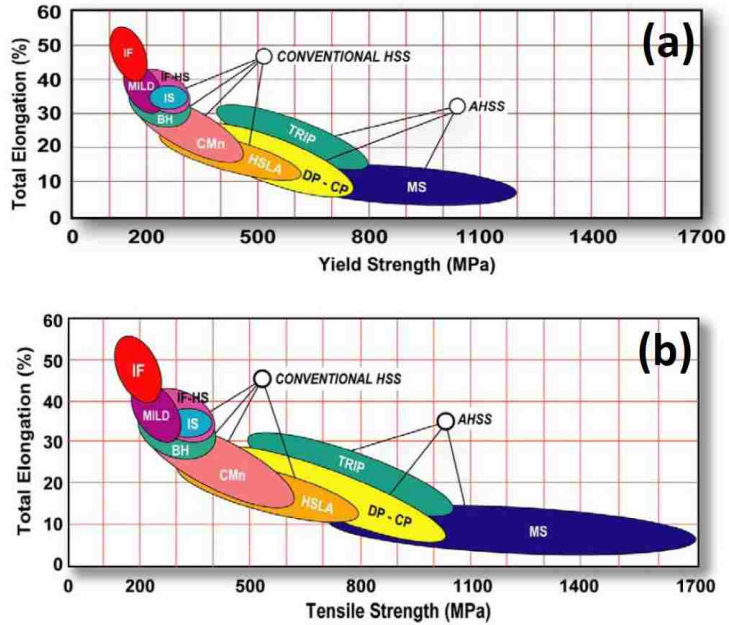


Figure 1-1 Relationship between total elongation of steels and (a) yield strength and (b) ultimate tensile strength. HSS: high strength steel; AHSS: advanced high strength steel; IF: interstitial free; BH: bake hardened; HSLA: high strength low alloy; TRIP: transformation-induced plasticity; DP: dual phase; MS: martensitic steel. [4]

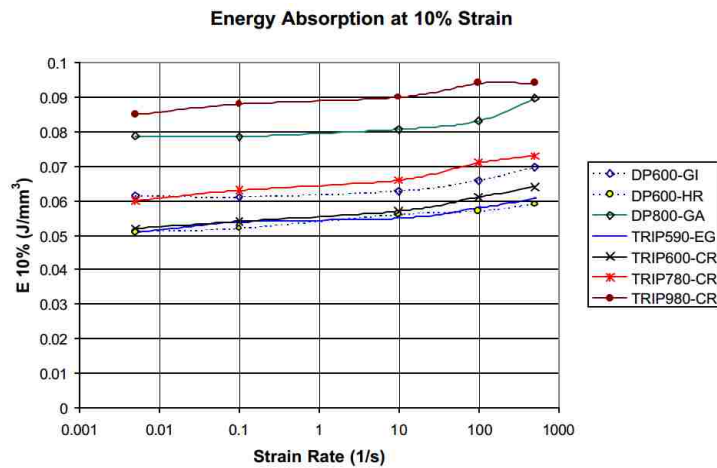


Figure 1-2 Energy absorption of dual phase and TRIP steels below 10% strain as a function of strain rate [3]

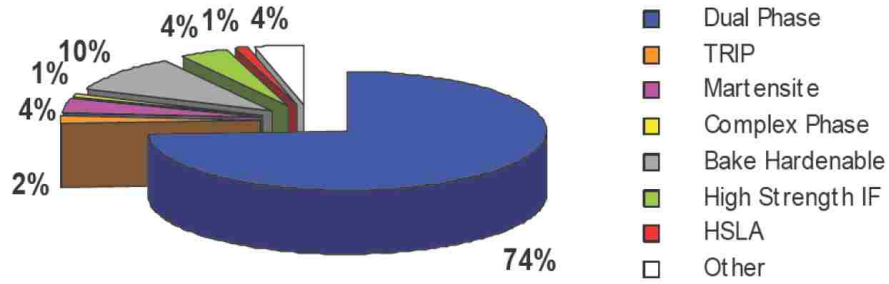


Figure 1-3 ULSAB-AVC: application of different steels in autobody structure [5]

Several studies were carried out during the 1970s and 1980s on the processing, microstructure-properties relationship, and specially the deformation of dual phase steels. Davies et al. [6-9], Speich et al. [10-13], Balliger et al. [14, 15], Cai et al. [16, 17], Marder et al. [18-20], Geol et al. [21] Kim et al. [22], Lanzillotto et al. [23], and Ramos et al. [24] made great contributions toward the development of dual phase steels. In regards to the metal forming industry, in addition to a superior combination of strength and ductility, dual phase steel sheets attracted more attention due to their specific characteristics such as continuous yielding [25, 26], low yield to tensile strength ratio accompanied with a high initial work hardening rate [9, 27], and remarkably high uniform tensile elongation.

1.2 High Strain Rate Forming of Dual Phase Steels

Nowadays, there is a global endeavor to mass-produce vehicles with lower fuel consumption in the most economical manner. This objective cannot be achieved using conventional metal forming technologies. This issue motivates the automotive industry to develop new metal forming technologies, not only to reduce the costs and increase manufacturing productivity but also to be able to form thinner sheets to reduce the weight of vehicles. One approach is to industrialize high energy rate forming (HERF) technologies such as explosive forming, electromagnetic forming, and electrohydraulic forming that can provide high strain rate forming conditions. As it will be discussed in Section 2.3, under certain high strain rate forming conditions, significant formability improvements can be achieved with dual phase steel sheets. Therefore, application of

dual phase steels and the development of suitable HREF technologies for industrial applications, can lead to rapid manufacturing of safe vehicles with lighter weight and reasonable price. As presented in Table 1-1, there have been many investigations conducted since 2000 on the characterization of dual phase steels under high strain rate forming. Most of these research efforts were carried out in the strain rate range of 10^2 - 10^3 s^{-1} using Split Hopkinson Bar and high speed tensile test equipment under controlled states of stress. A limited number of reports studied microstructural aspects of high strain rate deformation of dual phase steels under torsion [28-31] and compression [32].

Table 1-1 Significant research conducted on high strain rate forming of dual phase steels since 2000

Reference	Materials	Forming Condition	Strain Rate Range
2000 [33]	Dual Phase Steels	High Speed Tensile Test	$1300 s^{-1}$
2000 [34]	DP600, DP800, and DP1000 Steels	High Speed Tensile Test	$200 s^{-1}$
2000, 2004, 2005 [28-30]	Dual Phase Steels	Dynamic Torsion	$1750 s^{-1}$
2005 [35, 36]	Dual Phase Steels	High Speed Tensile Test	10^{-3} - $10^3 s^{-1}$
		Servo-hydraulic High Rate Impact	$100 s^{-1}$
2007 [32]	Dual Phase Steels	Split Hopkinson Pressure Bar	2500 - $5100 s^{-1}$
2008 [37]	DP600 and DP800 Steels	High Speed Tensile Test	$200 s^{-1}$
2008 [31]	Dual Phase Steels with Bainite and Martensite	Split Hopkinson Bar in Shear Mode	$2000 s^{-1}$
2008 [38]	Dual Phase Steels	Split Hopkinson Tension Bar	150 - $600 s^{-1}$
		Servo-hydraulic Testing Machine	$100 s^{-1}$
2009 [39]	DP600 Steel	High Speed Tensile Test	500, 1100 and $1600 s^{-1}$
2011 [40]	DP590 Steel	High Speed Tensile Test	$100 s^{-1}$
2013 [41]	DP600, DP800, DP1000 Steels	Split Hopkinson Tensile Bar	Up to $1250 s^{-1}$

1.3 Objective of the Research

In this research, both quasi-static and high strain rate forming conditions were applied to form dual phase steel sheets using the Nakazima test [42] and electrohydraulic forming (EHF) [43], respectively. Compared to high speed tensile tests and general Split Hopkinson Bar tests, the challenge with electrohydraulic forming is attributed to the complex state of stress at higher strain rates that can reach the order of 10^4 s^{-1} . This makes electrohydraulic forming of dual phase steels an interesting research area in terms of multi-scale characterization of deformation and failure in different grades of dual phase steels.

During some preliminary investigations, a significant formability improvement, i.e. hyperplasticity, was observed in dual phase steel specimens formed under EHF using a conical die compared to the specimens formed under quasi-static forming conditions using the Nakazima test. Hence, dual phase steel sheets exhibited a notably different behaviour under the different forming conditions.

The goal of this research is to characterize the behaviour of DP500, DP780, and DP980 steel sheets under EHF in terms of mechanisms of deformation and failure. The main guidelines of the research can be summarized as follows:

- 1- Quantitative analysis of macro and micro-scale deformation in the specimens.
- 2- Investigation on the deformation mechanisms in ferrite and martensite phases.
- 3- Study of plastic compatibility between ferrite and martensite.
- 4- Characterization of work hardening in the specimens.
- 5- Observation of void nucleation and growth, and formation of micro-cracks.
- 6- Quantitative analysis of the voids.
- 7- Fractography of the specimens.

1.4 The Structure of Dissertation

A brief description of the contents of each chapter is presented in the following:

Chapter 2: presents a literature review on the processing, mechanical metallurgy, and mechanisms of failure of dual phase steels. Also, high energy rate forming technologies as well as hyperplasticity of materials under high strain rate forming are described in this chapter.

Chapter 3: describes the experimental procedures that were carried out during the research.

Chapter 4: presents tensile properties, chemical composition, and microstructure characteristics of the commercial dual phase steels investigated in this research.

Chapter 5: exhibits the results of preliminary macro-scale investigations on the formed specimens. General appearance of the specimens, different types of failure, and distribution of effective strain across the specimens are presented in this chapter.

Chapter 6: describes and discusses the macro, micro, and nano-scale investigations on occurrence and mechanisms of hyperplasticity in dual phase steel sheets formed under EHF.

Chapter 7: describes and discusses the mechanisms of failure and fracture in the specimens formed under Nakazima test and EHF.

Chapter 8: presents a summary and conclusions of this research. Also, some recommendations for future research are suggested in this chapter.

CHAPTER 2

2 Literature Survey

2.1 Dual Phase Steels

2.1.1 Processing of Dual Phase Steels

During the 1970s, it was found that ferrite-martensite steels with enhanced combination of strength and ductility could be produced by intercritical annealing of carbon steel followed by rapid cooling down to room temperature. These steels were called dual phase steels. Nowadays, dual phase steels are mostly used in the form of sheets in the automotive industry. Processing of dual phase steel sheets is a combination of rolling and heat treatment. As described in the following, there are two common methods for processing dual phase steels which result in different microstructures and properties.

Sequential quenching First of all, the initial steel is hot rolled to reach the desired thickness. During hot rolling, the microstructure of the steel contains ferrite and pearlite. After hot rolling, the steel is heated in the austenite region of the Fe-Fe₃C phase diagram which is shown in Figure 2-1. Then, the temperature of the steel is reduced to the intercritical temperature in the $\alpha+\gamma$ region. During the holding time, ferrite nucleates at the austenite grain boundaries and grows into the austenite grains. To obtain a homogeneous microstructure, the temperature of the steel must become uniform during the holding time otherwise the centre of the sheet may remain austenitic while the edge is in $\alpha+\gamma$ region. After a sufficient holding time, quenching of

the steel transforms the austenite to martensite and a dual phase sheet is produced [44, 45].

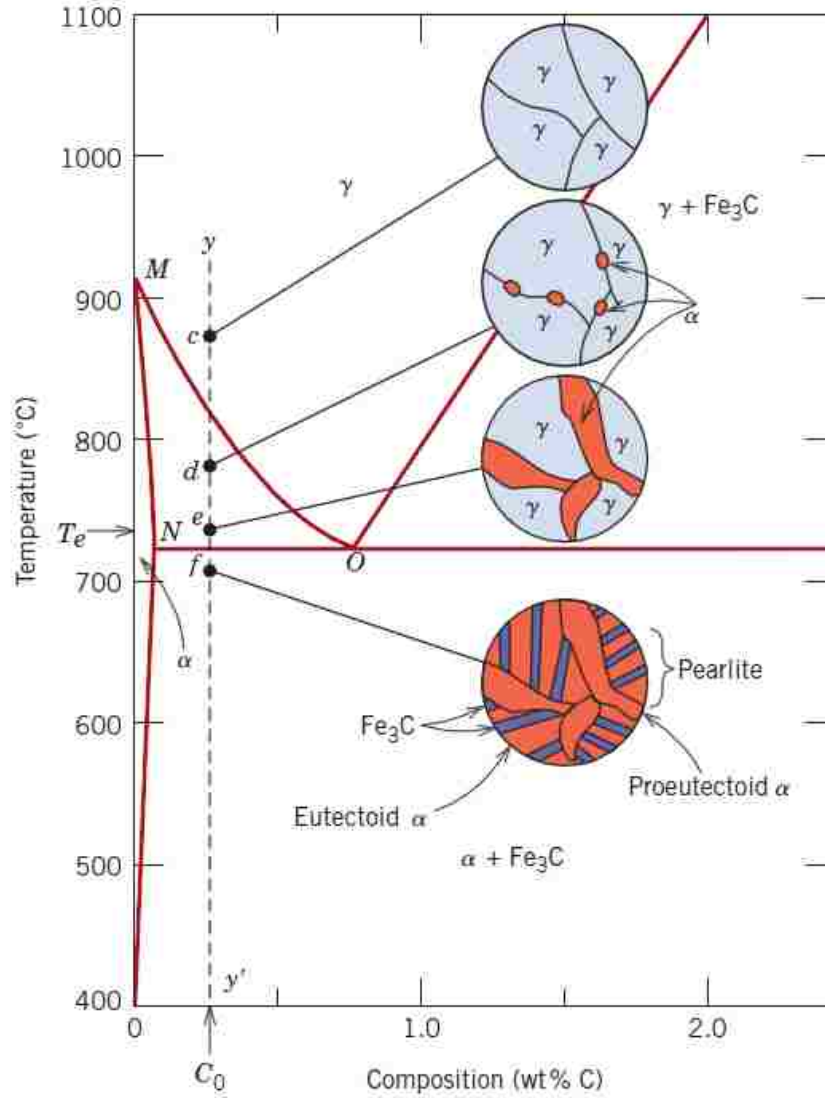


Figure 2-1 Schematic presentation of the steel microstructure in hypoeutectic region of Fe-Fe₃C phase diagram [46]

Intercritical annealing The intercritical annealing method is usually associated with galvanizing [47]. In this method, the steel sheet with the ferrite-pearlite microstructure is cold rolled to the desired thickness. Since the dimensional accuracy after cold rolling is better than after hot rolling, industrial dual phase steel sheets are processed using intercritical annealing in the $\alpha+\gamma$ phase region. Under equilibrium conditions, heat

treatment of dual phase steel under intercritical annealing method contains four stages [48-51]: first, dissolution of pearlite at the ferrite/carbide interfaces to form austenite with eutectoid composition; second, growth of austenite along grain boundaries into the ferrite up to the equilibrium composition at the annealing temperature; and third, homogenization of alloying elements by diffusion through the austenite grains; and finally, martensite is produced by quenching the sheet from the intercritical temperature to room temperature. However, due to economic realities, equilibrium phase transformation is not generally attained in industrial conditions. Hence, other phases or structures such as bainite may exist in the microstructure.

In both methods, the fraction of austenite that transforms to martensite depends on the cooling rate, the chemical composition of the austenite, and the size and dispersion of austenite particles [52]. Figure 2-2 shows the microstructures of dual phase steels produced by intercritical annealing and sequential quenching. Large martensite islands at the grain boundaries of coarse ferrite grains is produced in the sequential quenching technique while finer martensite islands and ferrite grains are obtained with the intercritical annealing method [48].

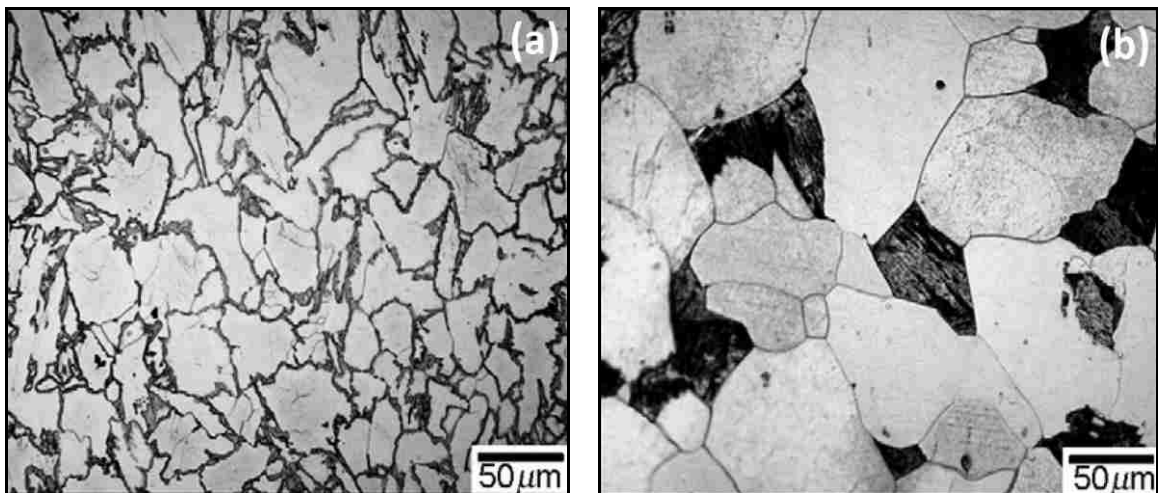


Figure 2-2 Microstructure of dual phase steel produced by (a) intercritical annealing and (b) sequential quenching methods [48].

2.1.2 Alloying Elements in Dual Phase Steels

Manganese, silicon, chromium, and molybdenum are the typical alloying elements in dual phase steels. These elements generally make solid solutions to increase the strength of the steel. Manganese is a cost-effective element for enhancing hardenability [53]. It also reduces the carbon activity in the austenite and allows martensite to be formed at slower cooling rates [54]. The diffusivity of manganese in austenite is slower than in ferrite. Due to economic constraints, the holding time during intercritical annealing cannot be extended sufficiently to reach a complete homogenization of the alloying elements in the microstructure. Therefore, as shown in Figure 2-3 there is a manganese enrichment in the vicinity of austenite grain boundaries that enhances the local hardenability. Considering this effect, if the cooling rate is not sufficiently high, the edges of the austenite grains may transform to martensite while the core of the grain transforms to ferrite/carbide [49].

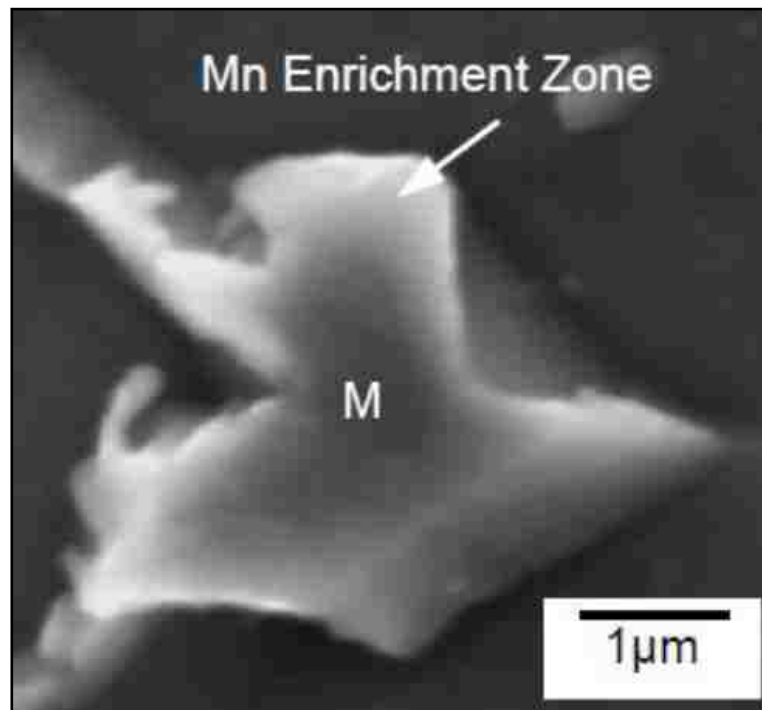


Figure 2-3 *Manganese enrichment in a martensite particle after austenite to martensite transformation [49]*

Silicon affects the chemical composition of the austenite during intercritical annealing. Silicon accelerates the migration of carbon atoms from the ferrite into the austenite [55]. It also suppresses the formation of cementite during cooling from the intercritical temperature. Hence, it prevents the formation of pearlite structure [53, 56]. Molybdenum and chromium suppress pearlite formation and reduce the critical cooling rate of austenite to martensite transformation [45, 57]; however, these elements increase the required holding time during intercritical annealing to dissolve the iron carbide [58].

Vanadium and titanium may be added to dual phase steel to form carbide and nitride precipitates [59, 60]. These precipitates increase the strength of the steel by causing precipitation hardening within ferrite grains and also enhance the hardenability of the steel. However, niobium forms precipitates and refines ferrite grains [61]. During quenching, these precipitates confine the movement of ferrite/austenite interface which enhances the martensite formation [57].

During quenching of the steel from intercritical temperature, each alloying element has an effect on the martensite start temperature according to [62]:

$$M_s(^{\circ}C) = 539 - 423(C) - 30.4(Mn) - 12.1(Cr) - 17.7(Ni) - 7.5(Mo) \quad (2-1)$$

2.1.3 Microstructure Banding in Dual Phase Steels

Alloying elements causes dendritic solidification that happens within a range of temperatures and chemical compositions. In this type of solidification, relatively pure metal solidifies in the dendrite cores and the alloying elements are rejected to the interdendritic space leading to elemental segregation. In low alloy steels, microstructure banding occurs as a reason of segregation of alloying elements during dendritic solidification [63].

During the solidification of dual phase steels, the rejection of substitutional alloying elements into the interdendritic spaces makes these regions enriched in solute. The

cores and the interdendritic spaces which include low and high alloying elements, respectively, are elongated into parallel bands under compressive stresses such as a rolling operation. Microstructure banding in a dual phase steel is shown in Figure 2-4.

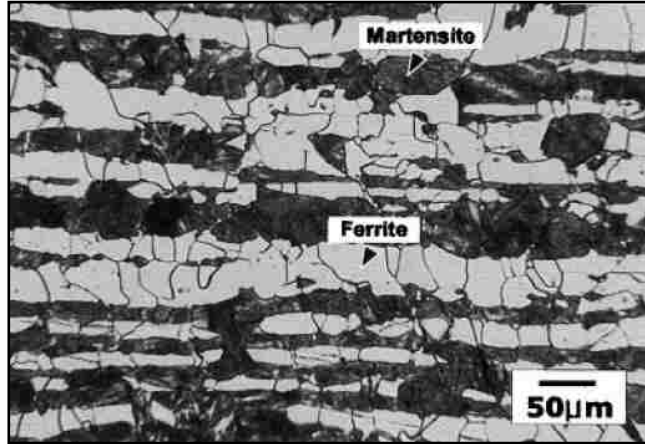


Figure 2-4 Microstructure banding in dual phase steel (015C–2.0Mn–0.2Si); austenitizing at 875 °C for 1 h, furnace cooling to 720 °C (3 K min⁻¹), water quenching [30]

Redistribution of the alloying elements can be described by the equilibrium partition ratio, k , as follows:


$$k = \frac{C_S}{C_L} \quad (2-2)$$

where C_S and C_L are the solute concentration of the solid and liquid, respectively. The values of k for the common alloying elements of dual phase steel are presented in Table 2-1. Since, the tendency of segregation is greater in alloying elements with smaller k , phosphorus has the strongest tendency for segregation; however, the type of alloying element is also an effective factor (see Table 2-1). The main alloying element in dual phase steels is manganese, which is known as the most influential element in development of banding in dual phase steels [64]. For instance, during solidification of a steel with 1.0 wt% of manganese, the chemical composition of manganese in microstructure varies from 0.7 wt% in the beginning to 1.6 wt% at the end of solidification [65]. Hence, homogenization is an essential part of the heat treatment of dual phase steels.

Table 2-1 Equilibrium partition ratios for some of the alloying elements in steel [66]

Element	k
P	0.14
Nb	0.23
Cr	0.33
Mn	0.71
Ni	0.83

Low



High

Microstructure banding does not generally occur in dual phase steels during hot rolling [67]. Elimination of banding is achievable by high temperature homogenization before intercritical annealing to redistribute alloying elements. In addition to the concentration gradients of alloying element, austenite grain size, austenitizing temperature, and cooling rate affect the microstructure banding [64].

2.1.4 Strengthening Mechanisms of Ferrite in Dual Phase Steels

Ferrite is an equilibrium phase in the Fe-Fe₃C phase diagram at room temperature. It is generally a ductile phase which increases the elongation of the steels. Ferrite has a body-centred-cubic crystal structure where carbon atoms are interstitial solid solution in the octahedral position. The flow stress of the ferrite is generally controlled by chemical composition and grain size [61, 68, 69], and is also influenced by dislocations [70, 71], as described in the following:

Chemical composition Interstitial and substitutional alloying elements in dual phase steels, e.g. carbon, manganese, silicon, chromium, and molybdenum, can increase the shear stress required for the movement of dislocations. Hence, the interaction between the alloying elements and dislocations can increase the flow stress of the material which is known as solid solution strengthening. Solid solution strengthening depends on the solute concentration [61]:

$$\sigma_{SSS} = kc^n \quad (2-3)$$

where c is the solute concentration, k is a constant, and $0.5 < n < 0.67$.

In addition to solid solution elements, the strength of ferrite can be enhanced by precipitates such as vanadium and titanium [55].

Grain Size Grain size is the other parameter that influences the plastic behaviour of the ferrite. The relationship between the yield strength and grain size was first developed by Hall [72] based on experimental work and later by Petch [73] by means of experiments and theory. The effect of grain size on the flow stress of the polycrystalline materials is described by Hall-Petch equation [70]:

$$\sigma_y = \sigma_f + k_y d^{-0.5} \quad (2-4)$$

where σ_y is the yield strength of the polycrystalline material, d is the grain size, σ_f is the friction stress opposing the movement of dislocations and, k_y is a constant. This relation has been found to be effective for grain sizes between 0.3 to 400 μm in ferritic steels [61].

Chang and Preban [74] studied the effect of ferrite grain size on the yield strength of dual phase steels. They produced different dual phase steels with carbon contents of 0.034, 0.07, 0.17 and 0.23 wt%, martensite contents of 3.3-47 vol%, and ferrite grain sizes from 6.7 to 59 μm . According to their report, the Hall-Petch equation was valid for these dual phase steels. They also indicated that k_y increased with the volume fraction of martensite in dual phase steels.

As can be seen in Figure 2-5, Jiang et al. [75] showed that at small strains, a reduction of the ferrite grain size results in an enhancement of the work hardening rate while at higher strain levels the influence almost disappears.

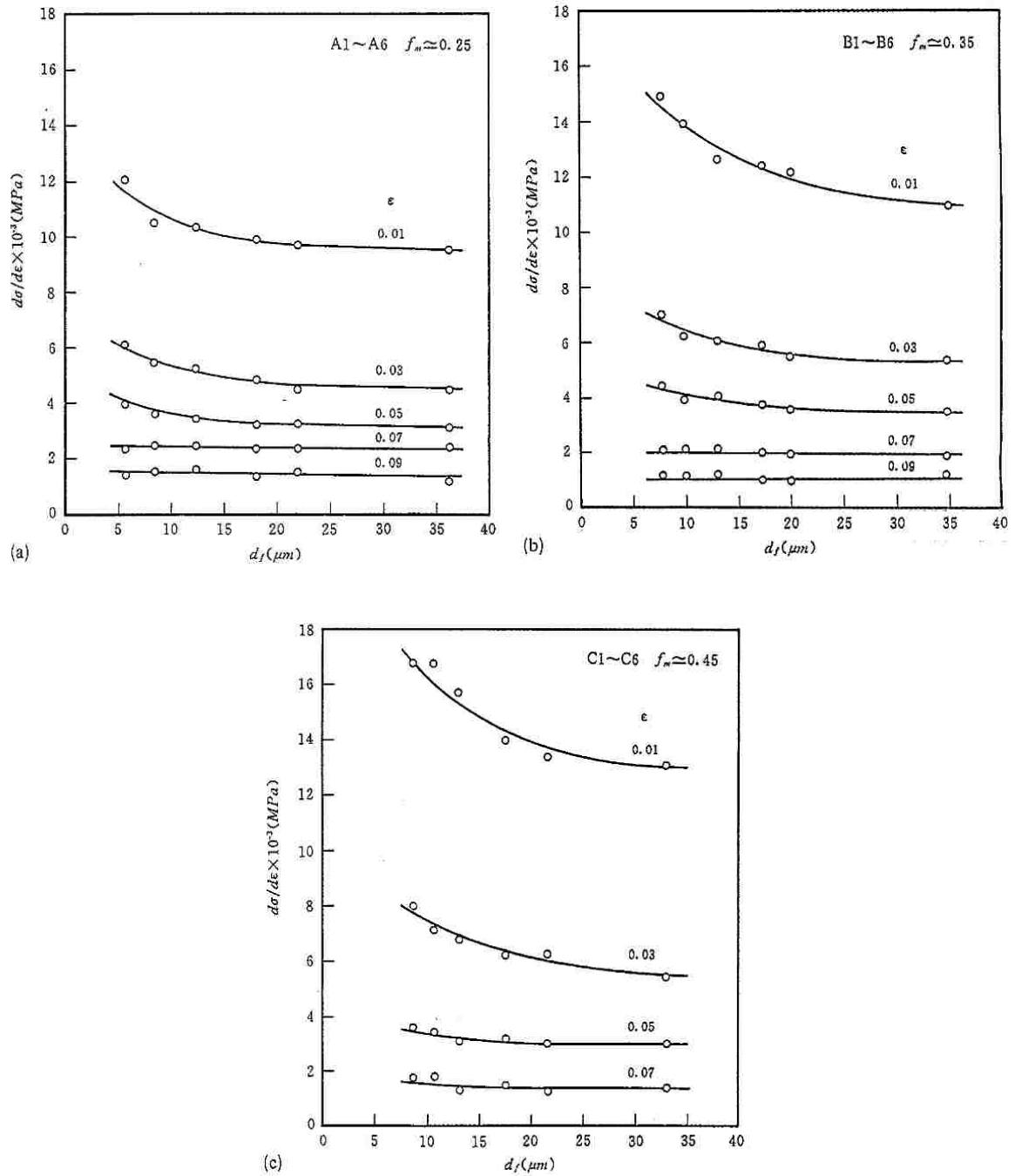


Figure 2-5 Variation of strain hardening rate as a function of ferrite grain size in dual phase steels with different martensite contents (a) A_1 - A_6 : $f_m \approx 0.25$, (b) B_1 - B_6 : $f_m \approx 0.35$, and (c) C_1 - C_6 : $f_m \approx 0.45$ [75]

Dislocations The flow stress also depends on the dislocation density [70]:

$$\sigma_{DSL} = \alpha G b M \rho^{0.5} \quad (2-5)$$

where α is a constant, G is the shear modulus, b is the Burgers vector, and M is the Taylor factor. Ferrite plasticity in dual phase steels is affected by the accumulation of dislocations behind the martensite islands during the austenite to martensite transformation. Figure 2-6 shows how the dislocation configuration evolves as a function of strain in ferrite grains in a dual phase steel. It can be seen that, in the beginning of the deformation, as the dislocation density increases it results in dislocation tangles; however, at greater strains, higher dislocation density results in a cell structure which significantly increases the ferrite flow stress.

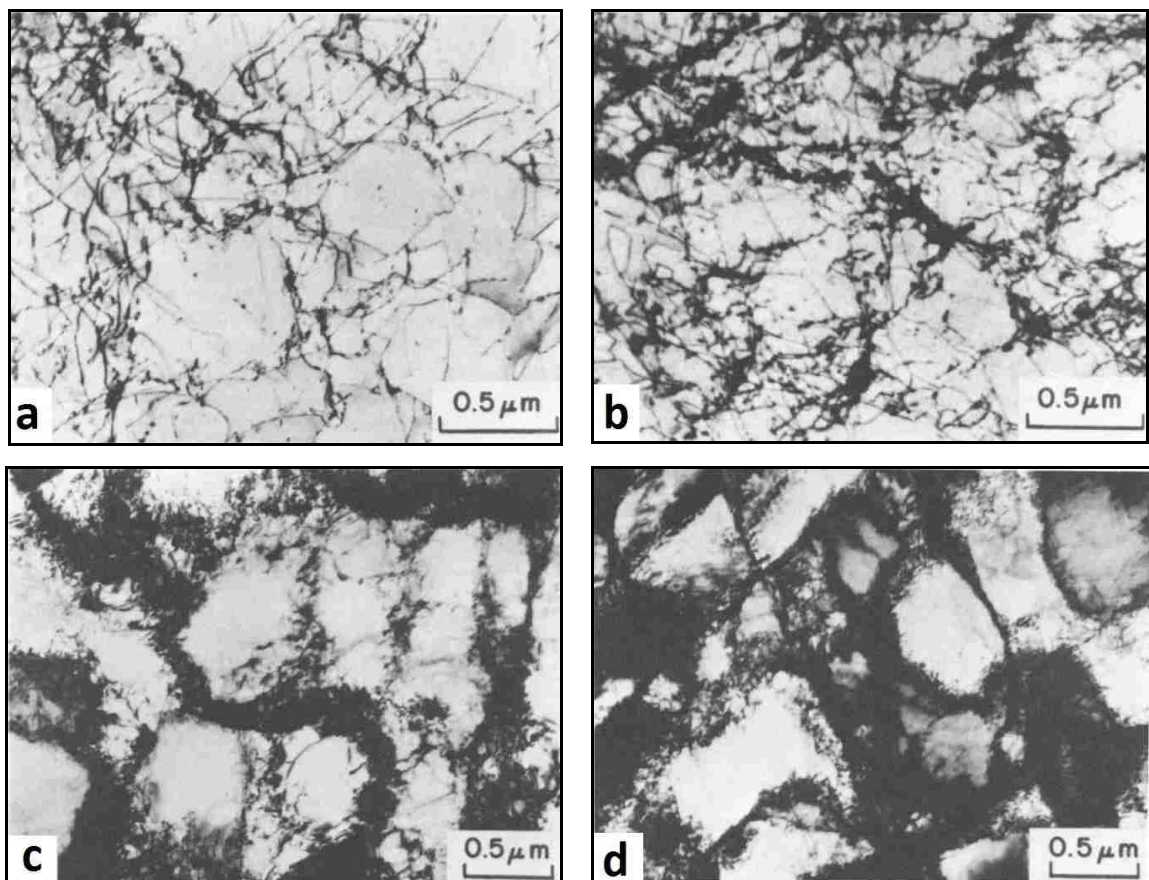


Figure 2-6 Dislocation substructure in ferrite grains of a C-Mn-Si dual phase steel formed under quasi-static uniaxial tensile test. Dislocation tangles at (a) $\epsilon=0.01$ and (b) $\epsilon=0.02$, and dislocation cells at (c) $\epsilon=0.07$ and (d) $\epsilon=0.14$. [76]

2.1.5 Martensite in Dual Phase Steels

Martensite is a metastable phase in steels which is known as a supersaturated solid solution of carbon in ferrite that is obtainable by rapid cooling of the austenite from high temperatures [57]. As can be seen in Figure 2-7-a, the lattice dimensions of martensite are a function of the martensite carbon content. The values of c and a are identical for carbon contents below 0.59 wt% and equal to the lattice parameter of pure iron. So, based on the carbon content, martensite can have a body-centred-cubic or body-centred-tetragonal crystal structure. This issue was first reported by Fink and Campbell [77] in 1926. Figure 2-7-b presents the tetragonality (c/a) of martensite which was experimentally determined by different researchers.

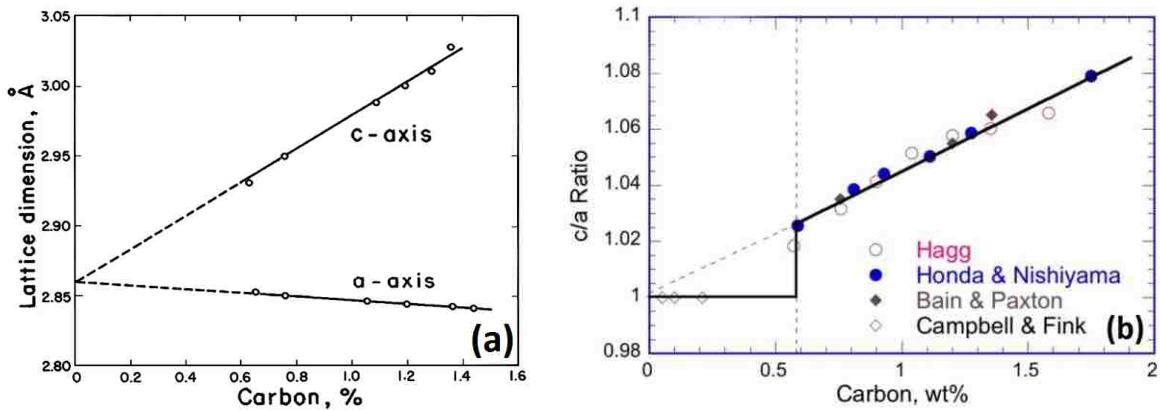


Figure 2-7 (a) Lattice parameters of martensite versus carbon content of martensite in Fe-C steels [78], and (b) tetragonality of martensite as a function of carbon content [79]

The mechanical strength of martensite primarily depends on the carbon content [59, 61, 68]. Figure 2-8 shows the significant dependence of the hardness of martensitic microstructure on the carbon content of the steel. Besides, the mechanical properties of martensite are also influenced by its structure such as lath and plate structures [59]. As it is shown in Figure 2-9, the type of the martensite structure depends on the carbon content of the steel. Figure 2-10 shows the effect of martensite carbon content on the yield strength of martensite. The two lines indicate the upper and lower values of yield

strength. Solid solution hardening can enhance the strength of martensite as a secondary strengthening mechanism after the effect of carbon content [61].

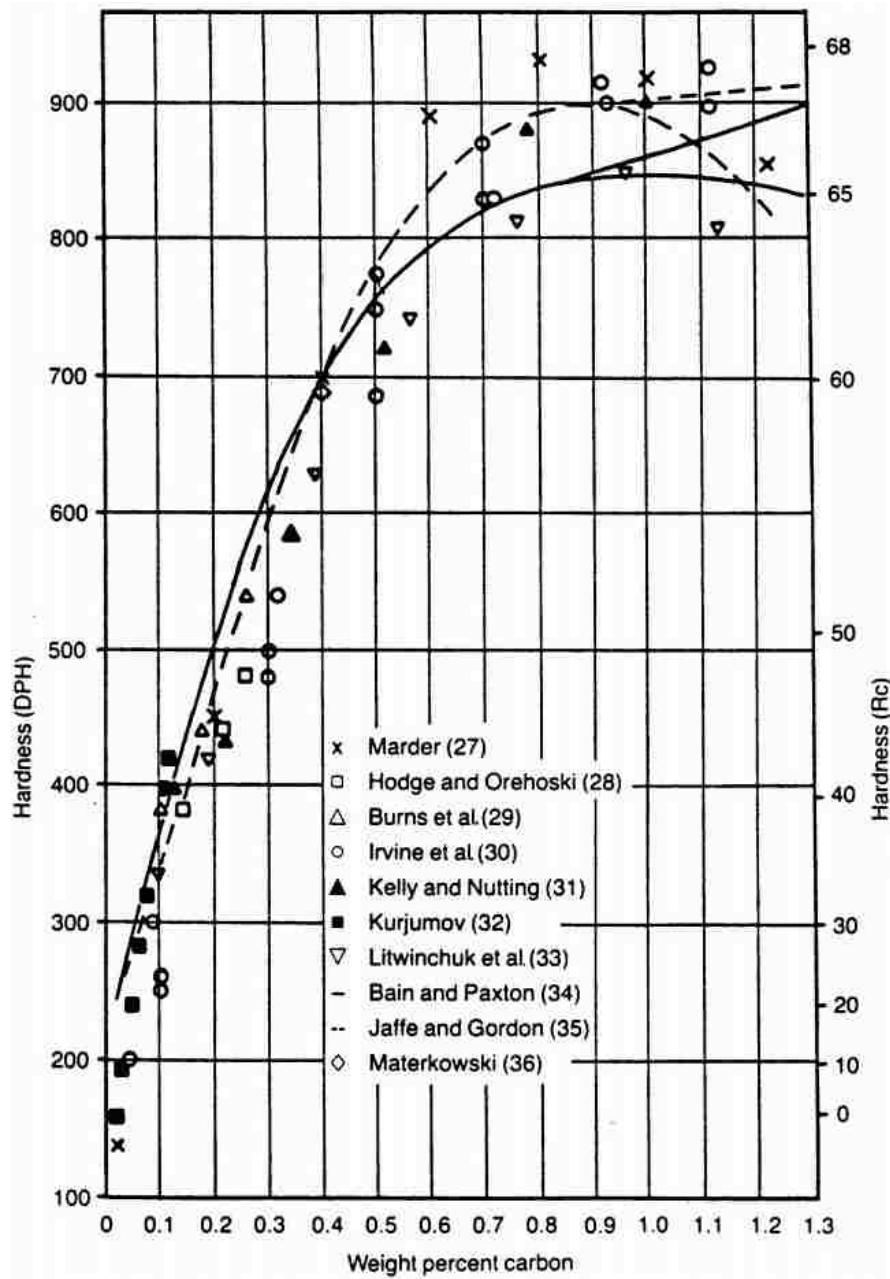


Figure 2-8 Hardness of martensitic steel as a function of carbon content [80]

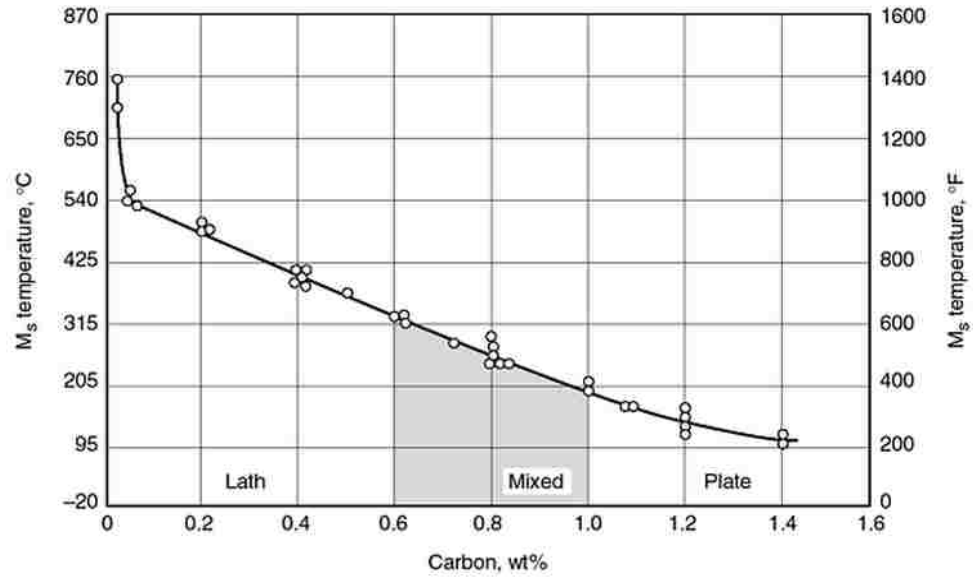


Figure 2-9 Effect of carbon content on Ms temperature in steels [81]

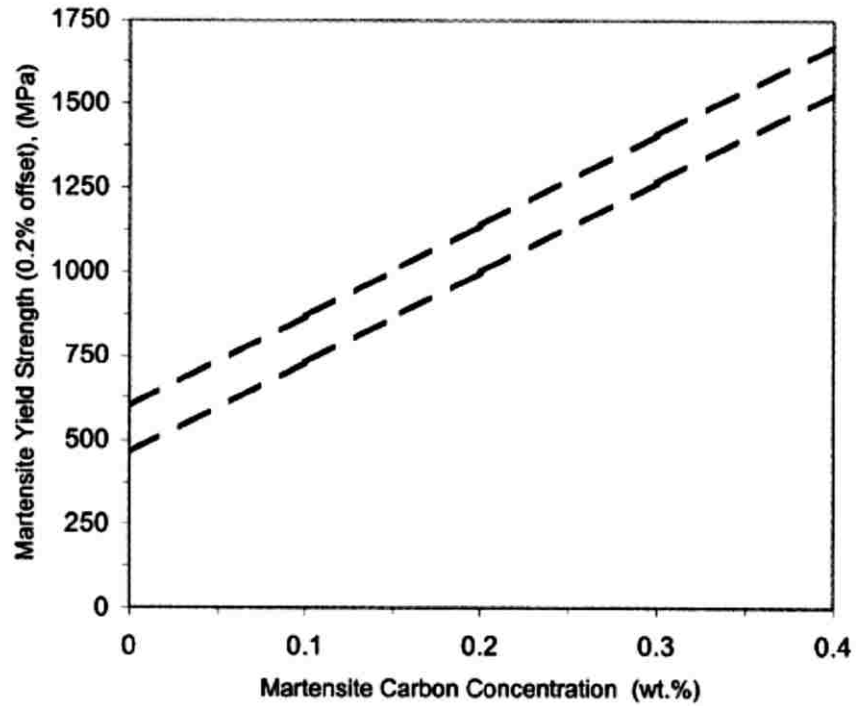


Figure 2-10 Upper and lower yield strength of martensite as a function of carbon content [59]

The mechanical properties of dual phase steels primarily depend on the martensite volume fraction [6, 28, 30, 82-87] and morphology [28, 29, 82, 83, 85-93]. There is a general agreement that finely dispersed martensite islands result in a superior combination of strength and ductility. Also, increasing the volume fraction of martensite was found to increase the yield and ultimate strengths of dual phase steel. However, when the martensite content increases, the yield strength first decreases due to a gradual removal of the yield point elongation at low martensite contents; then it starts to increase [53]. Bag et al. [82] and Byun et al. [83] indicated that the increase in strength in dual phase steels occurs up to a certain martensite content, after which a reduction in strength is observed. Bag et al. [82] reported that 55 vol% of martensite results in the highest strength.

The major strengthening mechanism in dual phase steel is associated with the martensite phase. Martensite islands can affect the strength of dual phase steels in three ways:

- Martensite is a very hard phase that can carry the external loads which are transferred from the ferritic matrix.
- Martensite can introduce “geometrically necessary dislocations” [94-96] to enhance the deformation behaviour of the two-phase material. When the deformation behaviour of the constituent phases is notably different, geometrically necessary dislocations can accommodate the strain gradient and make the deformation of the constituent phases somewhat more compatible.
- During the austenite to martensite transformation, mobile dislocations are introduced into the ferrite due to the plastic strains that are generated by volumetric expansion of the martensite [97-100]. The density of the dislocations generated in the ferrite increases with the martensite volume fraction, so the strengthening effect of martensite on ferrite is more pronounced at higher martensite contents.

During plastic deformation of dual phase steels, martensite was generally found to exhibit elastic deformation unless the strain reaches high levels [14, 101-105]. However,

martensite plasticity was reported in some cases. Jiang et al. [75] reported martensite plasticity by analyzing work hardening curves of a dual phase steel with 0.12 wt% of carbon. Also, Shen et al. [106] determined martensite plasticity in dual phase steels with 0.09, 0.23, and 0.29 wt% of carbon using in-situ scanning electron microscope images. Su et al. [107] used micro-grids to study the martensite plasticity in the steels containing 0.12 wt% of carbon. They reported plastic deformation of martensite in dual phase steels that contained 50-80 vol% of martensite. Mazinani et al. [108] indicated that the martensite plasticity occurred when its strength was reduced by lowering its carbon content or by tempering. They also reported martensite plasticity when the morphology of martensite changed from equiaxed to banded.

2.1.6 Yield Behaviour of Dual Phase Steels

Plastic deformation in dual phase steels starts in the ferrite. Hence, the yielding behaviour of dual phase steels is controlled by the ferrite properties [26, 99, 109, 110].

Generally, low carbon steels exhibit a yield point phenomenon due to the effect of interstitial carbon atoms that act against the motion of dislocations [111]. When an external stress is applied, it must exceed a critical value to unlock the dislocations. The required stress to move the dislocations in the grain is less than the necessary stress to unlock them, and this causes a sharp drop at the yield point. Hence, the upper and lower yield points are seen in the tensile stress-strain curve.

This phenomenon is not observed in dual phase steels. The stress-strain curves of dual phase steels exhibit continuous yielding behaviour. The continuous yielding of the ferrite-martensite dual phase has been related to the following:

- Before plastic deformation starts, mobile dislocations are present in the ferrite in the vicinity of martensite islands. These dislocations were generated due to the volumetric expansion of the martensite during the austenite to martensite transformation [97-100]. Figure 2-11 shows mobile dislocations at the ferrite/martensite interface region and the continuous yielding behaviour of dual phase steels with different martensite contents.

- The plastic incompatibility between the ferrite and martensite phases leads to micro-yielding of the ferrite in the vicinity of martensite under internal stresses. The micro-yielding occurs due to the movement of mobile dislocations under lower stresses compared to the yield stress of the bulk ferrite [109, 112]. This happens due to the great back stresses by martensite islands on the glide bands within the ferrite grain.

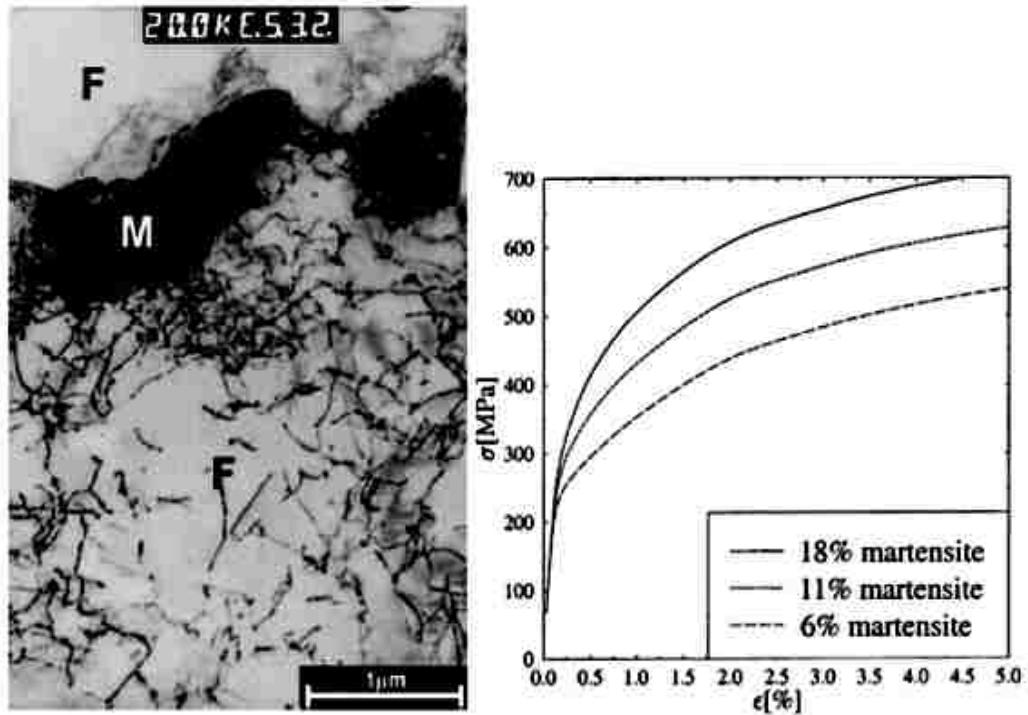


Figure 2-11 Mobile dislocations in the vicinity of ferrite/martensite interface causes continuous yielding behaviour of dual phase steels [99]

2.1.7 Work Hardening in Dual Phase Steels

As can be seen in Figure 2-12, work hardening in ferrite-martensite steels significantly depends on the volume fraction of martensite. It is reported [14, 113] that the work hardening rate is greater in dual phase steels with finer martensite islands. Also, Sarosiek [26] indicated that the work hardening in dual phase steels with continuous martensite bands is similar to the work hardening in dual phase steels with homogenized noncontinuous martensite islands.

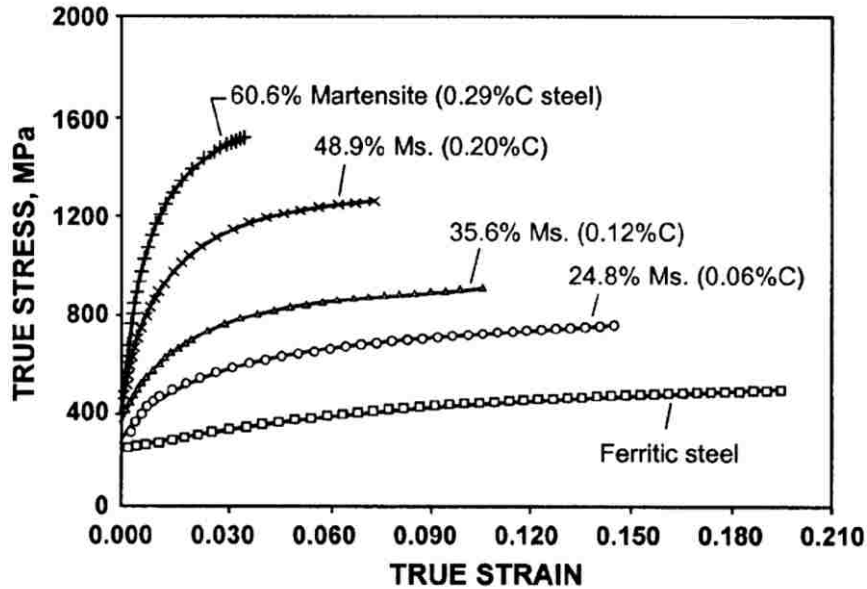


Figure 2-12 True stress-strain curve of a ferrite-martensite steel with 1.5 wt% Mn and different carbon contents annealed at 760 °C [10]

Crussard [114] and Jaoul [115] developed a method, which is known as CJ analysis, to analyze work hardening during plastic deformation. In this method, the logarithm of the strain hardening rate is plotted as a function of the logarithm of true plastic strain. The slope of the curve describes the work hardening behaviour. Based on CJ analysis, Figure 2-13 shows that dual phase steels exhibit three distinctive stages of work hardening [116-118] as follows:

Stage one: Homogeneous deformation of the ferrite occurs in the vicinity of martensite. This results in high initial work hardening rate as presented in Figure 2-13. The initial work hardening rate increases with martensite volume fraction as shown in Figure 2-12 [10, 24].

Stage two: Smaller work hardening occurs by the limited deformation of the ferrite in the presence of rigid martensite.

Stage three: At higher strains, dislocation density increases and cell structures are formed. Further ferrite deformation happens due to dynamic recovery processes like cross slip. Some martensite plasticity may happen in this stage.

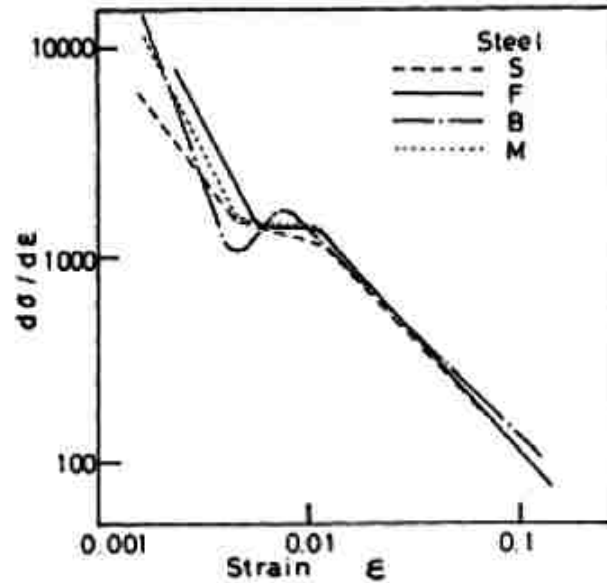


Figure 2-13 Crussard-Jaoul plot of several dual phase steels [119]

2.1.8 Failure in Dual Phase Steels

Failure mechanisms in dual phase steels depend on chemical composition, history of heat treatment, and final microstructure [88, 93, 104, 105, 120, 121]. Although martensite is known to be a hard phase with low elongation, dual phase steels show ductile fracture behaviour [18, 107, 120, 122]. Ductile fracture in dual phase steels occurs based on the nucleation and growth of voids which results in dimpled fracture surfaces. Micro-mechanisms of failure in dual phase steels are described in the following:

Void Nucleation In the beginning of deformation at low strains, nucleation of voids in dual phase steels is associated with martensite cracking and separation. At higher strains, voids also nucleate at the ferrite/martensite interface due to decohesion. Decohesion of the ferrite/martensite interface under loading occurs due to plastic

incompatibility of the two phases [108, 120, 123-125]. The size of the voids in this step depends on the size of the martensite islands [88]. Void nucleation also happens due to non-metallic inclusions [89, 105, 120, 122, 126-128] such as (Ce, Ca, Fe) sulfides [126] and MnS [129]; however, these voids in dual phase steels do not appear to have an important role in failure [123, 130]. Furthermore, nucleation of voids occurs inside martensite islands with a low carbon content. Crystallographic orientation, strain gradient, and the state of the local stress affect the nucleation of voids inside the martensite phase [14, 101, 120, 128].

Void Growth Void growth primarily occurs by elongation of the voids at the ferrite/martensite interfaces which are parallel to the applied force. Under uniaxial stress, voids generally elongate in the tensile direction resulting in failure without significant coalescence; however, under triaxial stresses, the growth of voids tends to happen in the transverse direction, causing coalescence and finally failure [123].

Fracture Although ductile fracture is the main fracture mode in dual phase steels, brittle fracture is also possible in dual phase steels with high martensite content and depends on the level of damage between the ferrite and the martensite [131]. The characteristics of the martensite have the greatest role in changing the ductile fracture of dual phase steels to brittle. Kim, et al. [22] reported cleavage fracture in ferrite in coarse martensite structure whereas void nucleation at the ferrite/martensite interface in a fine martensite structure. As shown in Figure 2-14, the ductility of fracture of dual phase steels is reduced by increasing the martensite size and volume fraction [15, 18, 22, 132]. The martensite volume fraction at which brittle fracture occurs is not fixed. Generally, a combination of ductile and brittle fracture is seen in dual phase steels with intermediate martensite volume fractions [122]. Furthermore, martensite with higher carbon content crack easily [10], and large banded martensite with interconnected network decrease the ductility of the steel [18, 22, 132]. In addition to the ductile and brittle fracture, quasi-cleavage fracture is also found to happen as a transition fracture

mechanism between ductile and brittle fracture. Hence, there is not always a clear boundary between ductile and brittle fracture [133].

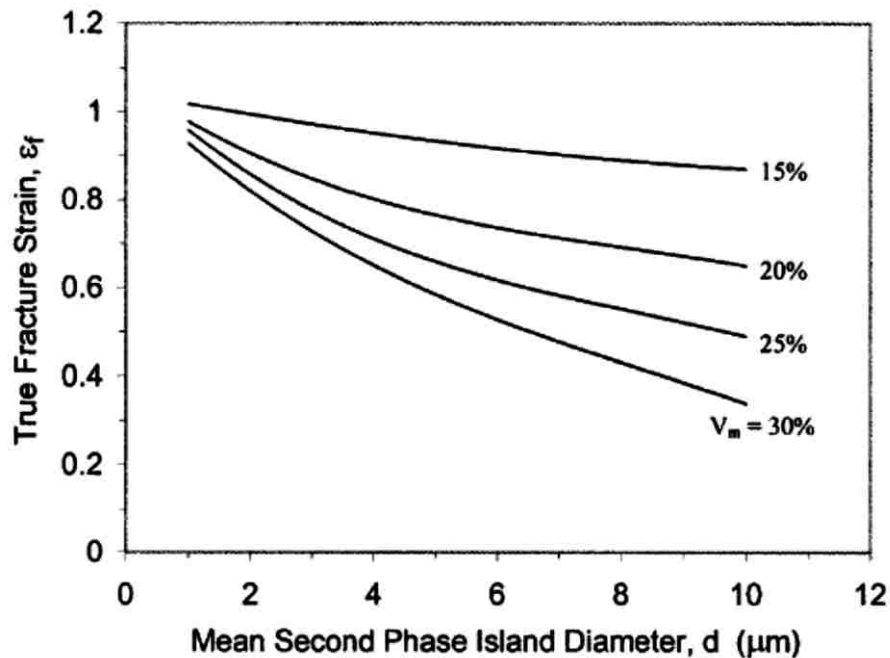


Figure 2-14 True fracture strains of dual phase steels with 0.066-0.13% carbon with different martensite volume fraction and size [15]

2.2 High Energy Rate Forming Technologies

There are three well-known high energy rate forming (HERF) technologies which can provide high strain rate forming conditions: explosive forming, electromagnetic forming, and electrohydraulic forming. These technologies are mainly used to form sheet metals at high strain rates.

As an advantage of these technologies, one sided dies can be used to form the sheets into a die cavity. This advantage becomes remarkable when very large dies must be fabricated using the expensive and time-consuming processes. Also, due to the smaller area of contact between the sheet and the forming tools, there is a notable saving on lubrication of the parts [134]. A brief description of the explosive, electromagnetic, and electrohydraulic forming technologies is presented hereafter.

2.2.1 Explosive forming

The interest in explosive forming applications appears to have started in the aerospace industry [134]. Explosive forming technology was developed to form a variety of metals and alloys. The result showed high reproducibility for geometrically complicated and large parts with great accuracy. Explosive forming has been commonly used to form sheet metals. Figure 2-15 shows that the explosive material can be assembled in different shapes. This capability allows for control of the explosive wave to create the desired force on different sheet surfaces to completely fill the die. After detonation, the waves propagate through a liquid medium, such as water, to reach the sheet surface.

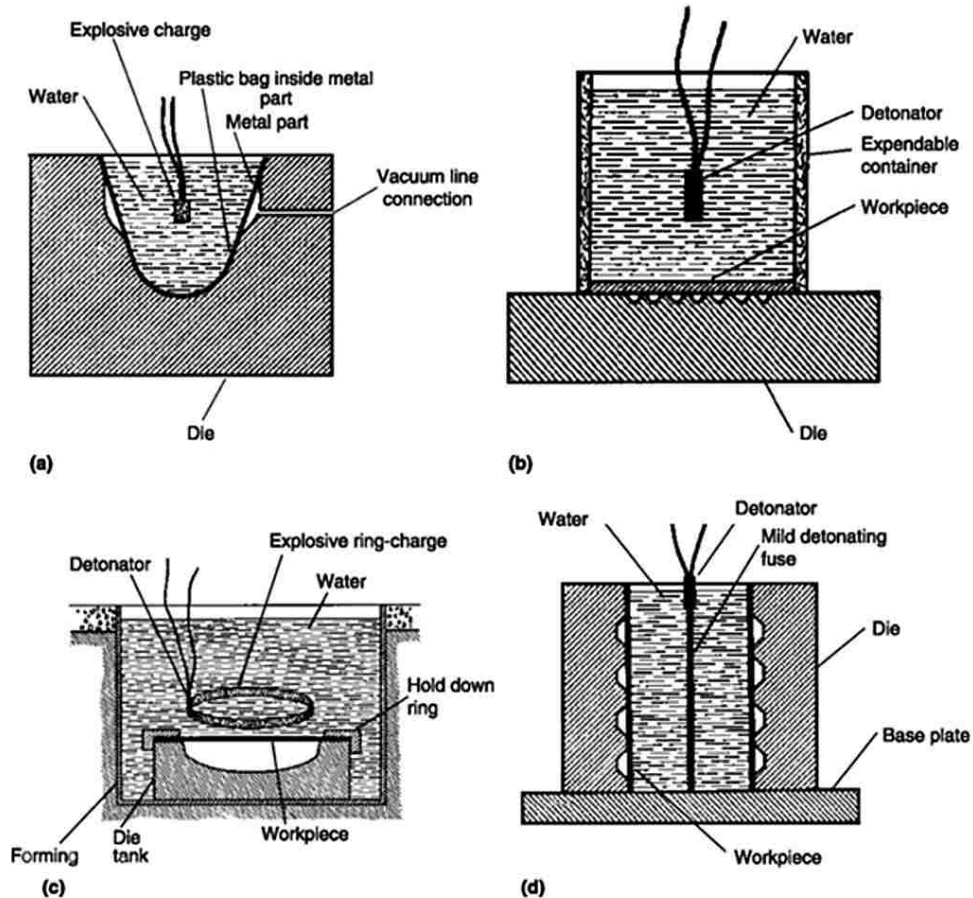


Figure 2-15 Typical explosive forming operations. (a) Sizing with a water-filled die cavity, (b) for forming a flat panel, (c) use of detonation cord to prescribe the pressure distribution in an open forming system, and (d) use of detonation cord to form a cylinder [135]

2.2.2 Electromagnetic forming

Electromagnetic forming is widely used both in metal joining and metal forming. Application of electromagnetic forming depends on the electrical properties of the material. The material must typically have an electrical resistivity of less than 15 mΩ.cm such as copper, aluminum, steel and brass [134]. In this technique, a capacitor is discharged into a coil which is near the workpiece to generate a magnetic field. The magnetic field around the coil generates an electric current and consequently a magnetic field in the workpiece. The two magnetic fields repel each other causing the workpiece to deform. Figure 2-16 shows some simplified electromagnetic forming circuits and processes for a tubular workpiece. The undesired heat effects and tool marks associated with other techniques do not appear in this technology [135].

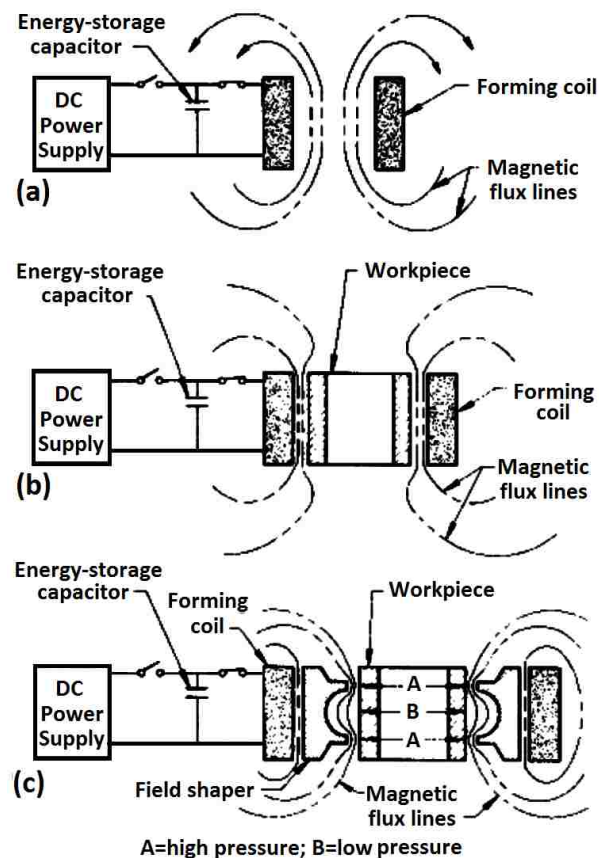


Figure 2-16 Basic circuit and magnetic field patterns for electromagnetic compression forming of a tubular workpiece, (a) field pattern in absence of workpiece, (b) field pattern with workpiece in forming coil, and (c) field pattern when field shaper is used. A, high pressure; B, low pressure.[135]

2.2.3 Electrohydraulic forming

Electrohydraulic forming (EHF), also known as electroshape [136], electrosark [136, 137], electric discharge[138], and underwater spark [139] forming, is a high energy rate forming process that directly converts electrical energy into work [136-138]. It is principally the same as explosive forming. The major difference is the method of generation of the forming wave. Instead of chemical explosion in explosive forming, in electrohydraulic forming the pressure is generated by an electrical discharge across a small gap between two electrodes.

The earliest applications of electrical discharge power were reported by Early and Dow [140] in 1953 for sheet metals and Yutkin [141] in 1955 for tube bulging. In the 1960s electro-discharge forming technology developed rapidly [142-144]. The formation of spark channels and the physics of underwater discharge were investigated by several researchers [145, 146]. The whole process takes up to a few hundreds microseconds depending on the positioning of the electrodes and the applied voltage.

Figure 2-17 schematically shows the equipment used for the electrohydraulic forming process. A capacitor bank stores electricity in a circuit that includes two electrodes. An aluminum or magnesium bridge wire may be placed between the electrodes as guiding the path. By closing the circuit, the wire instantly vaporizes and provides a plasma channel in the water which results in a spark. The spark generates a shock wave that propagates radially through the water which forces the sheet metal into the die. This process is completed in a few microseconds. An alternative to using the bridge wire is to increase the capacitor voltage. A higher voltage is able to generate a spark without the wire [136, 137]. The advantage of using a wire is that since it acts as a guiding path for the spark, the use of nonconductive liquids becomes possible; also the wire can be shaped according to the geometry of the product. The use of a bridge wire is not suitable for continuous production because the wire has to be replaced after each operation [147].

Compared to explosive forming, electrohydraulic forming is often preferred because of its shorter cycle times and generally safer operation. However, the amount of energy

in chemical explosion is higher that can shape larger parts [139, 147]. Also, compared to electromagnetic forming, electrohydraulic forming can be performed on poor conductors and is typically cheaper because the expensive design and production of consumable coils are omitted. The limit of the electrohydraulic forming process relates to the available capacitor bank energy. In fact, the physical size of the capacitor banks is a constraint. Consequently, the process is typically applicable for small and medium sized tube and sheet components with relatively small thicknesses [134]. Table 2-2 indicates a comparison between explosive forming, electromagnetic forming and electrohydraulic forming technologies.

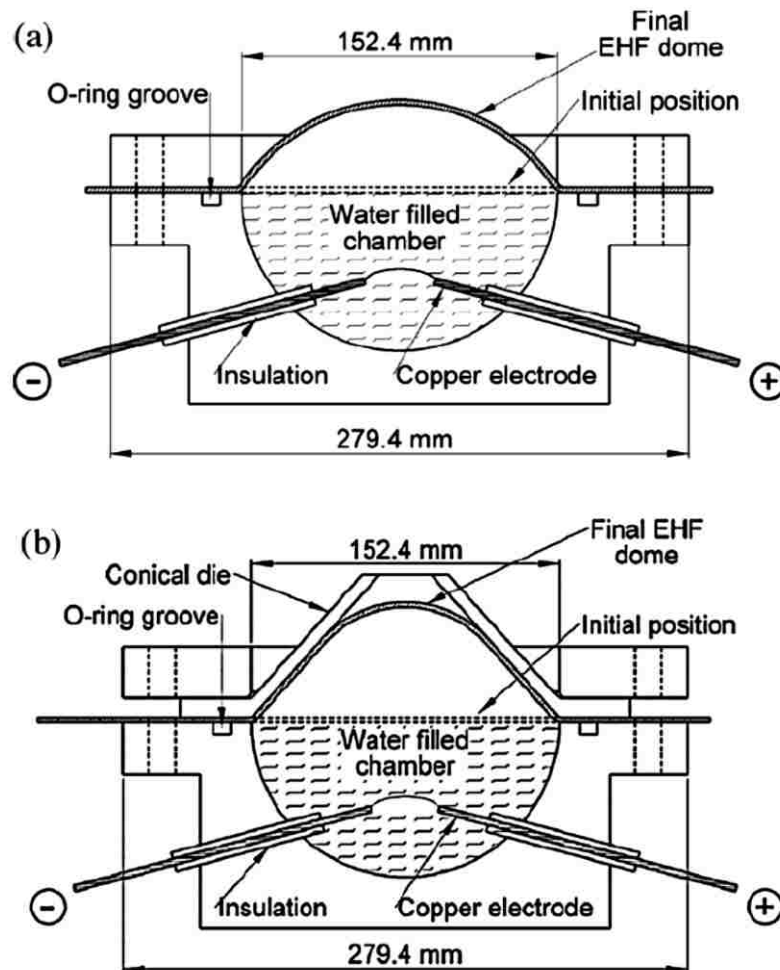


Figure 2-17 Schematic electrohydraulic forming setup (a) under free-forming, and (b) inside a conical die [148]

Table 2-2 Characteristics of HERF technologies [136]

	Standoff	Explosive forming		Electromagnetic forming	Electrohydraulic forming	
		Contact	Confined		Bridgewire	Spark Discharge
Size limits	6 m dia	6 m dia	1.5 m dia	0.3 m dia	1.2 m dia	1.2 m dia
Shape complexity	Moderately	Simple	Complex	Complex	Complex	Complex
Advantages	Large parts	High pressures	Reduced operations for complex shapes	Controllability & repeatability	Controllability & repeatability	Controllability & repeatability
Capital cost	Low	Low	Low	Moderate to high	Moderate	Moderate
Tooling cost	Low	Low	Moderate	Moderate to high	Low	Low
Production rate	0.5-4 pts/hr	0.5-4 pts/hr	2-12 pts/hr	To 1000 pts/min	4-12 pts/hr	To 50 pts/hr
Leadtime	Short	Short	Short	Moderate to long	Moderate to long	Moderate
Facility	Remote	In-plant or remote	In-plant or remote	In-plant	In-plant	In-plant

Source: Adapted from Noland et al., 1967.

2.3 Hyperplasticity

Hyperplasticity is a remarkable improvement in formability of materials when formed under certain forming conditions. Hyperplasticity may occur for strain-rate sensitive sheet materials when formed in high strain rate conditions; however, it can also occur in quasi-static forming conditions. As described in the following, incremental sheet forming and HERF technologies exhibits great potential to improve the formability of sheet metals in quasi-static and high strain rate forming conditions, respectively.

2.3.1 Incremental Sheet Forming

Formability improvement in sheet metals is achievable in quasi-static forming condition by incremental sheet forming (ISF) technologies. For the first time, before it was technically feasible, Leszak [149] proposed the idea of incremental forming of sheet metals. Nowadays, ISF allows manufacturing of prototypes directly from a 3D CAD model and a forming tool which is controlled by a CNC machine. As shown in Figure 2-18, there are different types of ISF processing. Depending on the number of contact points, incremental forming can be divided into single point incremental forming (SPIF) and two points incremental forming (TPIF). SPIF and TPIF are also known as negative and positive incremental forming. In SPIF, the opposite side of the sheet is supported by a faceplate while in TPIF the sheet is supported by a partial or a full die.

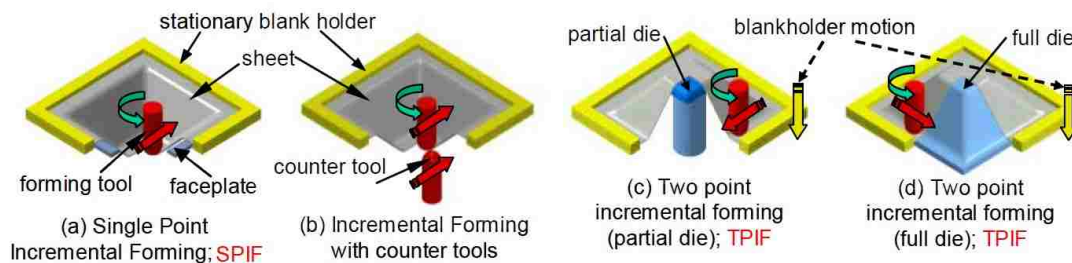


Figure 2-18 Incremental sheet forming process, (a) SPIF, (b) SPIF with counter tool, (c) TPIF with a partial die, and (d) TPIF with a full die. [150]

So far, different mechanisms have been suggested for the formability improvement of sheet metals in ISF:

Kim and Yang [151] formed small local regions of sheet metals by incremental moving of a hemispherical forming tool over the surface of the blanks. They reported that formability improvement occurred mostly by shear deformation which resulted in a more uniform distribution of strain in the sheets.

Based on theories of plastic instability, Iseki and Kumon [152] indicated that the forming limit curve of the sheets is located much higher when formed by ISF.

In the most recent work, Buffa et al. [153] reported formability improvement of aluminum alloys when formed by SPIF. They increased the rotational speed of the tool and the formability of AA1050-O, AA1050-H24, and AA6082-T6 sheets was enhanced through localized heating of the sheet.

2.3.2 High Strain Rate Forming

Under certain high strain rate forming conditions, strain-rate sensitive materials exhibit a significant improvement in formability, which is known as hyperplasticity. The improvement in formability of materials in high strain rate forming is beneficial for manufacturing parts with geometries that are difficult to form under quasi-static conditions [154]. HERF technologies have a great potential to satisfy hyperplasticity conditions. They offer the capability of controlling the forming process under high strain rate forming condition. For instance in EHF, the morphology of an impulsive pressure wave, i.e. amplitude and distribution, is an influential parameter that can be modified for different forming purposes [155].

The study of formability behaviour of materials under high velocity deformation started in the 1940s [156], and continued in the 1950s [157] and 1960s [158-160]. The investigation into the economics of high strain rate forming became important during the 1960s [161]. So far, the enhancement of formability in high strain rate forming has been observed in different steels [162-165], aluminum alloys [166-168], copper [167,

169-171], tantalum [170, 172], and titanium alloys [173]. Similar to other grades of steel, dual phase steels show hyperplasticity under high strain rate forming [35-37, 39, 40]. Figure 2-20, Figure 2-21, and Figure 2-19 show the formability improvement of aluminium, copper, iron, and steel under quasi-static and high strain rate forming conditions. As can be seen, a remarkable formability improvement was achieved in the specimens formed at high strain rate. Development of electromagnetic forming [165, 167, 174-176] and electrohydraulic forming [154, 177-180] provided the ability to study the formability of materials in larger scales and under complex states of stress which were more similar to industrial manufacturing conditions.

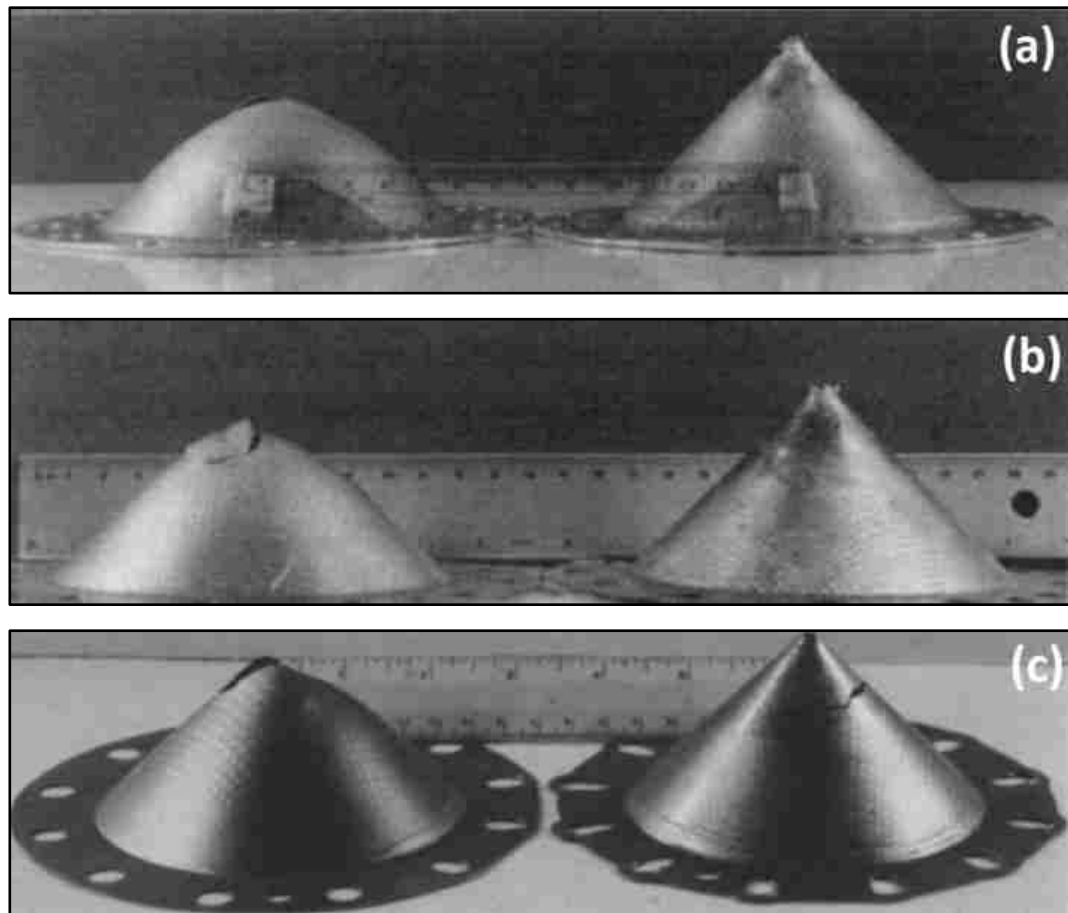


Figure 2-19 Formed specimens of (a) Al 6061 T4 [178], (b) OFHC copper[178], and (c) iron [177], under quasi-static (left) and high strain rate conditions using electrohydraulic forming (right)

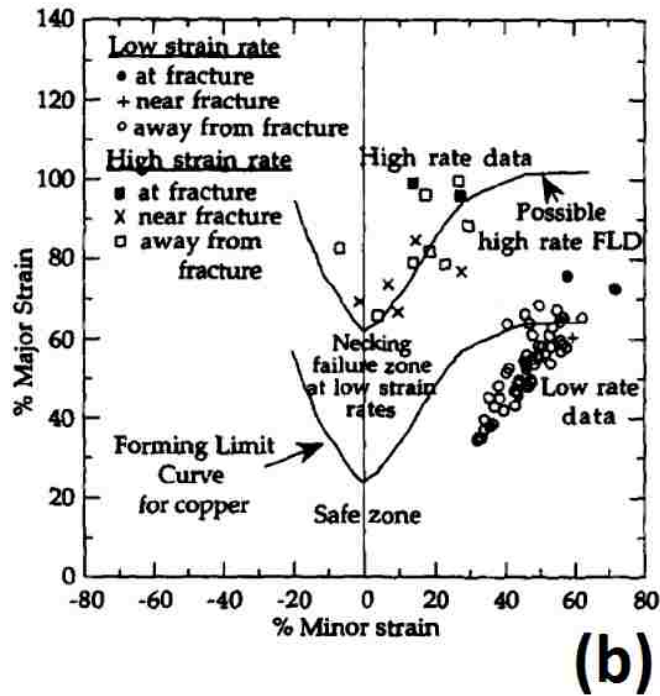
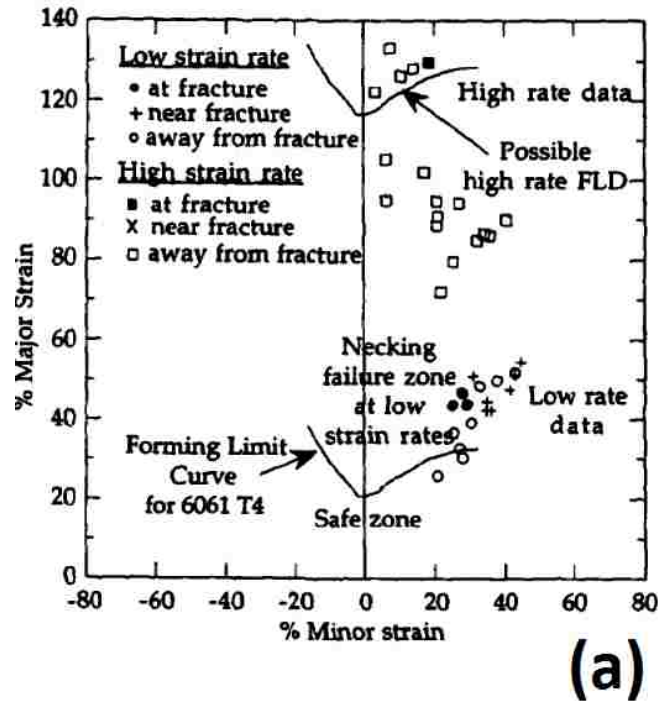


Figure 2-20 Forming limit diagrams of (a) Al 6061 T4 [181], (b) OFHC copper [182] at low and high strain rates. Formability improvement was observed in high strain rate forming.

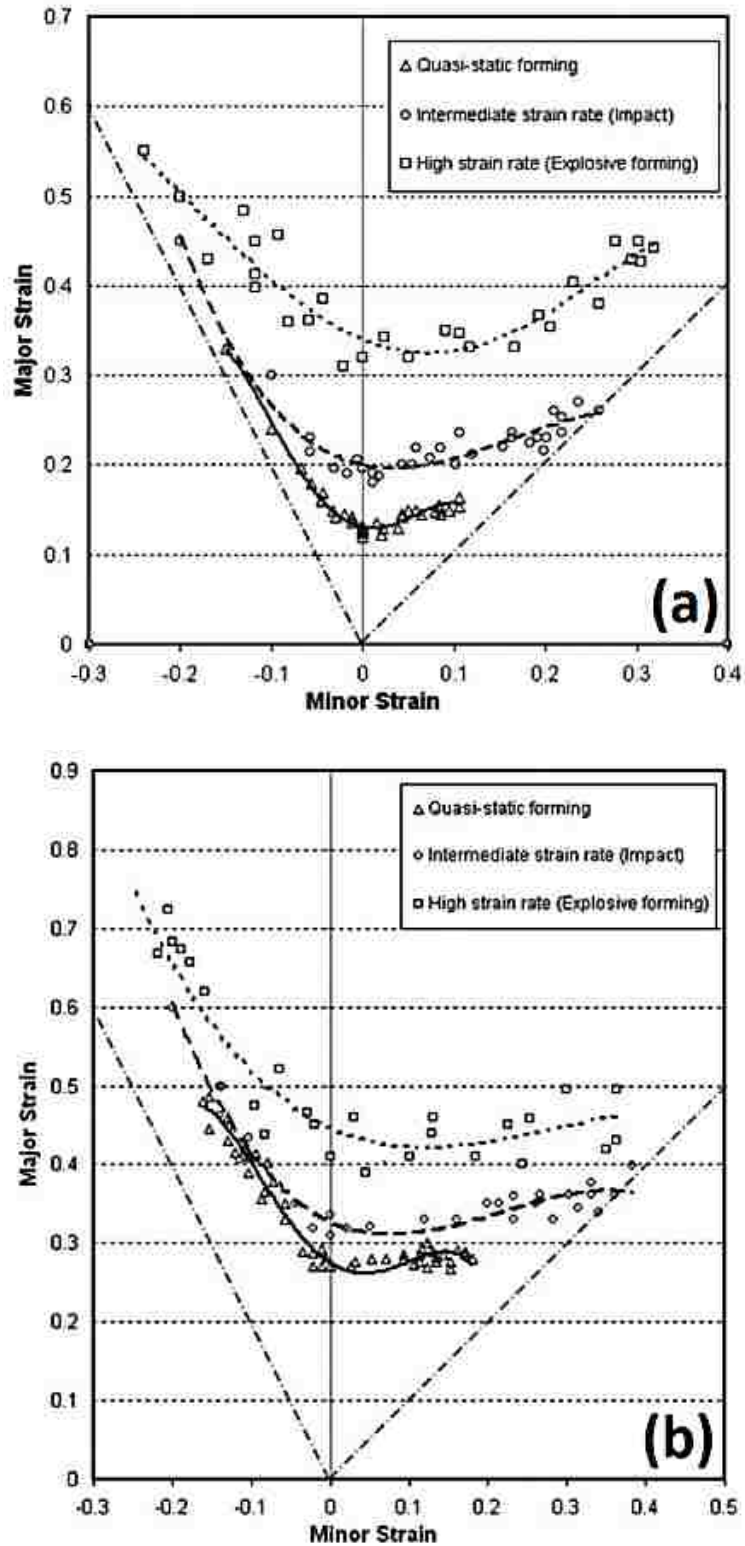


Figure 2-21 Forming limit diagrams of (a) Al 6061 T6, and (b) AISI 1045 steel at low and high strain rates [183]. Formability improvement was observed in high strain rate forming.

2.3.3 Mechanisms of Hyperplasticity in High Strain Rate Forming

Changes in constitutive behaviour [39, 184], inertial effects [185-187], die effects [176], and adiabatic shear bands have been identified as the main causes of hyperplasticity in high strain rate forming that are discussed in the following.

2.3.3.1 Changes in constitutive behaviour

Equation (2-6) is a simple, well-known, constitutive law for strain rate sensitive materials that are formed at high strain rate at room temperature [188].

$$\sigma = K\varepsilon^n \dot{\varepsilon}^m \quad (2-6)$$

where σ , ε , and $\dot{\varepsilon}$ are the stress, strain, and strain rate, respectively. Also, n is the strain hardening exponent and m is the strain rate sensitivity parameter.

As an empirical constitutive law for strain rate sensitive materials, the Johnson-Cook constitutive model [189] considers the effects of strain, strain rate and temperature on the von Mises flow stress:

$$\sigma = [A + B\varepsilon_p^n][1 + C \ln \dot{\varepsilon}^*][1 - T^{*m}] \quad (2-7)$$

where ε_p is the effective plastic strain, $\dot{\varepsilon}^* = \dot{\varepsilon} / \dot{\varepsilon}_0$ is a dimensionless plastic strain rate relative to a reference strain rate of $\dot{\varepsilon}_0$, and $T^* = (T - T_{room}) / (T_{melt} - T_{room})$. A , B , C , n and m are material constants that are obtained by empirical investigation.

Also, Zerilli and Armstrong [190] developed a physically-based constitutive model based on the motion of thermally activated dislocations to determine the von Mises equivalent stress:

$$\sigma = \Delta\sigma'_G + \sigma_{th} + kl^{-1/2} \quad (2-8)$$

where $\Delta\sigma'_G$ presents the contribution of the solute and the initial dislocation density and σ_{th} considers the contribution of strain rate and temperature on the yield stress. Also, k is the microstructural stress intensity and l is the average grain size.

Strain rate sensitivity is a key parameter in the hyperplastic behaviour of materials at high strain rate. Investigations carried out in the 1970s and 1980s [191-195] indicated

that under high strain rate conditions, the strain rate sensitivity was significantly increased and led to an enhancement of strain hardening [196-206]. High strain rate elastic behaviour of BCC Armco-iron and low-alloyed steel was studied by Dusek [162]. Dusek examined the yield point dependence of two ferritic steels on the strain rate. He reported that within the range 10^{-3} - 10^2 s^{-1} , there is a slow increase in yield stress. However, from 10^2 to 10^4 s^{-1} the increase is more significant. He also indicated that Young's modulus is independent of the strain rate. Other researchers [198, 199] also indicated that at low temperatures and at strain rates of less than 10^2 s^{-1} , plastic deformation is primarily controlled by the strain hardening exponent and to a lesser extent by the strain rate sensitivity exponent. However, post-uniform elongation is governed by the strain rate sensitivity exponent and ductile fracture processes.

In 1990s, El-Magd [207] reported that for strain rate sensitive materials, under dynamic loadings with strain rates of more than 2000 s^{-1} , the following constitutive law can be applied:

$$\sigma = \sigma_0 + \eta \dot{\epsilon} \quad (2-9)$$

El-Magd also indicated that during dynamic loading, the increase of strain rate sensitivity in the necking region significantly enhanced the flow stress in this area and reduced the instability.

In 2007 [208], Lee et al. studied the impact behaviour of 316L stainless steel using a Split-Hopkinson bar. A significant increase in work hardening and strain rate sensitivity was observed at a strain rate of 7.5×10^3 s^{-1} which affected the stress-strain behaviour of the material.

Hu and Daehn [187] indicated that the combination of stress state and constitutive behaviour in high velocity forming resulted in different ductility improvements. They reported that in a uniaxial tensile test, the material with lower m and higher n showed more ductility improvement whereas in the ring expansion test, the material with lower n and higher m showed a greater improvement.

The effect of strain rate on forming limit diagrams (FLDs) was reported by Jie, et al. [184] and Dariani, et al. [183] in 2009.

2.3.3.2 Inertial Effect

Under high strain rate forming, the workpiece has the tendency to maintain its current velocity. This effect, which is known as the inertial effect, is negligible in quasi-static forming but is enhanced during HERF [135]. As a major reason of hyperplasticity, the inertial effect has been investigated for a long time: during the 1960s [209], 1970s [210], 1980s [186, 211, 212], and 1990s [177-179, 213-215]. Research showed that the inertial effect enhanced ductility by delaying the onset of necking in uniaxial tension [186, 187] as well as in the ring expansion test [185, 216, 217].

Priem et al. [218] studied the manufacture of metallic parts by electromagnetic and electrohydraulic forming. They proposed that the inertial effect reduced the velocity gradient across the neck by generating additional tensile stresses outside the necking region. Consequently, additional extension occurred in the region of uniform deformation of the tensile specimen which resulted in a formability improvement.

Rajendran and Fyfe [185] studied an electromagnetically expanded ring and suggested that compressive forces were created due to the inertia effect, which could reduce void growth and delay necking.

Hu, et al. [213] indicated that material inertia is effective when extension velocity is greater than a critical value. This value is a function of the strain rate sensitivity and the strain hardening exponent.

Needleman [214] reported that as a result of inertial effects, the material could slow down necking by reducing the stress triaxiality in the centre of the neck.

2.3.3.3 Die Effect

In 2002, Oliveira [219] reported no formability improvement in free forming of Al alloys under electromagnetic forming. In 2005, J.M. Imbert, et al. [176] reported the formability enhancement of AA5754 Al sheet alloy by electromagnetic die forming. The report indicated that electromagnetic forming did not increase the formability in free

forming (without a die). They concluded that the die effect plays a significant role in enhancement of formability of parts in high strain rate forming.

During the 90s V.S. Balanethiram, et al. [177-179] studied the deformation of 6061 Al alloy and HCOF Copper using EHF. Studies were carried out using a conical die. Results showed that in addition to “inertial stabilization” against neck growth, formability improved by “inertial ironing” because of the strong impact of the sheet against the die. Consequently, a large compressive hydrostatic stress is formed which can reduce damage by closing the voids and postpone necking.

2.3.3.4 Adiabatic Shear Bands

Adiabatic shear bands (ASBs) are narrow microscopic regions that are created due to significant localized plastic deformation during dynamic deformation of material [220, 221]. Generally, there is a remarkable local rise of temperature in the ASB region which leads to local work softening. The work softening allows further plastic deformation in the metal rather than failure and fracture. Hence, it results in formability improvement.

ASBs are typically formed when materials are deformed by strong impact or torsion. Impact speed, geometry constraints, and microstructure characteristics have a significant influence on the localization of shear strain [222-225]. Figure 2-22 shows the ASBs in a low carbon steel deformed by compressive-type split-Hopkinson pressure bar at very high strain rates.

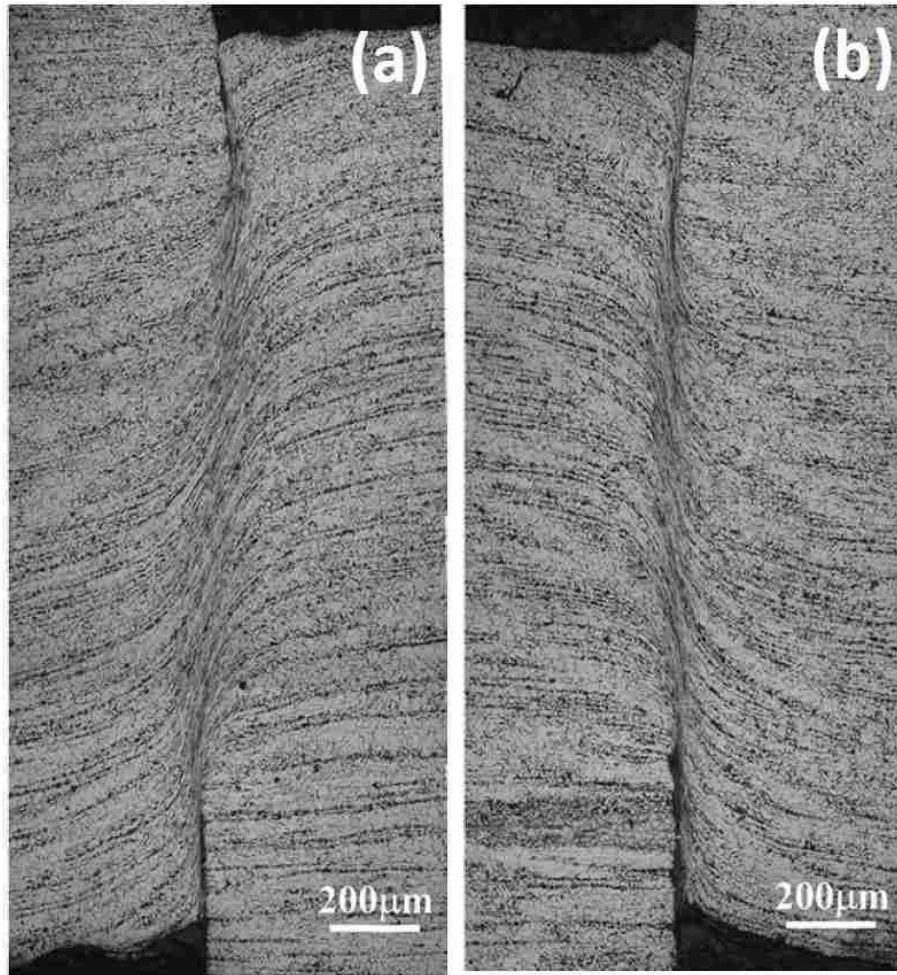


Figure 2-22 Optical micrographs of shear zones in S15C steel specimens formed at (c) $5.0 \times 10^4 \text{ s}^{-1}$ and (d) $2.0 \times 10^5 \text{ s}^{-1}$.

2.4 Dislocation Motion in BCC Materials at High Strain Rate

Dislocation velocity, v , is related to the shear strain rate, $\dot{\gamma}$, by [226]:

$$\dot{\gamma} = m^* b \rho v \quad (2-10)$$

where m^* is the orientation factor, b is the Burgers vector, and ρ is the dislocation density. The maximum velocity of a dislocation is close to speed of the elastic shear wave in the material [190]. When the strain rate is sufficiently high that the maximum dislocation velocity would be surpassed, the relationship changes to:

$$\dot{\gamma} = m^* b \rho \Delta x \quad (2-11)$$

where $\dot{\rho}$ is the rate of increase of the dislocation density and $\Delta \mathbf{x}$ is the average dislocation displacement. In this case, dislocation density increases in density through nucleation rather than merely by multiplication [227].

Plastic deformation in steels is controlled by the movement of dislocations; however, there are several obstacles against the motion of dislocations. It is possible for dislocations to overcome the obstacles if sufficient shear stress is applied. The Peierls-Nabarro shear stress (τ_{PN}) is the required shear stress for a dislocation to move by one atomic space:

$$\tau_{PN} = \frac{Gb}{2c} \exp(-\pi a/c) \sin(2\pi x/c) \quad (2-12)$$

where G is the shear modulus, b is the Burgers vector, c is the lattice spacing, and a is the lattice parameter.

A dislocation can also pass the obstacles by the aid of thermal fluctuations [228]. In BCC materials, the interaction between dislocations and lattice controls the thermal activation of mobile dislocations [190]. The movement of thermally activated dislocations can rule plastic deformation until a critical strain rate at which the movement and multiplication of existing dislocations cannot accommodate the plastic deformation anymore [227]. In most BCC metals, this occurs at approximately 10^4 s^{-1} , with a dislocation density of 10^6 - 10^8 cm^{-2} [229]. A remarkable increase in strength occurs in metals at this point since dislocations reach their maximum velocity and then nucleation of new dislocations is required.

Figure 2-23 displays the dependence of the lower yield stress of mild steel on the strain rate at different temperatures. The diagram is divided into three regions: I, II, and IV. Region I represent quasi-static conditions, where deformation is controlled by long range (athermal) obstacles. In region II, the flow stress is logarithmically dependent on the strain rate. In this condition, short range obstacles become influential which can be overcome by thermal activation. Here, thermally activated dislocation controls the strain rate sensitivity. In region IV, at very high strain rates, over 5000 s^{-1} , the dependence of

the flow stress on the strain rate increases significantly. The nucleation of dislocations occurs to allow the deformation to proceed. At this point, dislocation drag, due to the interaction between the gliding dislocations with thermal phonons and conduction electrons, opposes the motion of dislocations which can increase the flow stress.

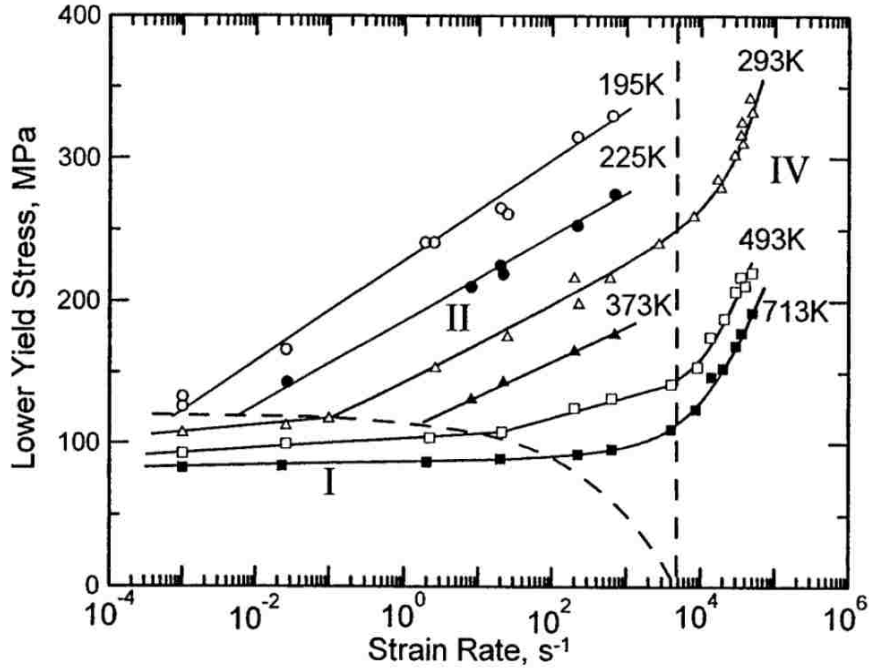


Figure 2-23 Dependence of the lower yield stress on the strain rate in a 0.12 wt% C steel [230]

CHAPTER 3

3 Experimental Procedure

Three commercial Fe-C-Mn dual phase steel sheets, i.e. DP500, DP780, and DP980, were formed and investigated in this research. In this chapter, the experimental procedures for metal forming and characterization of the specimens are described. The tensile properties, chemistry, and microstructural characteristics of the as-received dual phase steel sheets are presented in Chapter 4.

3.1 Metal Forming Procedure

DP500, DP780, and DP980 sheets were formed under quasi-static condition using the Nakazima test [42] and under high strain rate conditions using EHF [43] with a 34° conical die. The voltage and corresponding energy of EHF tests are summarized in Table 3-1. Also, some specimens were formed under EHF without using a die.

Table 3-1 Input voltage and corresponding energy in EHF tests

	Voltage (kV)	Energy (kJ)
DP500	8.0	10.3
	9.5	14.4
DP780	13.4	28.9
DP980	13.3	28.3
	13.7	30.0

Figure 3-1 and Figure 3-2 schematically show the Nakazima test and EHF set-ups, respectively. As can be seen, there is a punch-sheet contact in the Nakazima test. In the Nakazima test, the sheets were formed in both dry and lubricated conditions. In case of

lubrication, Teflon was used as the lubricant. Dome-shaped and conical specimens were produced in Nakazima test and EHF, respectively.

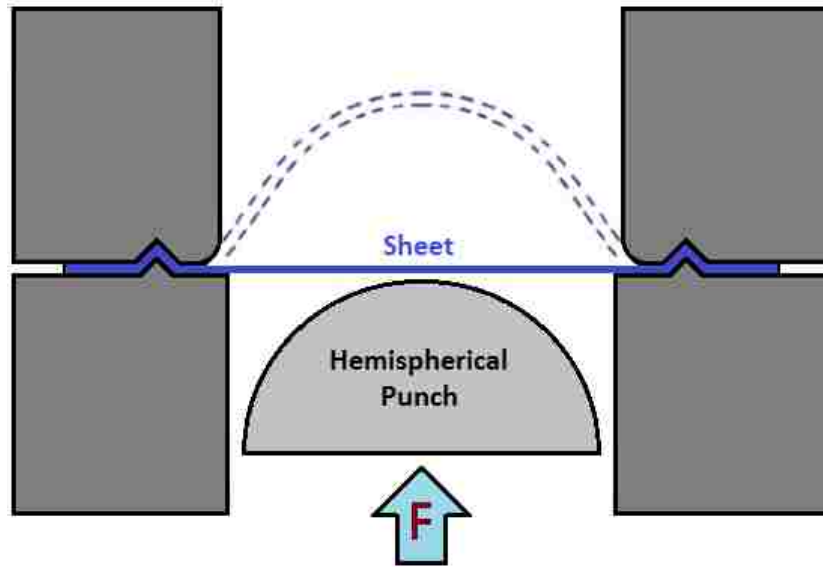


Figure 3-1 Schematic of the Nakazima test

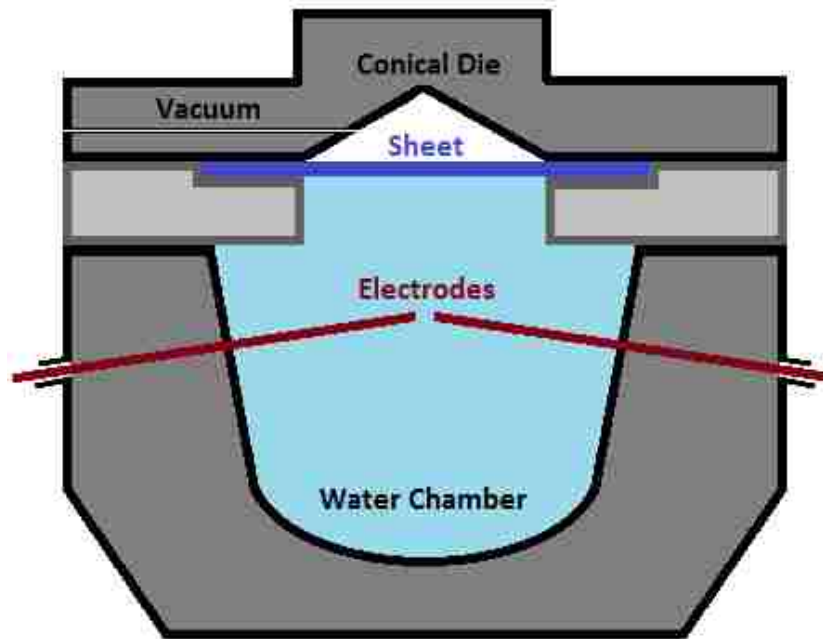


Figure 3-2 Schematic of EHF process

3.2 Macro-strain Measurement

As shown in Figure 3-3, the sheets were electro-etched with a 2.54 mm diameter circle grid prior to deformation. After deformation, the circles were distorted into ellipses, as can be seen in Figure 3-3, with a d_{Major} and d_{Minor} . Minor and major strains, i.e. ϵ_{Minor} and ϵ_{Major} , were measured using an FMTI Model 100 optical strain measurement system in the safe regions. It was found that the level of stains increased from the edge toward the centre of both the Nakazima specimens and EHF specimens.

Measurement of the thickness of the specimens at different strain levels was carried out using an ultrasonic instrument GE Inspection Technologies Ultrasonic CL5. The thickness strain was calculated from the measured thickness as follows:

$$e_T = \frac{T_f - T_{as-rolled}}{T_{as-rolled}} \quad (3-1)$$

$$\epsilon_T = \ln(1 + e_T) \quad (3-2)$$

where e_T and ϵ_T are the engineering and true strains through the thickness of the specimens, respectively. $T_{as-rolled}$ is the initial thickness and T_f is the final thickness at locations of interest.

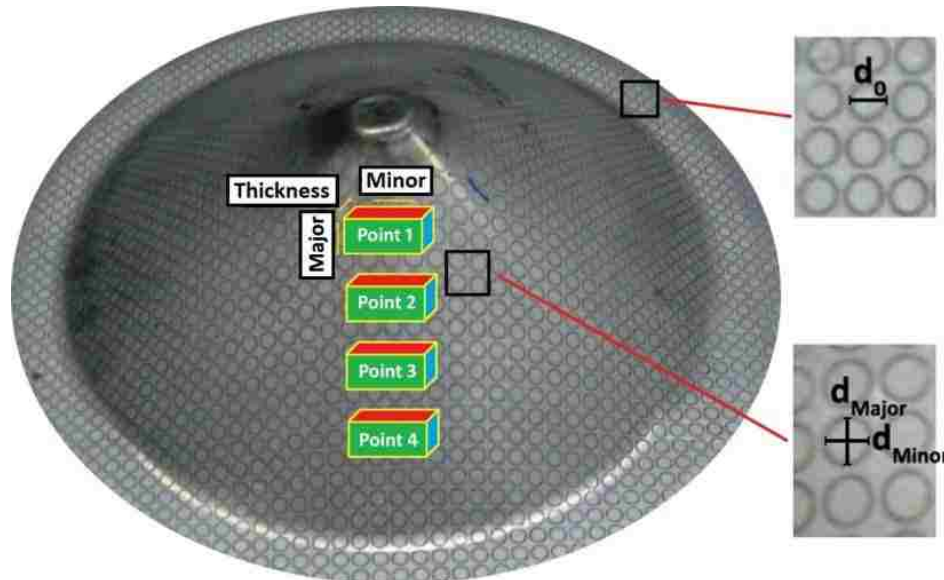


Figure 3-3 Elongated circles on the specimens used for determination of major and minor strains.

Also, according to the principle of volume constancy during plastic deformation:

$$\varepsilon_{Major} + \varepsilon_{Minor} + \varepsilon_T = 0 \quad (3-3)$$

This relationship was used to verify the accuracy of the strain measurements.

The equation below was used to calculate the von Mises effective strain at different points on the specimens:

$$\bar{\varepsilon} = \sqrt{\frac{2}{3}(\varepsilon_{Major}^2 + \varepsilon_{Minor}^2 + \varepsilon_T^2)} \quad (3-4)$$

3.3 Metallography

For microstructural investigations, four 10×10 mm samples were cut from edge-to-centre of each specimen, as shown in Figure 3-4-a. Each sample was cut into three new samples for observation of microstructures in the normal (ND), rolling (RD), and transverse (TD) directions at different strain levels. Electro-discharge machining (EDM) was used to cut the samples to prevent heat generation and further deformation. After cutting the specimens, the three samples taken from the same location were mounted in the same die as shown in Figure 3-4-b. Diallyl Phthalate thermosetting resin was used as the mounting powder and was cured at 150 °C and 20 MPa for 90 seconds.

The mounted samples were ground using BuehlerMet® II Abrasive Discs C with a Grit ANSI of 60 to 600. Polishing was carried out in three steps: MetaDi® Polycrystalline Diamond Suspension of 9 µm, followed by Micropolish® II Deagglomerated Alpha Alumina powders of 1.0 and 0.05 µm. The specimens were etched using Nital 2% for 15-20 s at room temperature. Micrographs were taken at magnifications of ×500 to ×10000 using backscatter electron beams at 15 eV using a scanning electron microscope (SEM) JEOL JSM-5800LV equipped with an EDAX energy dispersive spectrometer.

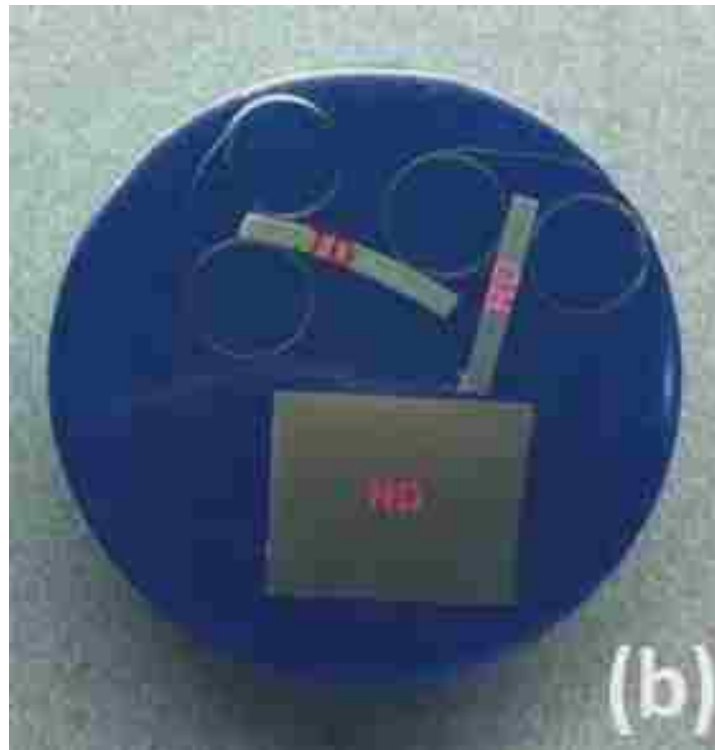
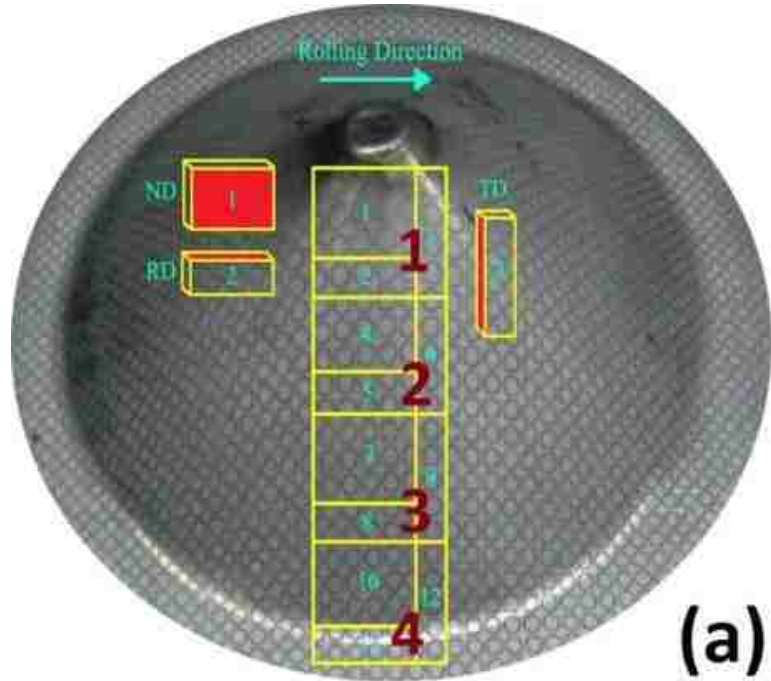


Figure 3-4 (a) The pattern of cutting the samples for metallography, and (b) mounting of the three samples of the same region into one die.

3.4 Quantitative Metallography

3.4.1 Micro-strain Measurement

Micro-strains in the ferrite grains and martensite islands were measured by quantitative analysis of high resolution scanning electron microscope images using the commercial image analysis software Clemex Vision Pro 3.5.

According to Figure 3-4-b, the RD part of each sample was used for quantitative metallography, since the strain level was constant throughout it.

Since the sizes of the constituent phases in the microstructure observed in the normal direction were dependent upon the amount of grinding that was applied during the sample preparation, normal microstructures were not useful for quantitative metallography. Therefore, in order to measure the elongations of the ferrite and the martensite, through-thickness micrographs were analyzed. Determination of the size of martensite islands in DP980 was not possible due to the continuous network of martensite in the microstructure. So, quantitative metallography was carried out only on DP500 and DP780 specimens.

The ferrite mean grain size and the martensite island mean size were measured from the edge to the centre of the specimens using the RD microstructures. All measurements were carried out within safe ferrite grains and martensite islands, where no voids or micro-cracks were observed. Minor and through-thickness micro-strains were calculated as follows:

$$e = \frac{d_f - d_{as-rolled}}{d_{as-rolled}} \quad (3-5)$$

$$\varepsilon = \ln(1 + e) \quad (3-6)$$

where e and ε represent the engineering and true strains, respectively. $d_{as-rolled}$ is the initial mean size of ferrite grains or martensite islands in the as-rolled specimens, and d_f is the mean size after deformation. $d_{as-rolled}$ and d_f were calculated using the image

analysis software in the minor and thickness directions to determine ϵ_{Minor} and $\epsilon_{Thickness}$. By considering the volume constancy, ϵ_{Major} was calculated as:

$$\epsilon_{Major} = -(\epsilon_{Minor} + \epsilon_{Thickness}) \quad (3-7)$$

To evaluate the results, the 95% Confidence Intervals (**95% CI**) and Relative Accuracy percent (**%RA**) were calculated according to ASTM E1382-97 [231]:

$$95\%CI = \pm \frac{t \cdot s}{\sqrt{N}} \quad (3-8)$$

$$\%RA = \frac{95\%CI}{\bar{X}} \cdot 100 \quad (3-9)$$

where s is the standard deviation, N is the number of the measured grains, \bar{X} is the grain mean size, and t is a multiplier as a function of N which is 1.960 for $N > 60$. According to the standard, a 10 %RA (or lower) is considered to be an acceptable precision for most purposes.

3.4.2 Martensite Content

As it is described in Section 0, the microstructure of dual phase steel sheets varied from the surface to the middle of the sheet. Hence, general microstructural characteristics of the steels, such as martensite content, should be determined by analysis of through-thickness micrographs. To determine martensite content of the steels, through-thickness micrographs of the steels were captured at $\times 200$ magnification in such a way that the entire thickness of the sheet was visible in the image. Quantitative metallography was carried out using the Clemex Vision Pro 3.5 image analysis software.

3.4.3 Analysis of the Voids

In order to observe the voids, as-polished samples were slightly etched for 2-3 s just to remove the plastic layer but not to etch the microstructure. Hence, voids were relieved as the dark areas in a white matrix. The sequence for the quantitative analysis of voids is shown in Figure 3-5. Micrographs of the voids were taken at several strain

levels from the edge to the centre of the specimens throughout the TD samples using an optical microscope Leitz Laborlux 12ME equipped with a Paxit PAXcam imaging system. The contrast of the micrographs was enhanced in Adobe Photoshop 7.0 ME software to distinguish between the voids (black) and the matrix (white). The new image was analyzed in Clemex Vision Pro 3.5 where void volume fraction was determined as the number of red pixels over the total number of pixels. The software also provided detailed statistical data which were used for analysis of void growth.

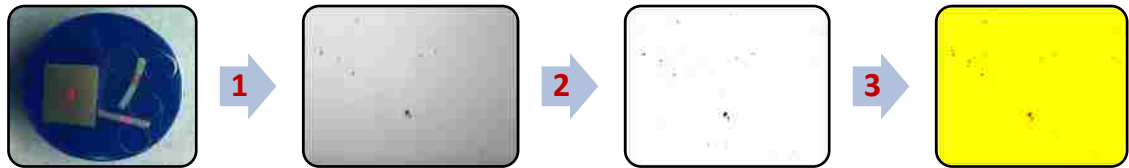


Figure 3-5 Sequence for the quantitative analysis of voids, 1: micrograph of TD part, 2: enhancement of contrast of the micrograph, 3: micrograph in the image analysis software

3.5 Microhardness Test

Microhardness measurements were carried out using Vickers indenter according to ASTM E384-11e1 [232] using a Buehler Micromet II equipped with a Vickers indenter. The hardness of the steels and ferrite grains were determined as a function of strain as described in Table 3-2. Since the size of the martensite islands was smaller than the size of the indentation even under a load of 10 g, it was not possible to carry out hardness tests inside the martensite islands. However, by applying a load of 25 g, the size of the indentation was sufficiently small to be located inside a ferrite grain.

The Vickers hardness was calculated according to:

$$HV = \frac{0.1891F}{d_{avg}^2} \quad (3-10)$$

where F is the indenter force in Newtons and d_{avg} is the average of the two pyramidal lengths in millimeters.

Table 3-2 Conditions for the microhardness test

	Orientation	Load (g)	Time (s)
Steels	Normal direction	300	20
Ferrite grains	Normal direction	25	15

3.6 Fractography

Fracture surfaces were observed in the specimens formed under both quasi-static and high strain rate conditions. A field emission scanning electron microscope FEI Quanta 200 FEG equipped with an EDAX energy dispersive spectrometer was utilized for fractography using secondary electron beams at 5 eV. As it is shown in Figure 3-6, fractured surfaces were studied at different magnifications from $\times 200$ to $\times 10000$.

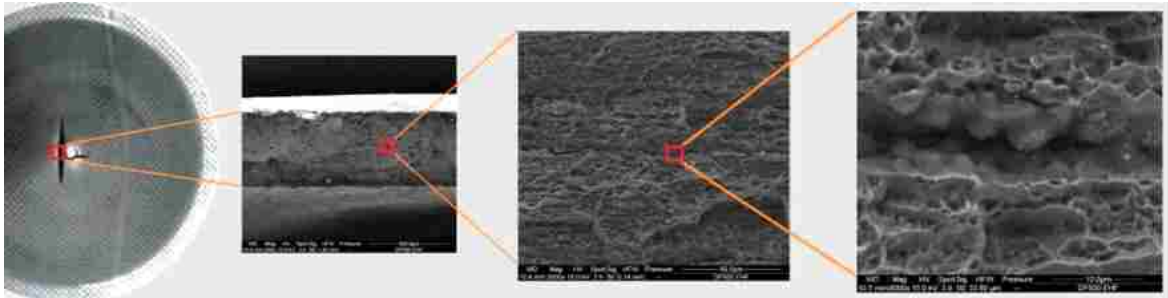


Figure 3-6 Fractography of the specimen at different magnifications

3.7 Nano-scale Observations

Nano-scale observations were carried out using transmission electron microscopy (TEM). Sample preparation and TEM were carried out at the Canadian Centre for Electron Microscopy (CCEM) at McMaster University using TEM FEI Titan 80-300 Cryo.

CHAPTER 4

4 Materials Characterization

In this chapter, the properties of the as-received dual phase steel sheets are presented.

4.1 Tensile Properties

Three commercial Fe-C-Mn dual phase steel sheets, i.e. DP500, DP780, and DP980, were formed and investigated in this research. Three grades of dual phase steels, i.e. DP500, DP780, and DP980 were investigated in this research. The number after DP indicates the minimum value of ultimate tensile strength (UTS) in the steel. For instance, the UTS of DP500, DP780, and DP980 are equal or greater than 500, 780, and 980 MPa, respectively. Table 4-1 presents the characteristics of the steel sheets provided by the suppliers.

Table 4-1 Characteristics of the as-received dual phase steel sheets

Steel Grade	Martensite (vol%)	Thickness (mm)	σ_Y (MPa)	σ_{uts} (MPa)	ϵ_{unif} (%)	ϵ_{tot} (%)	n	K (MPa)	Coating
DP500	10	0.65	341	565	14.7	26.0	0.15	878	Electro-galvanized
DP780	23	1.0	507	859	12.6	16.9	0.13	1290	Hot dip galvanized
DP980	34	1.0	573	1003	9.8	15.1	0.106	1426	Electro-galvannealed

4.2 Chemical Composition

Table 4-2 shows the chemical composition of the alloys which was determined according to ASTM E1019-08 [233], ASTM E1097-07 [234] and ASTM E1479-99 [235] using an Inductively Coupled Plasma (ICP) Spectrometry Agilent Technologies 725 ICP-OES.

As it can be seen Mn is the major alloying element in the steel. Hence, dual phase steels are sometimes described as Fe-Mn-C steels. In the case of DP500, the presence of Mn and a slight amount of other alloying elements was enough to reach the desired strength. However, DP780 and DP980 include greater amounts of Mo and Cr to make stronger solid solutions. Among the alloying elements, carbon provides interstitial solid solution. During the processing of dual phase steels, the allowable fraction of carbon in ferrite is much smaller than austenite. Therefore, after quenching of the steel to room temperature and the consequent transformation of austenite to martensite, most of the carbon atoms are located in martensite. The amounts of carbon in the three dual phase steels were adjusted according to the desired content and hardness of martensite in the microstructures. For instance, since the volume fraction of martensite in DP500 is much smaller than in DP780 or in DP980, the carbon content in the DP500 was reduced the most.

Alloying element distribution maps obtained by X-ray mapping of through-thickness microstructures using the EDAX energy dispersive spectrometer on the scanning electron microscope FEI Quanta 200 FEG. The elements were reasonably found to distribute homogeneously in the microstructure. For instance, Figure 4-1 shows the distributions of C, Mn, Mo, and Cr in DP780.

Table 4-2 Characteristics of the as-received dual phase steel sheets

Steel Grade	C	Mn	Mo	Cr	Ni	Si	P	S
DP500	0.063	1.83	<0.01	0.03	0.01	0.02	0.01	0.012
DP780	0.13	2.01	0.18	0.25	0.01	0.03	<0.01	0.006
DP980	0.11	2.27	0.33	0.24	0.01	0.04	0.01	<0.005

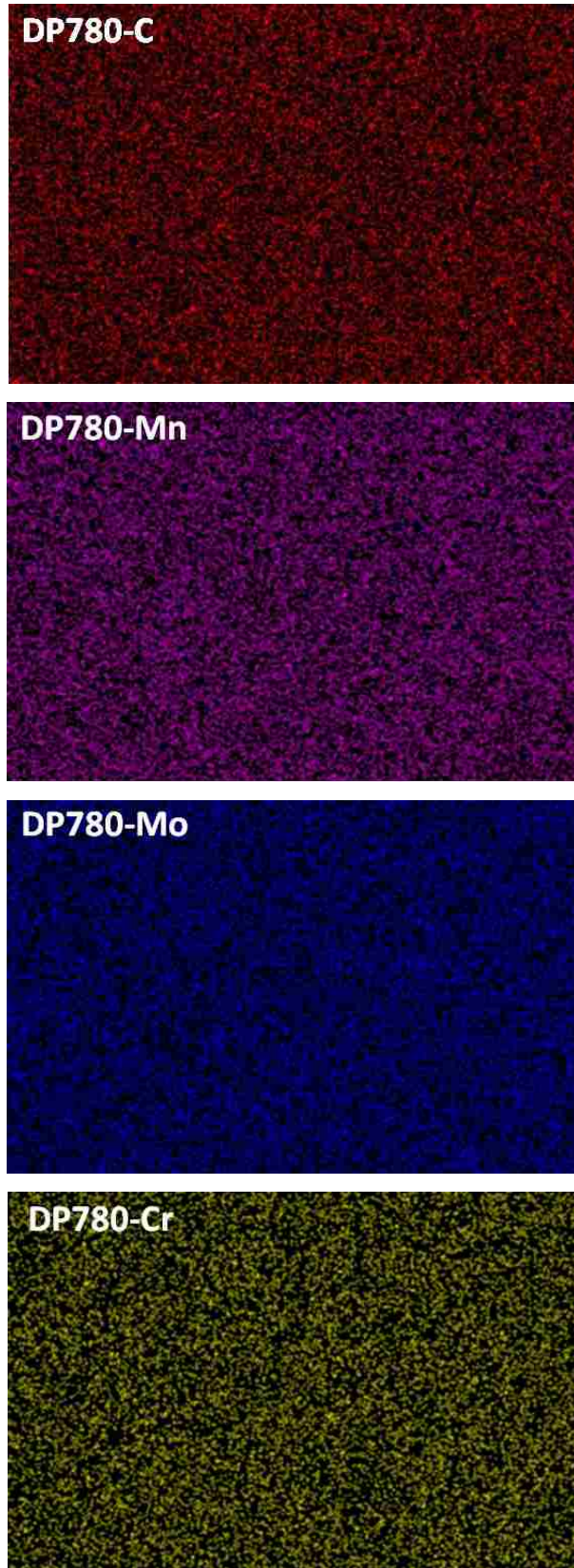


Figure 4-1 Distribution of some alloying elements in DP780 captured by X-ray mapping

4.3 X-ray Analysis

X-ray diffraction analyses were conducted to identify the various phases present in the steels using a X-ray Diffraction Rigaku D/MAX-1200 with a Cu target ($\lambda=1.51478 \text{ \AA}$) and a Ni filter. Figure 4-2 shows the XRD patterns of the as-rolled specimens. As it can be seen, only ferrite and martensite peaks were identified, so the fraction of retained austenite and other possible phases was considered to be negligible. In case of DP980, although no evidence of bainite was observed in the microstructure, formation of bainite was possible during the electro-galvannealing process.

General Microstructure Figure 4-3, Figure 4-4, and Figure 4-5 show the microstructures of DP500, DP780, and DP980 in the normal direction and through thickness of the sheet, respectively. As it can be seen, martensite islands are located at the ferrite grain boundaries. The reason is that during the intercritical annealing of dual phase steels, austenite nucleated at the grain boundary and after quenching these austenite grains transformed into martensite. Due to the low martensite volume fraction of DP500, martensite islands were separated and clearly identified. However, higher martensite volume fraction in DP780 created a partial martensite network in some areas but also separated martensite islands can be found. As can be seen in Figure 4-5, the high content of martensite in DP980 resulted in almost a continuous martensite network. Figure 4-3-b, Figure 4-4-b, and Figure 4-5-b show the through-thickness microstructure of the sheets which includes martensite banding. As mentioned in Section 2.1.3, microstructure banding in the dual phase steel sheets occurred due to elemental segregation during dendritic solidification followed by cold rolling. By increasing the martensite volume fraction, i.e. from DP500 to DP980, the ferrite mean grain size was decreased, while the martensite mean size was increased. Also, the through-thickness micrographs show that the ferrite and martensite mean sizes increased from the surface to the middle of the sheets. For this reason, any quantitative metallography should be carried out using the through-thickness micrographs.

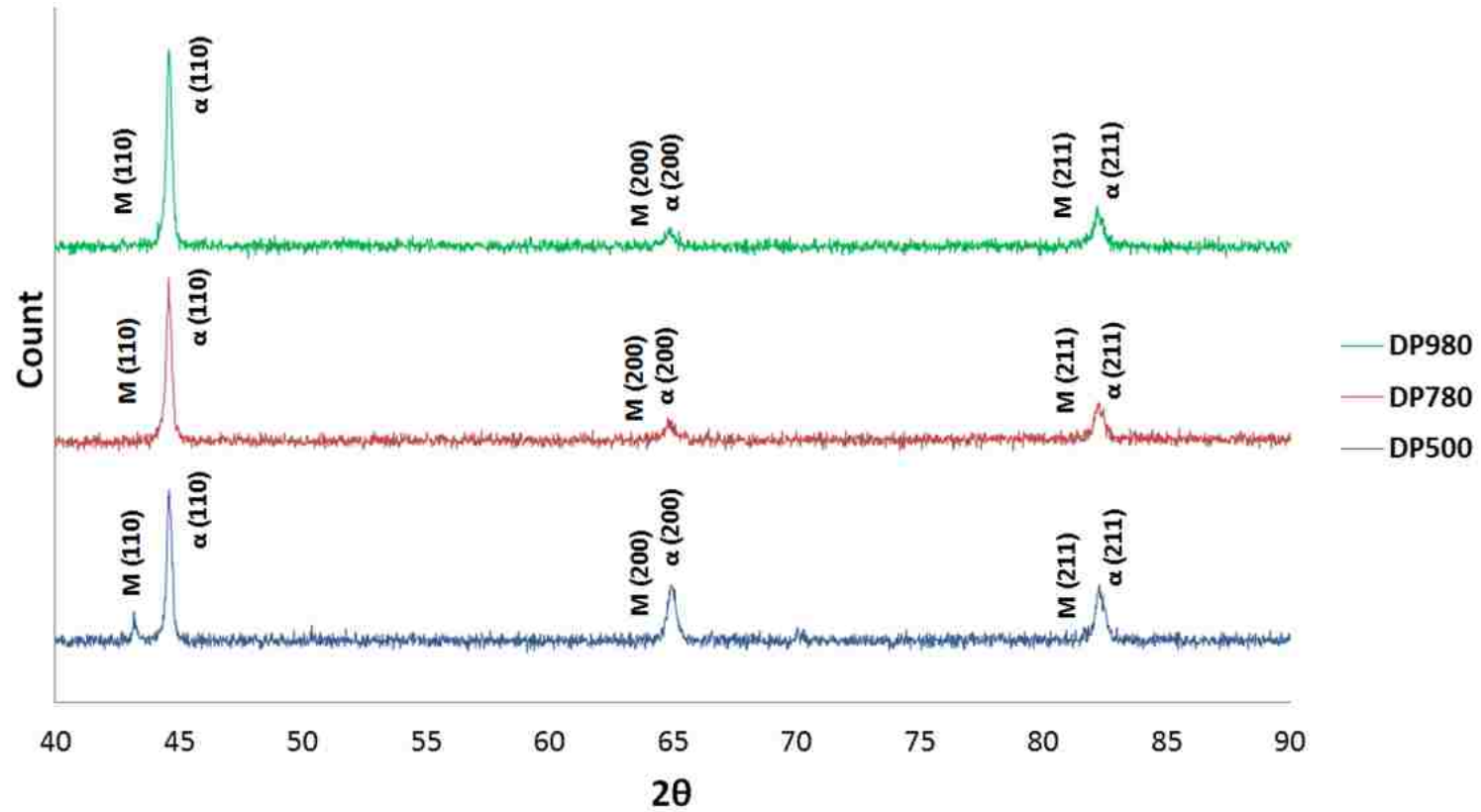


Figure 4-2 X-ray diffraction patterns of the dual phase steels include ferrite and martensite peaks

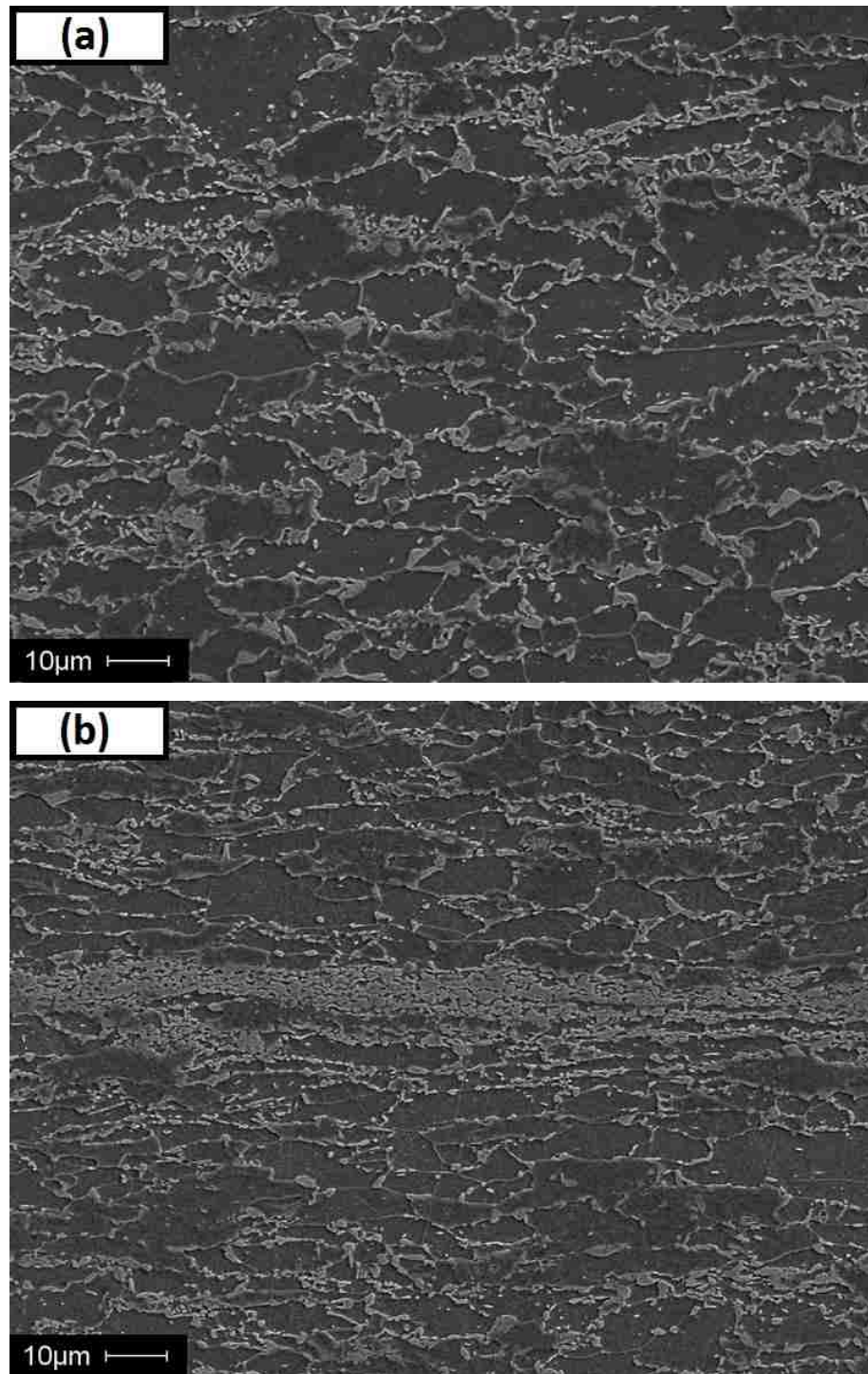


Figure 4-3 Microstructure of DP500: (a) normal direction, and (b) through thickness. The darker phase is ferrite and the light gray phase is martensite. Small particles of carbides are distributed in ferrite grains.

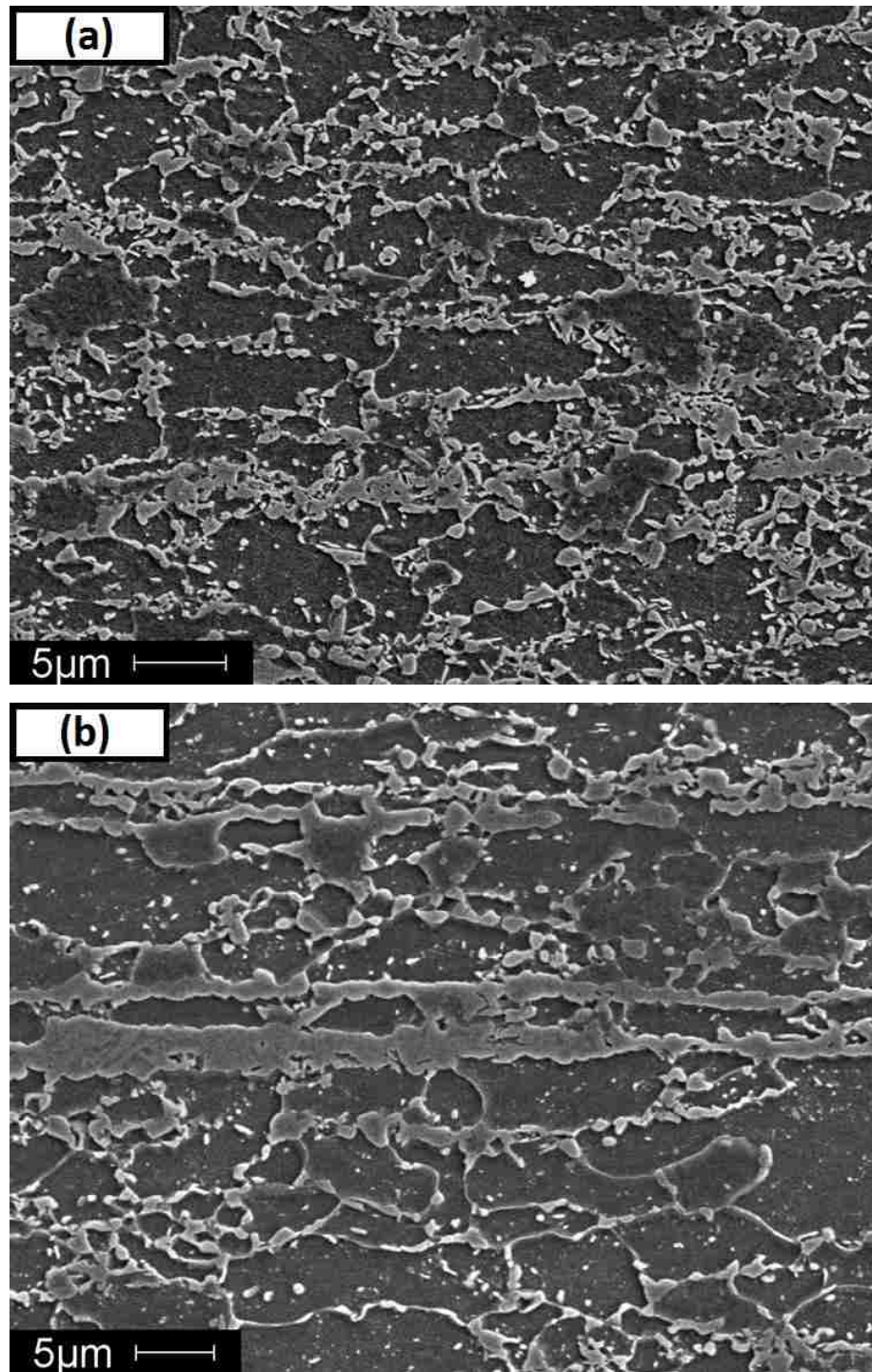


Figure 4-4 Microstructure of DP780: (a) normal direction, and (b) through thickness. The darker phase is ferrite and the light gray phase is martensite. Small particles of carbides are distributed in ferrite grains.

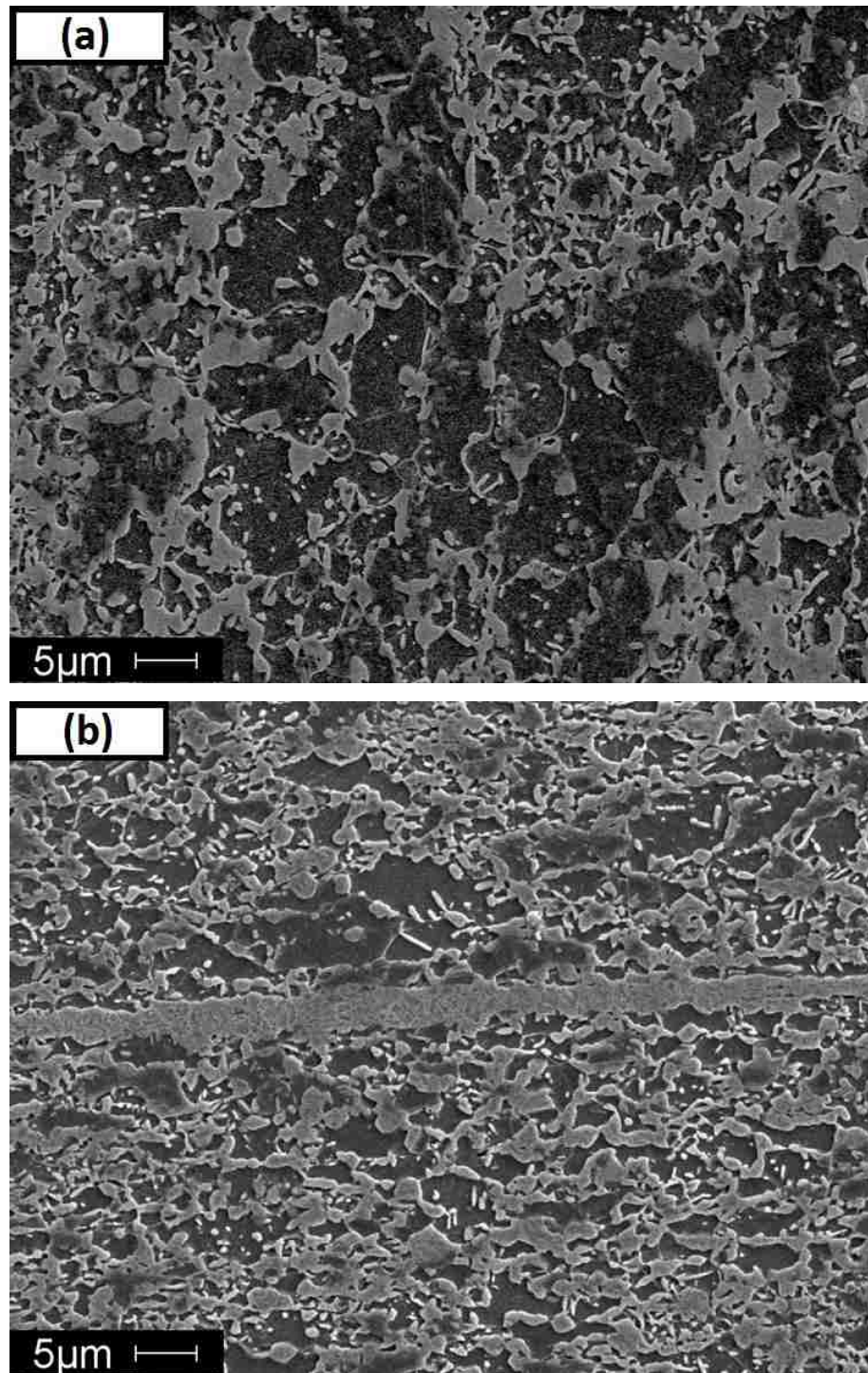


Figure 4-5 Microstructure of DP980: (a) normal direction, and (b) through thickness. The darker phase is ferrite and the light gray phase is martensite. Small particles of carbides are distributed in ferrite grains.

4.4 Carbon Content and Crystallography of Martensite

The mechanical behaviour of martensite significantly depends on its carbon content. The carbon in dual phase steels is distributed between ferrite and martensite according to the mixture rule:

$$C\% = C_F V_F + C_M V_M \quad (4-1)$$

where $C\%$, C_F , and C_M are the carbon content of steel, ferrite, and martensite respectively, and V_F and V_M are the volume fraction of ferrite and martensite, respectively.

The carbon content in ferrite at room temperature can be approximately assumed to be zero compared to the carbon content of martensite, hence:

$$C\% = C_M V_M \Rightarrow C_M = \frac{C\%}{V_M} \quad (4-2)$$

According to the volume fraction of martensite and carbon content of the steels presented in Table 4-1 and Table 4-2, respectively, the carbon content of martensite in the dual phase steels are:

$$C_{M,DP500} = \frac{0.063}{0.10} = 0.63\%$$

$$C_{M,DP780} = \frac{0.13}{0.23} = 0.57\%$$

$$C_{M,DP980} = \frac{0.11}{0.34} = 0.32\%$$

So, the hardness of the martensite in the dual phase steel grades decreases from DP500 to DP780 and DP980.

As it was mentioned in Section 2.1.5, when the martensite carbon content is below 0.59, the tetragonality of the martensite is unity and the lattice parameters of martensite, i.e. a and c , are equal to the lattice parameters of pure iron. According to the estimated carbon contents of the martensite phases in DP500, DP780, and DP980, the crystallography of martensite in the dual phase steels is similar to the crystallography of ferrite.

CHAPTER 5

5 Investigations on the Formability of Nakazima and EHF Specimens

5.1 Nakazima Specimens

Figure 5-1 and Figure 5-2 show the dome-shaped Nakazima specimens formed in dry and lubricated conditions, respectively. As can be seen, the quality of the markings after forming was very good which was essential for accurate strain measurements.

As it can be seen in Figure 5-1, necking and cracking occurred between the edge and the centre of the domes in all of the specimens formed in a dry condition. This necking pattern can occur due to the effect of friction forces or high speed forming. But since the Nakazima specimens were formed in a quasi-static condition, the only reason for this type of failure is because of the influence of friction which reduces the symmetry of deformation.

As it is shown in Figure 5-2-b and c, when DP780 and DP980 are formed in the lubricated condition, the effect of friction was significantly reduced. Hence, necking and cracking occurred at the apex of the domes in the centre of the specimens. In the case of DP500 specimens, necking occurred away from the apex and this may be due to insufficient lubrication or to the combined effect of a thinner gauge and a lower flow stress. In other words, since the flow stress and the sheet thickness of DP500 were less than those of the DP780 and DP980 sheets, a small amount of friction may have affected the symmetry of the deformation.

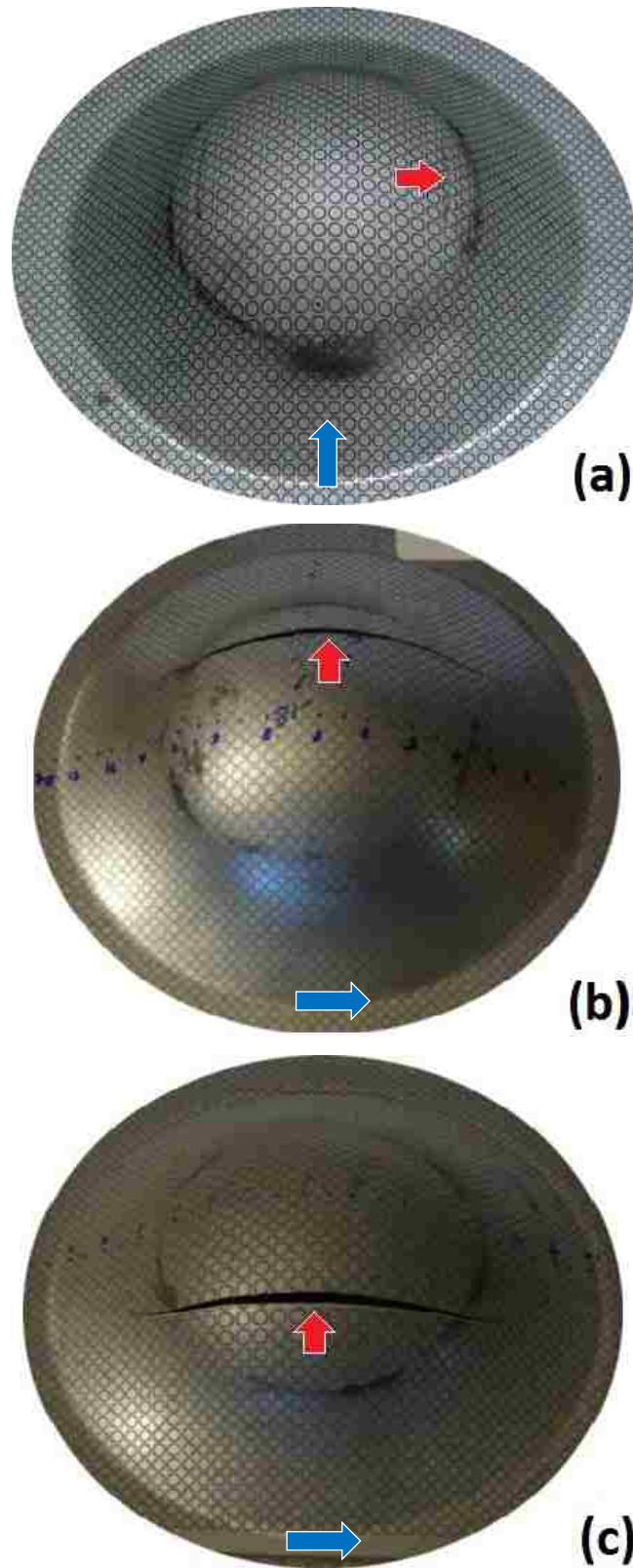


Figure 5-1 Nakazima specimens formed without lubricant: (a) DP500, (b) DP780, and (c) DP980. The rolling direction and cracking are shown by the red and blue arrows, respectively.

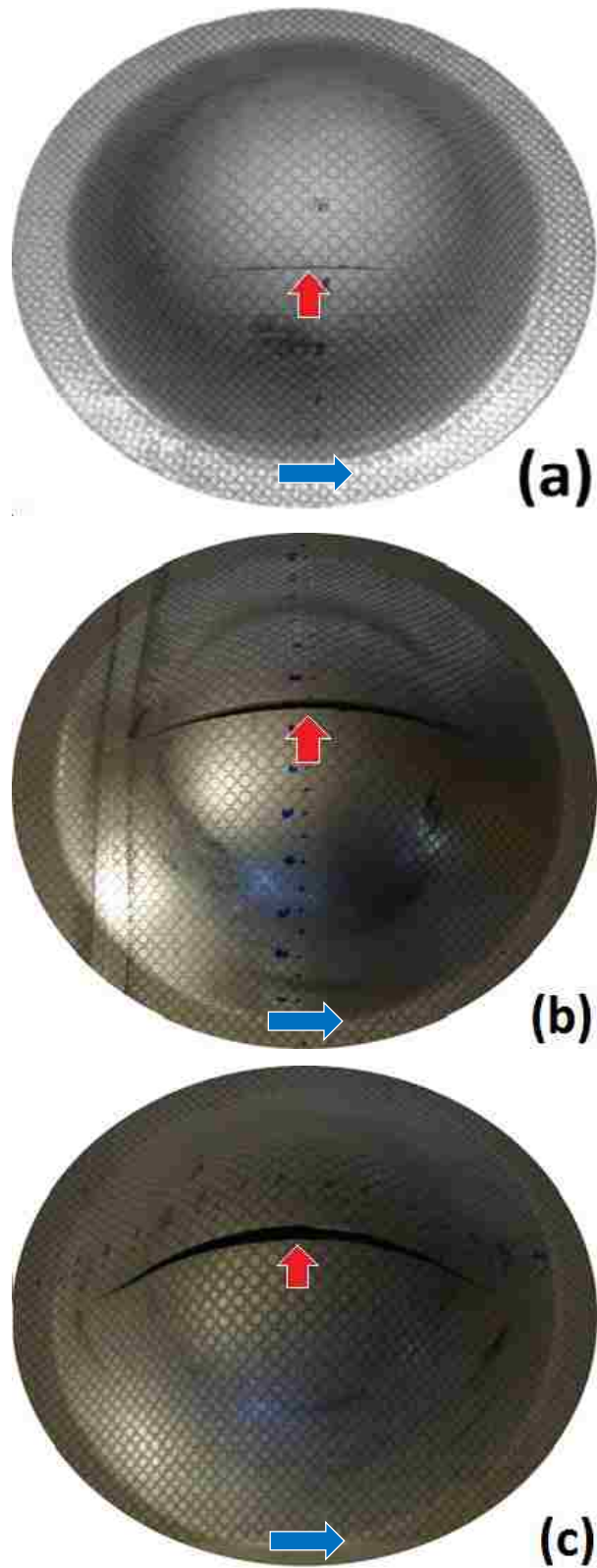


Figure 5-2 Nakazima specimens formed with lubricant: (a) DP500, (b) DP780, and (c) DP980. The rolling direction and cracking are shown by the red and blue arrows, respectively.

5.2 EHF Specimens

Figure 5-3 and Figure 5-4 show the conical specimens formed under EHF using a 34° conical die. In these EHF experiments, although there were strong contact forces between the sheet and the die, the successful electro-etching of the circle grids on the blanks resulted in a reliable contrast for accurate determination of minor and major strains.

As indicated in Table 3-1, DP500 and DP980 were formed with different levels of energy. When formed with the lower levels of energy, cracking occurred at the top of the specimens, as shown in Figure 5-3. However, when a slightly higher discharge energy was applied, rebounding occurred at the tip of the conical specimens, as seen in Figure 5-4. DP780 specimens were formed only at one level of energy. As displayed in the figures, rebounding occurred in both specimens; however, cracking also happened in one of the specimens.

Investigations showed no tangible difference between the microstructure of the cracked and rebounded specimens. Hence, rebounded specimens were used for characterization of deformation and cracked specimens were used for characterization of failure and fracture.

Figure 5-5 shows the DP500 and DP780 specimens formed under EHF without using a die, i.e. free forming. As can be seen, large splits occurred on the free formed specimens. These specimens indicated that controlling the effect of the strong shock waves on the blank is not practical without using a die.

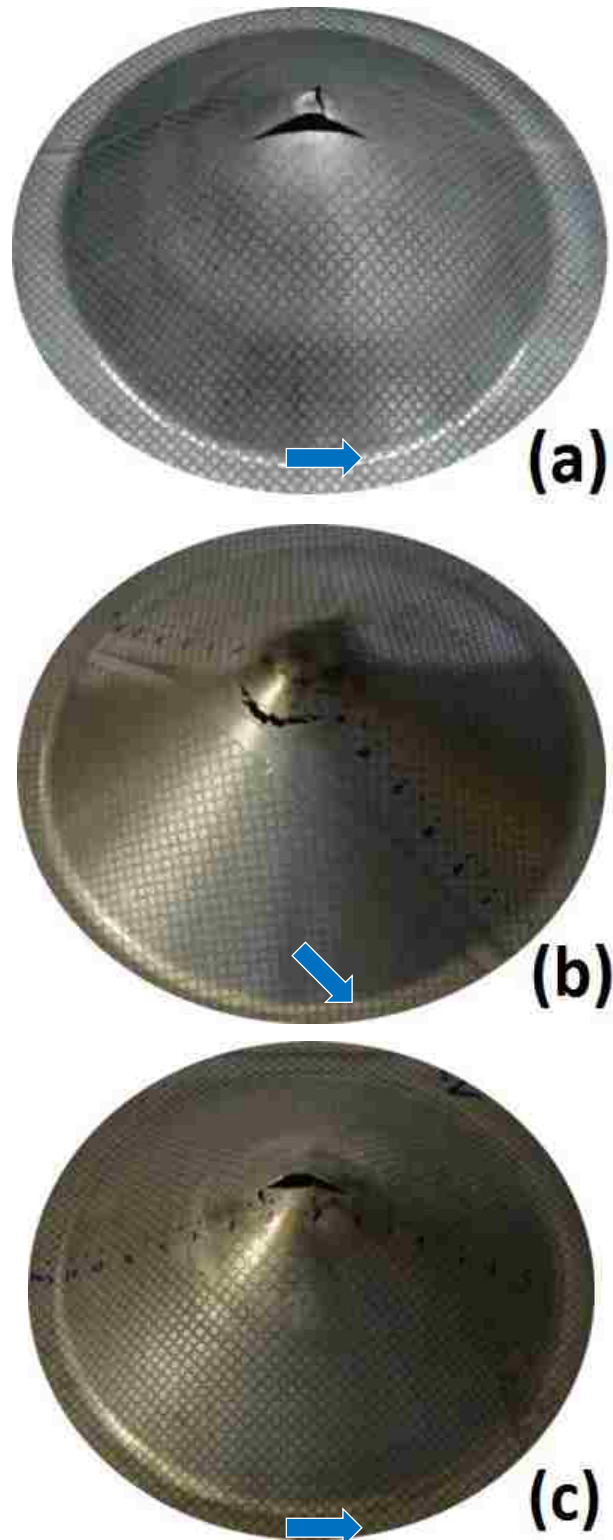


Figure 5-3 Specimens formed under EHF using the conical die showing a crack on the tip of the cone: (a) DP500 formed at 8.0 kV, (b) DP780 formed at 13.4 kV, and (c) DP980 formed at 13.3 kV.

The rolling direction is shown by the blue arrow.

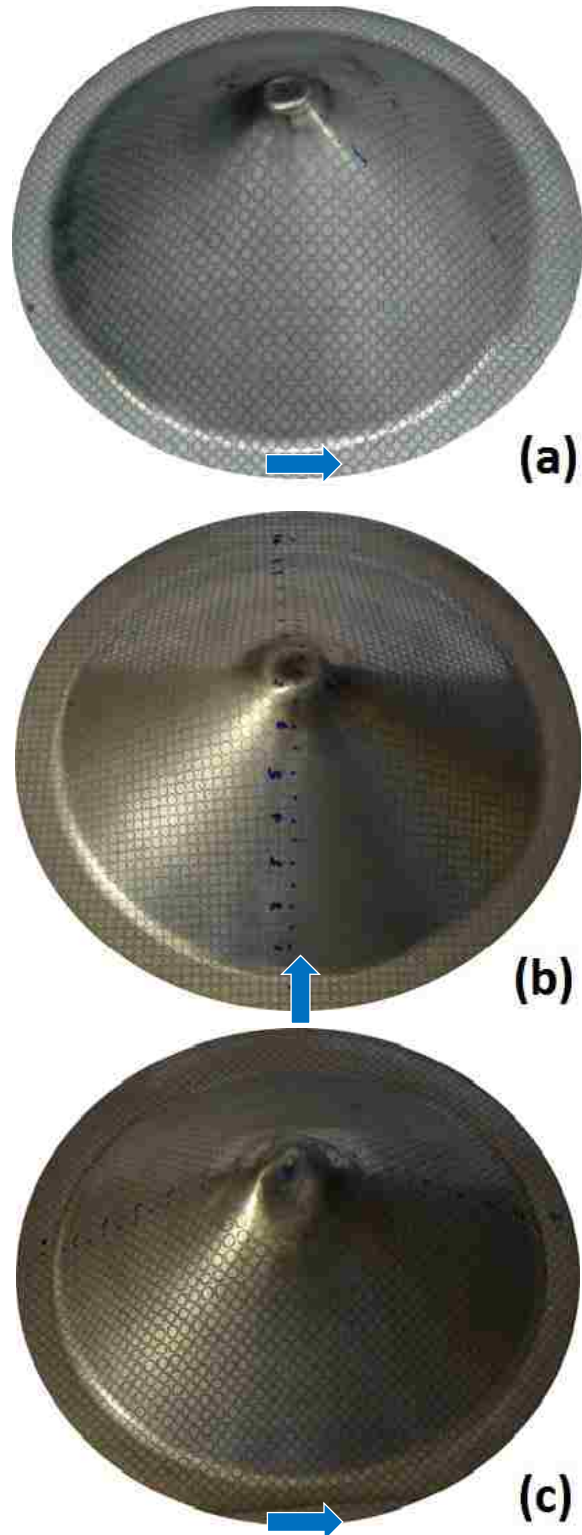


Figure 5-4 Specimens formed under EHF using the conical die showing rebounding on the tip of the cone: (a) DP500 formed at 9.5 kV, (b) DP780 formed at 13.4 kV, and (c) DP980 formed at 13.7 kV.

The rolling direction is shown by the blue arrow.

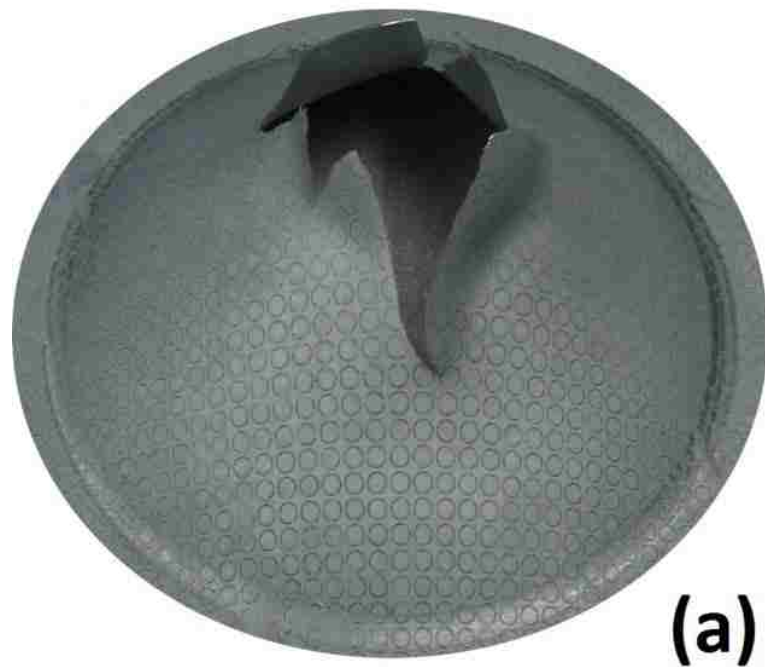


Figure 5-5 (a) DP500 and (b) DP780 specimens formed under EHF without using a die.

5.3 Distribution of Equivalent Strain in the Specimens

In order to gain a better understanding of the distribution of deformation and the necking in the Nakazima specimens and EHF specimens formed into the conical die (cracked specimens), Figure 5-6, Figure 5-7, and Figure 5-8 show the von Mises effective strain across the diameter of DP500, DP780, and DP980 specimens, respectively.

As previously indicated, for the Nakazima specimens formed under dry conditions, the maximum strains in the vicinity of necking did not occur at the top of the dome due to the friction between the sheet and the hemispherical punch. However, by lubricating the DP780 and DP980 sheets prior to forming, the effect of friction was significantly reduced, and the maximum strain was achieved at the apex of the dome.

Since EHF relies on water pressure to form the sheet, there is no friction on the underside of the sheet which leads to a more uniform distribution of strain, compared to the Nakazima test where friction forces act between the sheet and the die. However, to obtain symmetry in the conical specimens formed in EHF, the electrodes should be precisely located in the appropriate positions.

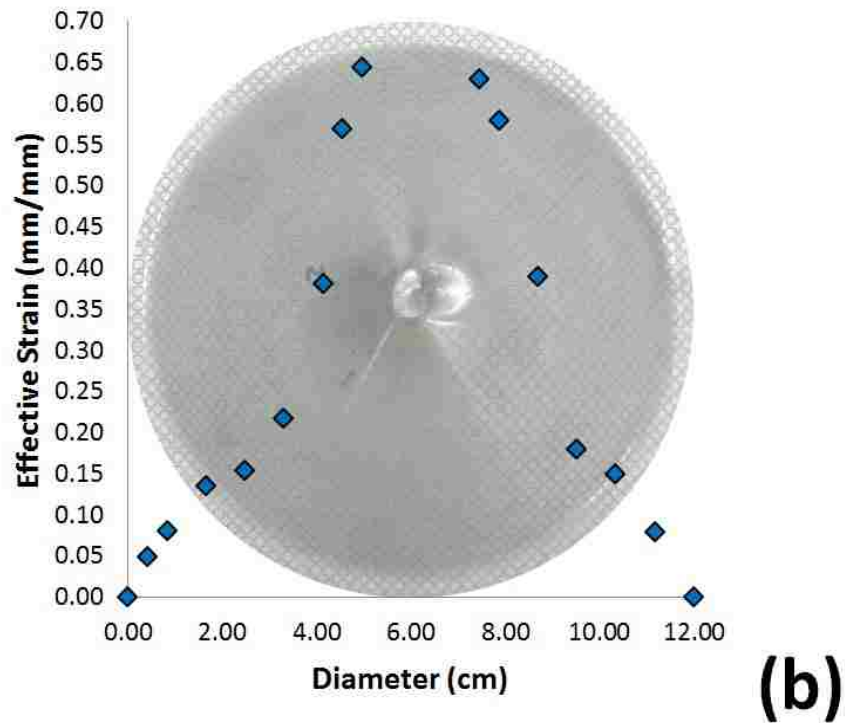
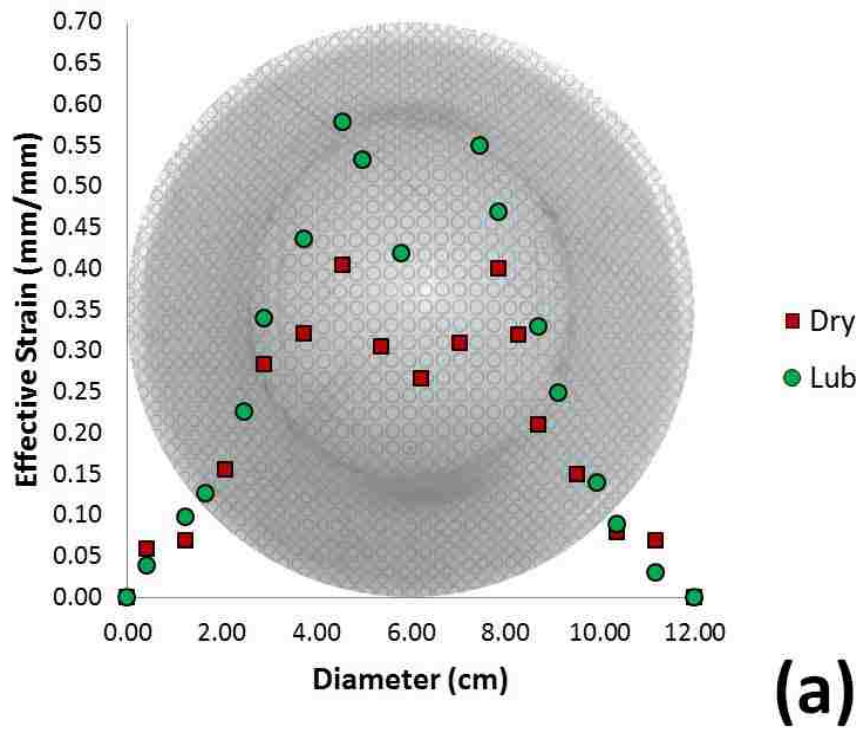


Figure 5-6 Distribution of effective strain across the diameter of the specimens in rolling direction: DP500 formed under (a) Nakazima test, (b) EHF.

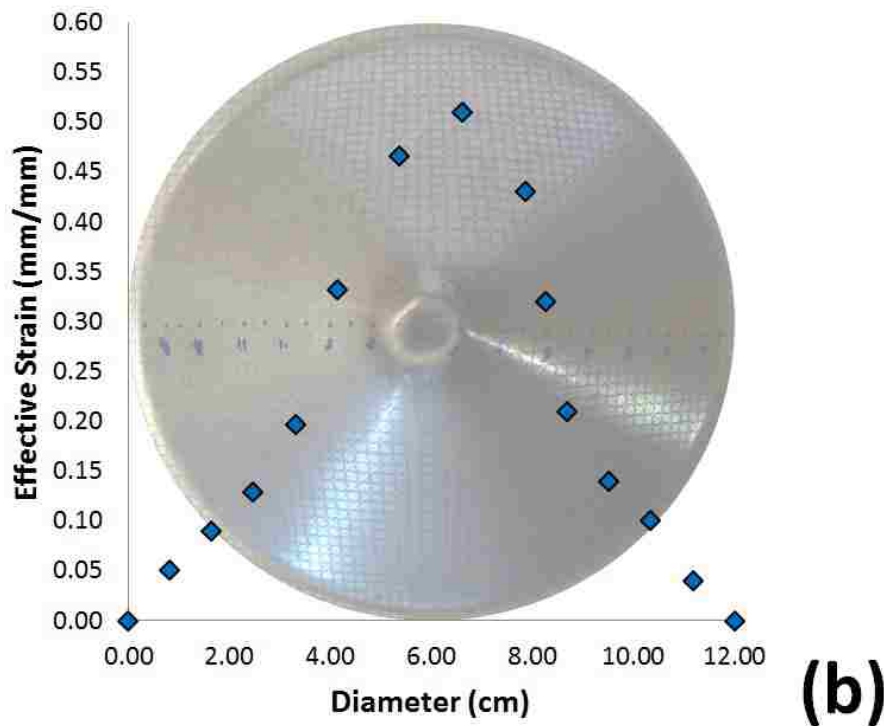
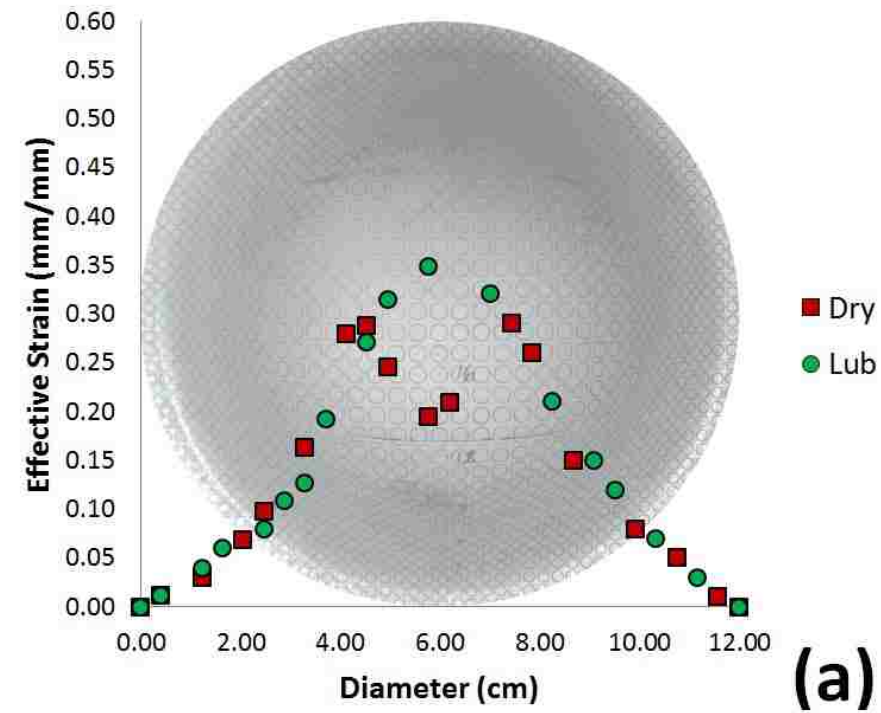
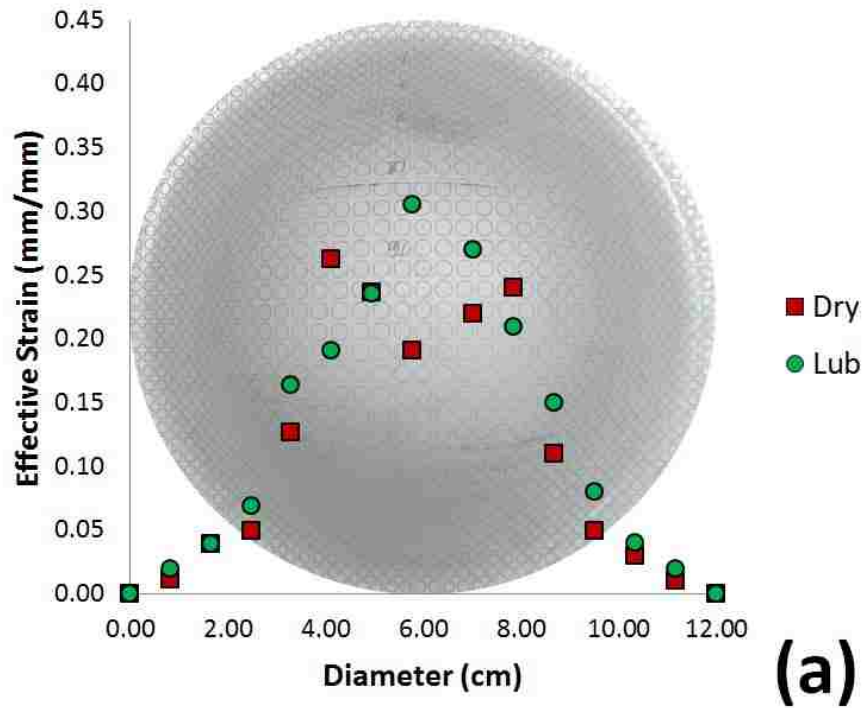
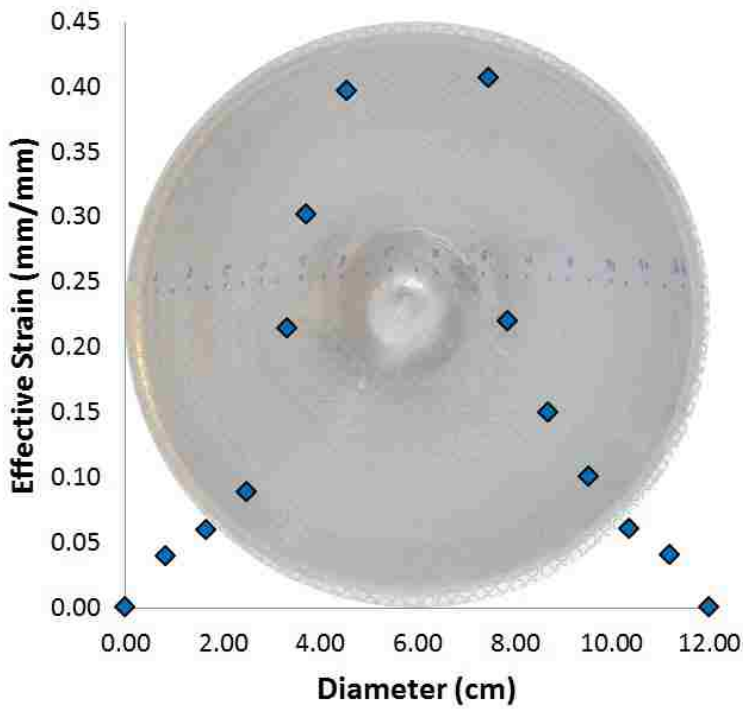


Figure 5-7 Distribution of effective strain across the diameter of the specimens in rolling direction: DP780 formed under (a) Nakazima test, (b) EHF.



(a)



(b)

Figure 5-8 Distribution of effective strain across the diameter of the specimens in rolling direction: DP980 formed under (a) Nakazima test, (b) EHF.

CHAPTER 6*

6 Characterization of Hyperplasticity in Dual Phase Steels

As indicated in Section 2.3, it is expected that under certain high strain rate forming conditions, significant formability improvement occurs in strain rate sensitive materials which is known as hyperplasticity. In this chapter, the formability improvement in the specimens formed under EHF compared to the specimens formed under Nakazima test is qualitatively investigated. There were two sets of EHF specimens: die formed specimens and free formed specimens. Preliminary investigations showed the occurrence of a remarkable formability improvement in die formed specimens compared to the specimens formed under Nakazima test; however, there was no formability improvement in the free formed specimens. It can be concluded that although the high strain rate condition was necessary to reach hyperplasticity it was not sufficient. As indicated in Section 2.3.3, the die effect and inertial ironing play a key role to achieve hyperplasticity which did not exist during EH free forming.

The formability improvement in the specimens formed under EHF using a 34° conical die was investigated at different levels of observation:

macro-scale: in terms of minor vs. major strains,

micro-scale: in terms of elongation of ferrite grains and martensite islands,

nano-scale: in terms of deformation mechanisms.

Attempts were also made to describe the correlations between the different scales, in order to reach a better understanding of hyperplasticity in dual phase steels.

* This chapter contains material that is the outcome of the joint research.

6.1 Macro-scale Characterization of Hyperplasticity

Figure 6-1-a, Figure 6-2-a, and Figure 6-3-a present the major vs. minor strains which were determined across the DP500, DP780, and DP980 specimens in the safe forming zone, respectively. The inclined dashed lines in Figure 6-1-a, Figure 6-2-a, and Figure 6-3-a present the mode of equibiaxial tension.

Figure 6-1-b, Figure 6-2-b, and Figure 6-3-b display quasi-static forming limit diagrams (FLDs) of the dual phase steels investigated in this research. Detailed information on the experimental work that yielded these forming limit curves (FLCs) is available in a paper by Golovashchenko et al. [236]. The greatest major vs. minor strains that were achieved in the safe zones of the specimens formed under EHF are shown on the FLDs. The vertical red lines display the formability improvement in EHF compared to quasi-static forming. As can be seen, a small formability improvement occurred in DP500 steel whereas remarkable formability improvements occurred in the DP780 and DP980 specimens formed under EHF. The relative formability improvement in DP500 specimen formed under EHF is much less than that of DP780 and DP980 steels. This is generally true for softer materials; since ductile materials already have good formability under quasi-static conditions, they tend to experience less relative formability improvement in high strain rate forming [165]. The greatest relative formability improvement was found for DP780, since its quasi-static formability was poor. Comparing Figure 6-2-b, and Figure 6-3-b, the quasi-static FLC of DP780 was even below the FLC of DP980. The early fracture of DP780 compared to DP980 can be attributed to the harder martensite phase in DP780 ($C_{M,DP780}=0.57 > C_{M,DP980}=0.32$) which results in early cracking in the martensite phase at unexpectedly low strain levels.

It should be noted that the strain path was close to equibiaxial tension in both the Nakazima specimens that formed with lubrication and the EHF specimens. Consequently, the formability improvement that is observed is specific to this particular mode of deformation and may be different for other modes of deformation.

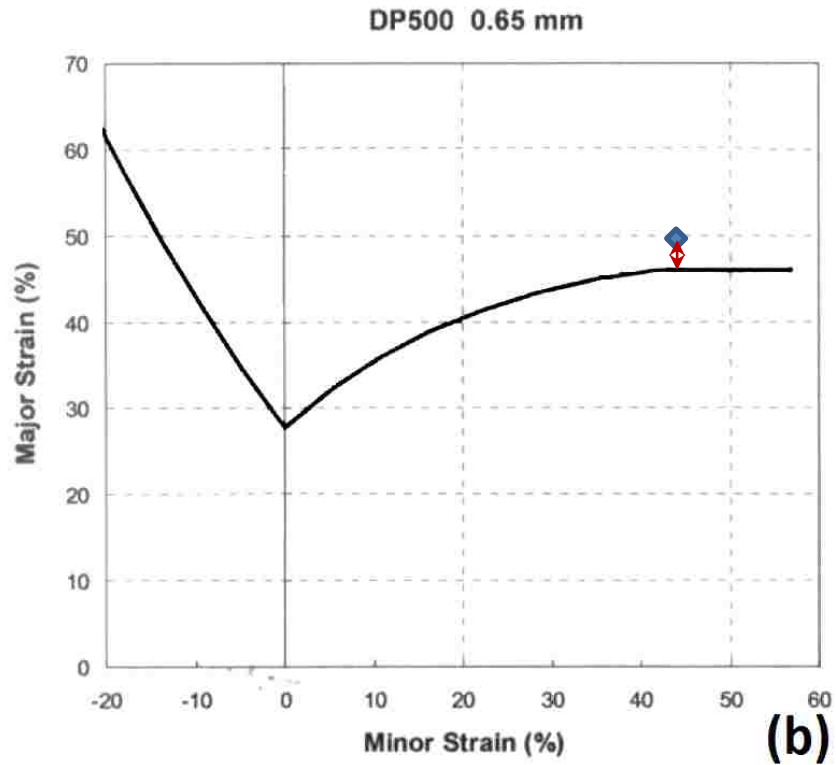
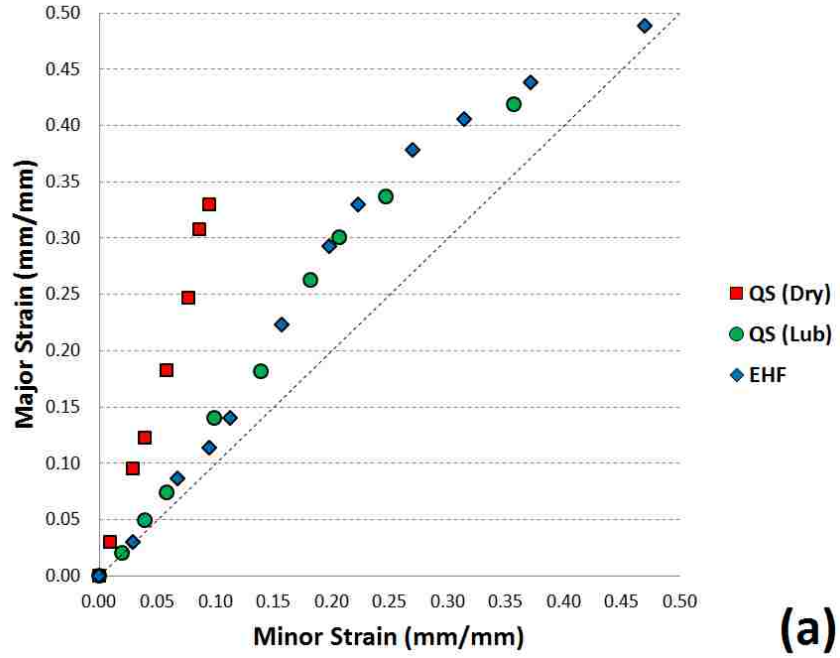
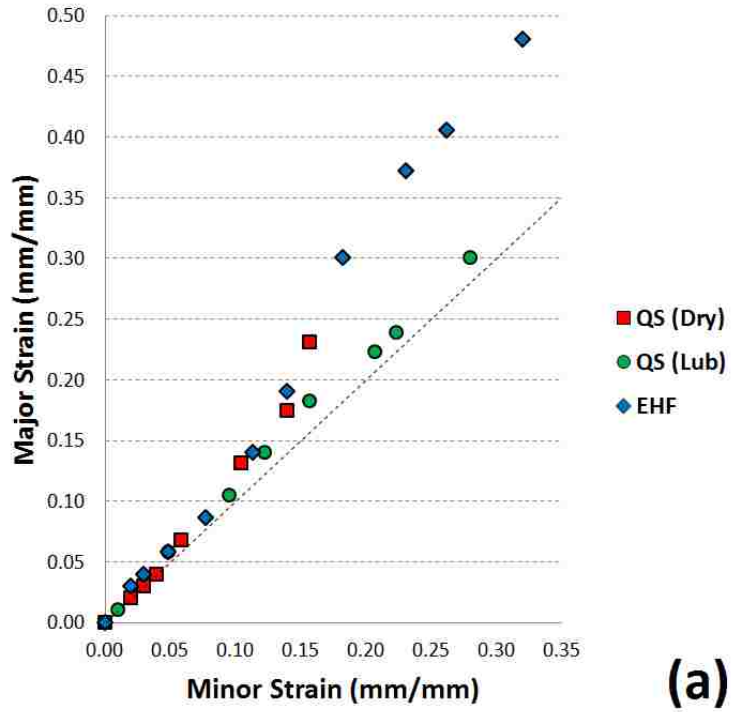
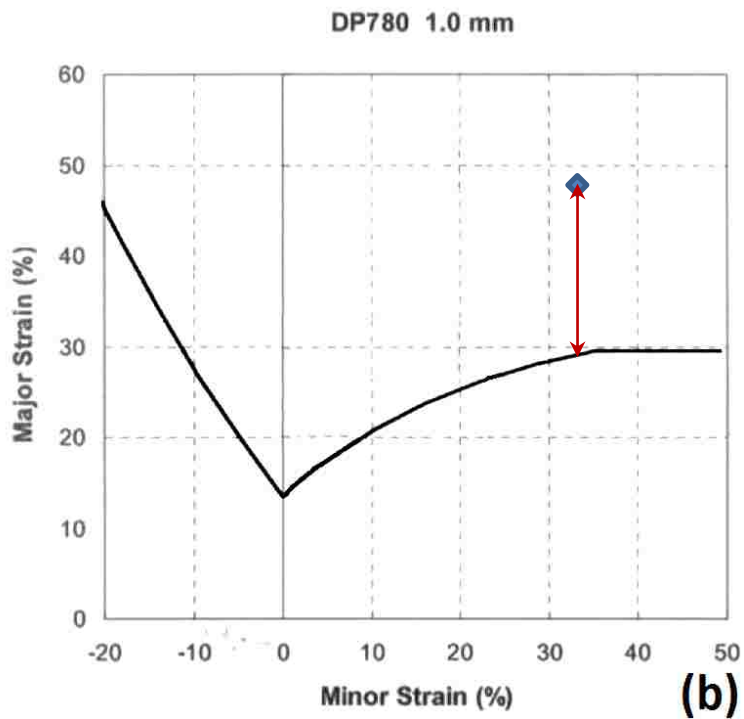


Figure 6-1 (a) True major vs. minor strain across the DP500 specimens, and (b) quasi-static forming limit diagram of the DP500 including the greatest safe engineering strain in DP500 formed under EHF using a conical die. The quasi-static FLD is reported by Golovashchenko et al. [236]



(a)



(b)

Figure 6-2 (a) True major vs. minor strain across the DP780 specimens, and (b) quasi-static forming limit diagram of the DP780 including the greatest safe engineering strain in DP780 formed under EHF using a conical die. The quasi-static FLD is reported by Golovashchenko et al. [236]

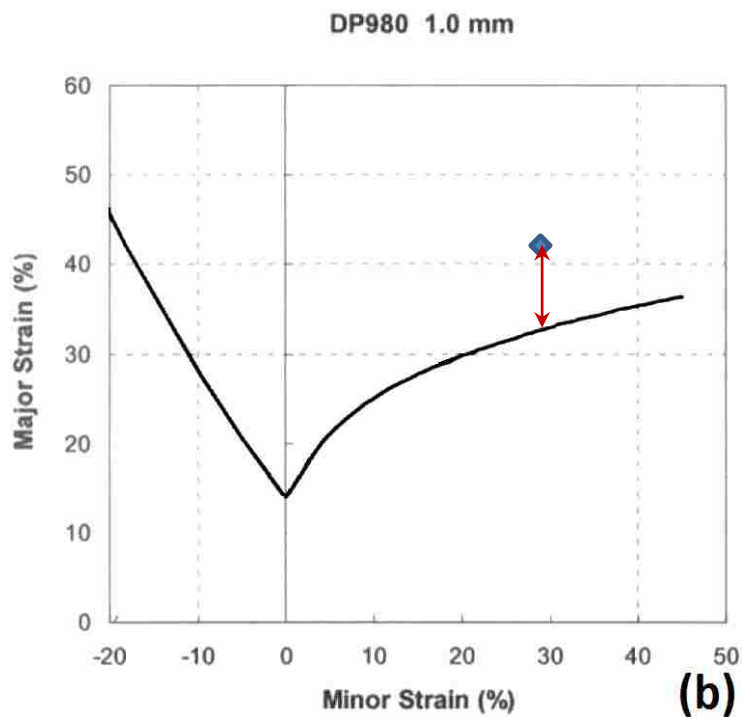
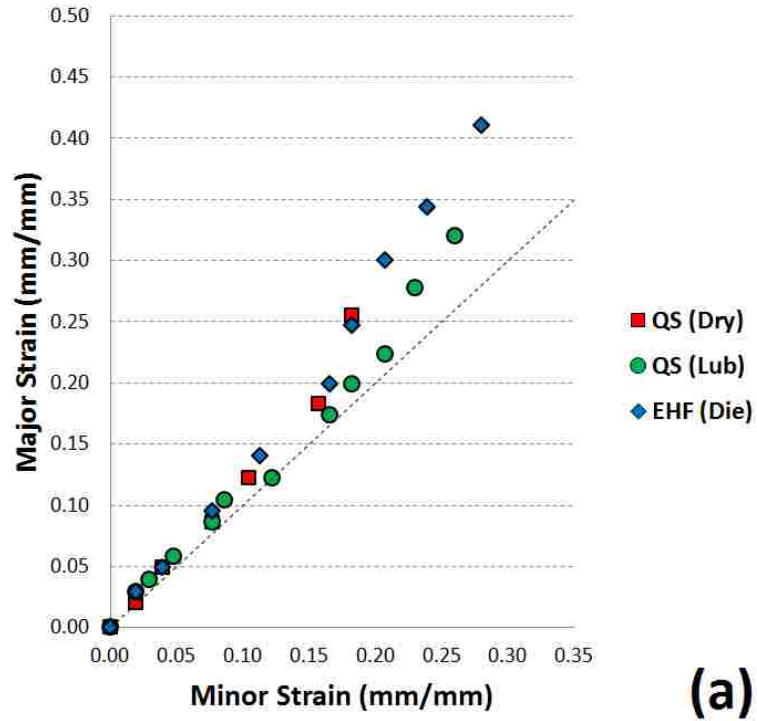


Figure 6-3(a) True major vs. minor strain across the DP980 specimens, and (b) quasi-static forming limit diagram of the DP980 including the greatest safe engineering strain in DP980 formed under EHF using a conical die. The quasi-static FLD is reported by Golovashchenko et al. [236]

6.2 Micro-scale Characterization of Hyperplasticity

Microstructural analysis of hyperplasticity is necessary in order to understand the role of each constituent in the formability improvement. In dual phase steels, ferrite is known as the soft and ductile phase. On the other hand, martensite is the hard phase with very limited ductility.

Under quasi-static conditions, the plastic deformation of martensite has been investigated by different techniques such as the analysis of work hardening curves [75], in-situ scanning electron microscope images [106], and microgridding [107]. The overall result indicated that under quasi-static forming conditions, untempered martensite generally behaves elastically up to high levels of deformation such as necking or even beyond. The question is whether martensite shows the same behaviour under EHF. The contribution of martensite to the enhanced plastic deformation of the EHF specimens can be investigated by quantitative study of micro-strain in the ferrite grains and martensite islands at different macro-strain levels from the edge to the centre of the specimens.

6.2.1 Micro-strain in Ferrite and Martensite

Optical measurements [237], high speed camera [238], and the digital image correlation (DIC) technique [38] were previously used by other researchers to study strain localization during high strain rate forming. In this chapter, the strain distribution in ferrite grains and martensite islands was determined by means of statistical quantitative metallography. To enhance the accuracy of the results, the sizes of more than 7,000 ferrite grains and 10,500 martensite islands were measured at different strain levels. Because of the continuous martensite network in DP980, it was not possible to measure the size of martensite islands in DP980. Hence, quantitative metallography was carried out only in DP500 and DP780 specimens.

Table 6-1 is the summary of the statistical analysis of the measured data in terms of the size of ferrite grains and martensite islands in the as-rolled and deformed DP500 and

DP780 specimens. As can be seen in all of the cases the **RA%** is below 10% which shows the acceptable accuracy of the data according to ASTM E1382-97 [231]. The “Point” numbers in Table 6-1 correspond with the “Point” numbers displayed in Figure 3-3. “Point 1” is the location where the greatest level of safe strains could be measured, i.e. the materials showed no evidence of damage at the macroscopic scale and the microscopic damage (micro-voids and micro-cracks) was negligible. “Point 4” was not considered for the specimens formed under quasi-static conditions since the strain induced in this area was very low. The values presented in Table 6-1 as the mean sizes were applied as $d_{as-rolled}$ and d_f in (3-5). By using (3-6 and (3-7, true major and minor strains in the martensite islands and ferrite grains were calculated from the edge to the centre of the specimens throughout the safe zone. The obtained micro-strains are presented in Figure 6-4. Figure 6-4-a shows that the martensite strain values in EHF were significantly higher than in quasi-static forming. This demonstrates that high strain rate forming processes can lead to a significant improvement in ductility of martensite. The enhanced deformation of ferrite is also displayed in Figure 6-4-b. To have a better understanding of the relative deformation improvement under EHF, Figure 6-5-a shows the greatest major vs. minor micro-strains of the constituents. As it is shown in Figure 6-5-b, based on the von Mises effective strain, relative deformation improvements of approximately 20% and 100% were determined in the ferrite and the martensite, respectively.

As can be seen in Figure 6-5-b, the relative deformation improvement of:

- the martensite was much greater than that of ferrite,
- the martensite in DP500 was greater than that of the martensite in DP780, and
- the ferrite in DP780 was practically identical to that of ferrite in DP500.

In Section 6.1, it was observed that the macro-scale relative formability improvement of the harder materials, i.e. DP780 and DP980 was greater than that of the softer materials, i.e. DP500. This observation seems to be verified at the micro-scale too.

Table 6-1 Ferrite grain and martensite island sizes in DP500 and DP780 steels after deformation

			Ferrite grain size (μm)				Martensite island size (μm)			
			DP500		DP780		DP500		DP780	
Point	Direction	Statistics	QS	EHF	QS	EHF	QS	EHF	QS	EHF
1	Minor	Mean	10.15	10.47	9.77	9.65	1.83	1.90	2.39	2.46
		Count	193	191	195	198	494	453	225	246
		Std. Dev.	4.82	4.29	4.23	4.18	0.81	0.88	1.15	1.25
		%RA	6.7	5.8	6.1	6.0	3.9	4.3	6.3	6.4
	Thickness	Mean	3.40	3.13	3.62	3.35	1.50	1.37	1.65	1.49
		Count	287	302	240	235	468	535	220	237
		Std. Dev.	1.79	1.87	1.76	1.81	0.72	0.66	0.88	0.79
		%RA	6.1	6.7	6.2	6.9	4.4	4.1	7.1	6.8
2	Minor	Mean	9.67	9.99	9.25	9.40	1.81	1.87	2.35	2.42
		Count	218	209	192	178	395	512	232	245
		Std. Dev.	3.95	3.87	4.28	4.37	0.82	0.74	1.07	1.18
		%RA	5.4	5.3	6.5	6.8	4.5	3.4	5.9	6.1
	Thickness	Mean	3.89	3.56	4.02	3.64	1.55	1.43	1.70	1.56
		Count	215	265	214	195	395	463	245	215
		Std. Dev.	1.88	1.98	2.05	1.77	0.72	0.69	0.94	0.81
		%RA	6.5	6.7	6.8	6.8	4.6	4.4	6.9	6.9
3	Minor	Mean	9.20	9.60	8.84	9.10	1.79	1.87	2.31	2.37
		Count	225	215	192	205	382	480	218	236
		Std. Dev.	4.08	4.53	4.16	4.26	0.88	0.78	1.09	1.03
		%RA	5.8	6.3	6.7	6.4	4.9	3.7	6.3	5.5
	Thickness	Mean	4.33	3.96	4.42	4.01	1.59	1.43	1.76	1.65
		Count	242	252	215	235	345	320	234	223
		Std. Dev.	1.92	1.95	2.02	1.98	0.74	0.68	0.91	0.87
		%RA	5.6	6.1	6.1	6.3	4.9	5.2	6.6	6.9
4	Minor	Mean	-	9.21	-	8.76	-	1.81	-	2.32
		Count	-	215		220	-	372	-	228
		Std. Dev.	-	4.18		3.91	-	0.79	-	1.17
		%RA	-	6.1	-	5.9	-	4.4	-	6.5
	Thickness	Mean	-	4.37	-	4.49	-	1.55	-	1.74
		Count	-	245		226	-	354	-	251
		Std. Dev.	-	2.05		2.14	-	0.69	-	0.79
		%RA	-	5.9	-	6.2	-	4.6	-	5.6
As-rolled	Minor	Mean	8.33		7.83		1.77		2.26	
		Count	208		215		408		215	
		Std. Dev.	3.75		3.68		0.88		1.09	
		%RA	6.1		6.3		4.8		6.4	
	Thickness	Mean	5.45		5.69		1.63		1.84	
		Count	265		258		382		215	
		Std. Dev.	2.03		2.16		0.78		0.89	
		%RA	4.5		4.6		4.8		6.5	

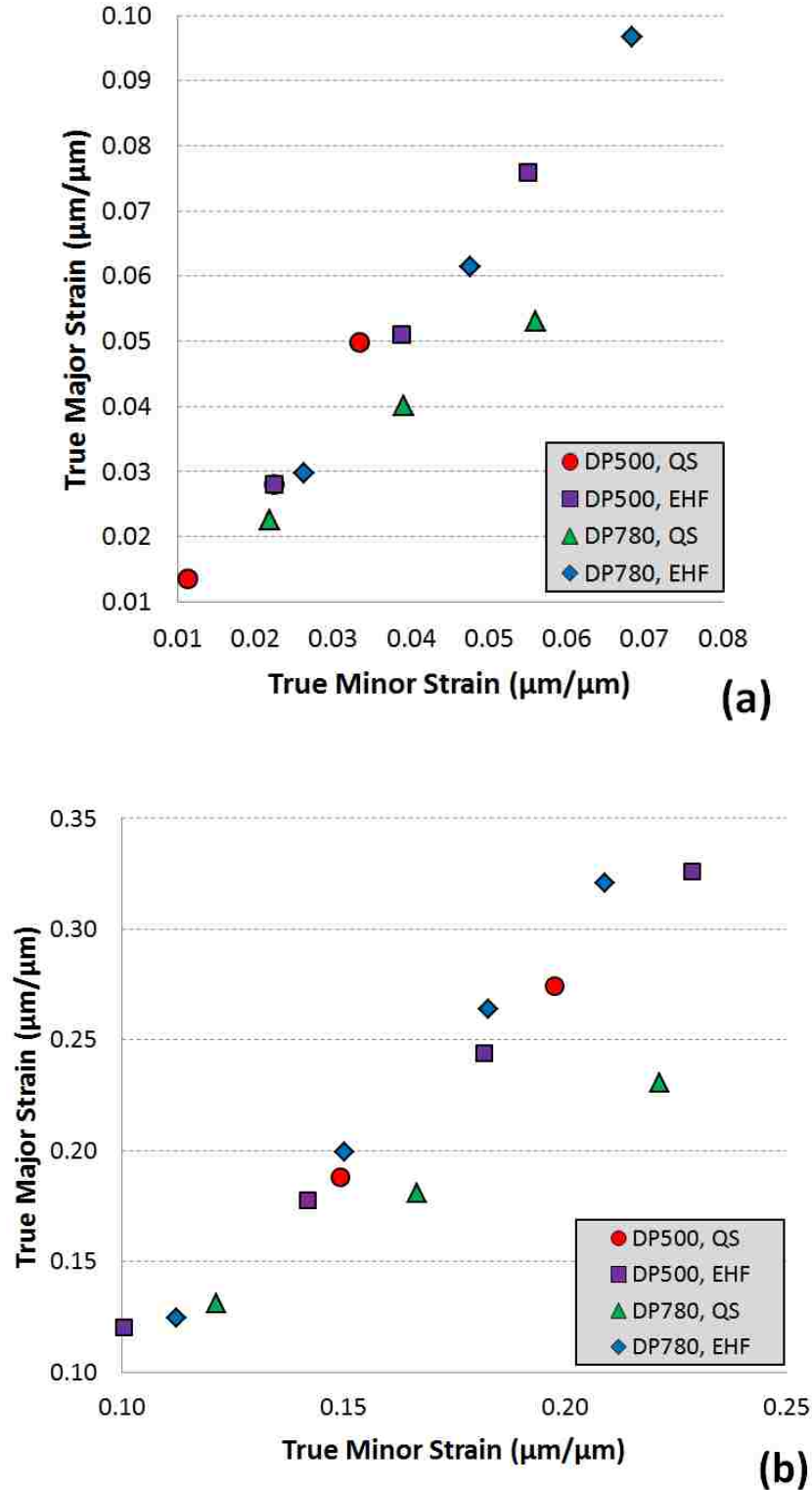
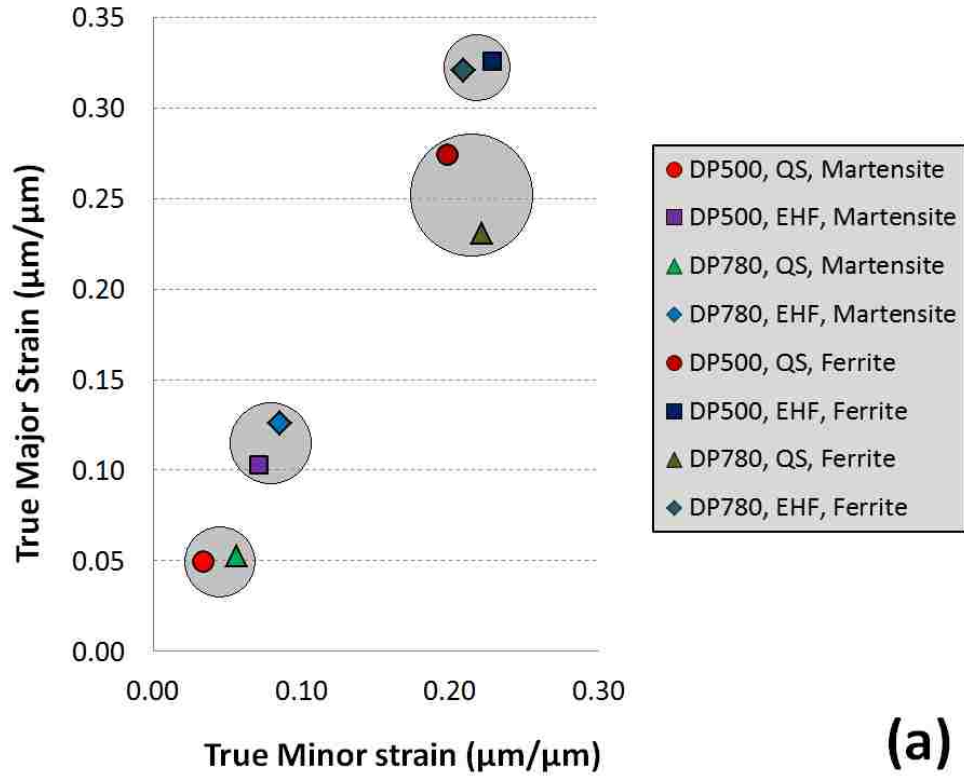
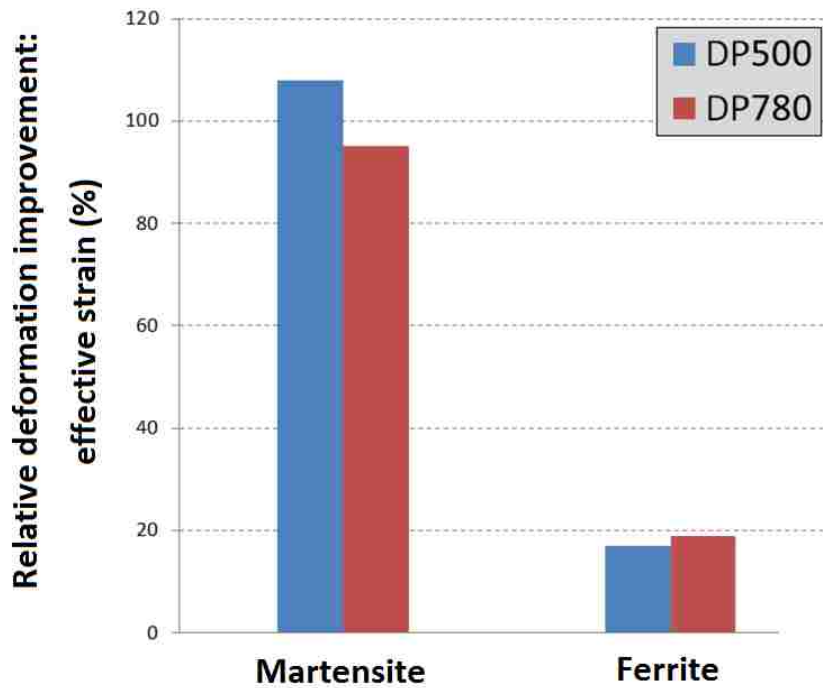


Figure 6-4 True major vs. minor micro-strains in (a) martensite islands, and (b) ferrite grains; from the edge to the centre of the specimens formed under quasi-static and high strain rate conditions. Note that the volume fraction of martensite in DP500 and DP780 was 10% and 23%, respectively.



(a)



(b)

Figure 6-5 (a) The greatest true major vs. minor micro-strains of the constituents in the safe zone of the specimens, and (b) relative deformation improvement of the constituents under EHF.

6.2.2 Correlation of Macro-strain and Micro-strains

The mixture rule was considered to investigate the correlation between the macro and micro-strains. The total major and minor micro-strains were calculated by substituting the ferrite and martensite strains and volume fractions into the mixture rule as follows:

$$\epsilon_{Micro} = \epsilon_F \times V_F + \epsilon_M \times V_M \quad (6-1)$$

where ϵ_{Micro} is the microstructure strain, ϵ_F and ϵ_M are the ferrite and martensite strains, respectively, and V_F and V_M are the ferrite and martensite volume fractions, respectively. The resulting macro- and micro-strains are shown in Figure 6-6. The error for the macro-strains was considered to be 0.005 which is the error of the FMTI strain measurement system, and the error for micro-strains was considered to be 7.0% which is approximately the greatest **%RA** presented in Table 6-1. As it can be seen in all the discussed cases, the mixture rule successfully correlated the micro-mechanical strains to the macro-scale strains both under quasi-static and high strain rate forming conditions; however, according to the trendlines, the micro-strains lie slightly below the macro-strains in all cases. Moreover, the deviation between the macro and micro-strain gradually increases with increasing strain. Finally, greater deviation between macro and micro-strains was observed in DP780 compared to DP500.

During the quantitative metallography, it was possible to measure the martensite island mean size throughout the sheet except in the martensite band. Therefore, by considering the strain measured in the martensite islands as the total martensite strain, the influence of the strain in the martensite band was not taken into account. Moreover, it appeared that the deformation of the martensite band was greater than that of the martensite islands due to the fact that martensite islands were surrounded with the softer ferrite which accommodates large strains during plastic deformation. However, since in the vicinity of the martensite band, the amount of the ferrite was lower, a greater proportion of the strain was induced into the martensite band. Figure 6-7 shows several nano-scale voids that nucleated within the martensite band due to the high level

of plastic deformation while the martensite islands remained relatively free of voids. The greater possibility of plastic deformation in martensite band compared to the martensite islands were also reported by Mazinani et al. [108].

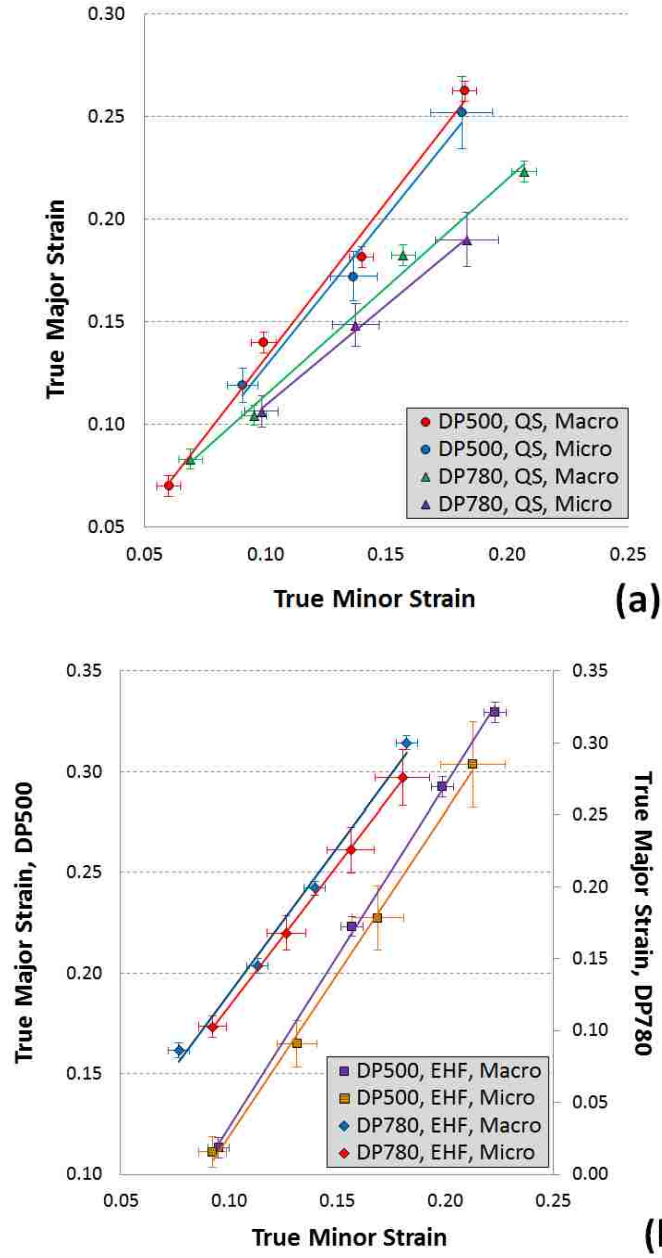


Figure 6-6 True macro and micro minor vs. major strains in DP500 and DP780 under (a) quasi-static and (b) EHF conditions.

It would seem that the difficulty to measure the strain in the continuous martensite band is a source of error in the determination of the martensite strains. This explanation is further supported by comparing the discrepancy between the macro and micro-strains in the specimens in Figure 6-6. It can be seen that the deviations between the trendlines for the quasi-static and high strain rate conditions were greater in the DP780 than in DP500, since the martensite band was larger in the DP780 steel.

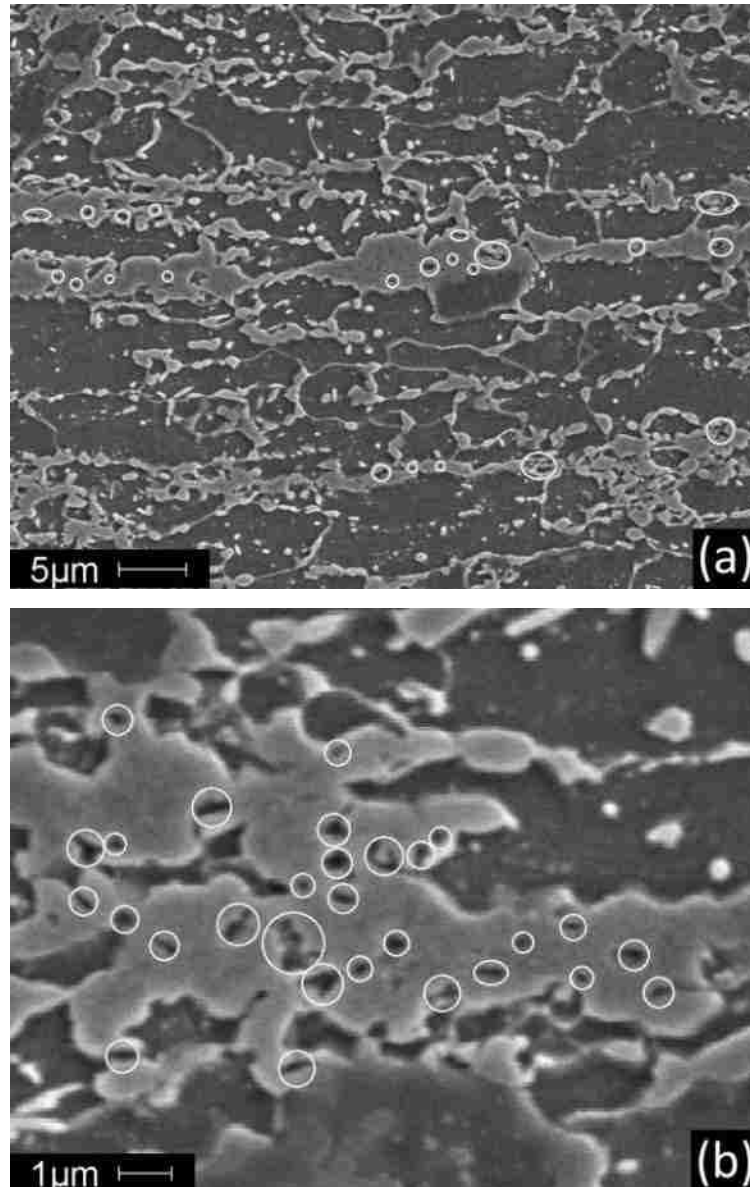


Figure 6-7 DP780 steel formed under EHF (a) safe martensite islands in the vicinity of the martensite band and (b) nano-scale voids in the martensite band.

6.3 Nano-scale Characterization of Hyperplasticity

In this section, the role of dislocations and deformation twinning, as the principal mechanisms of plastic deformation in BCC metals and alloys, in hyperplasticity of dual phase steels are discussed. Furthermore, there is a brief investigation on the bend contours which were observed in most of the TEM images.

6.3.1 Bending Contours in TEM Images

Bend contours appear in the bright field TEM images of buckled or bent samples. The mechanism that causes the bend contours to appear was explained by Fultz and Howe [239] in detail. As described before, dome-shaped and conical specimens were investigated in this research. "Consider a more general case when the sample is buckled around two axes, and is formed into the shape of a dome or a dish. In this case, the bright field image shows crossed sets of bend contours from the different sets of twisted Bragg planes." [239]. As an example, bend contours of a buckled specimen are shown in Figure 6-8 . As can be seen in Figure 6-9, Figure 6-10, and Figure 6-11, bend contours were found throughout the samples during TEM observations. It is important that the bend contours are not mistaken for dislocations or dislocation cells in the TEM images.

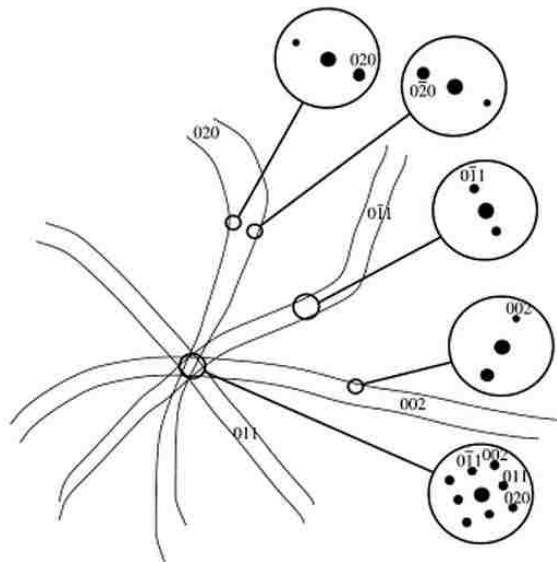


Figure 6-8 Bright field image of a bend contour in a buckled specimen [239]

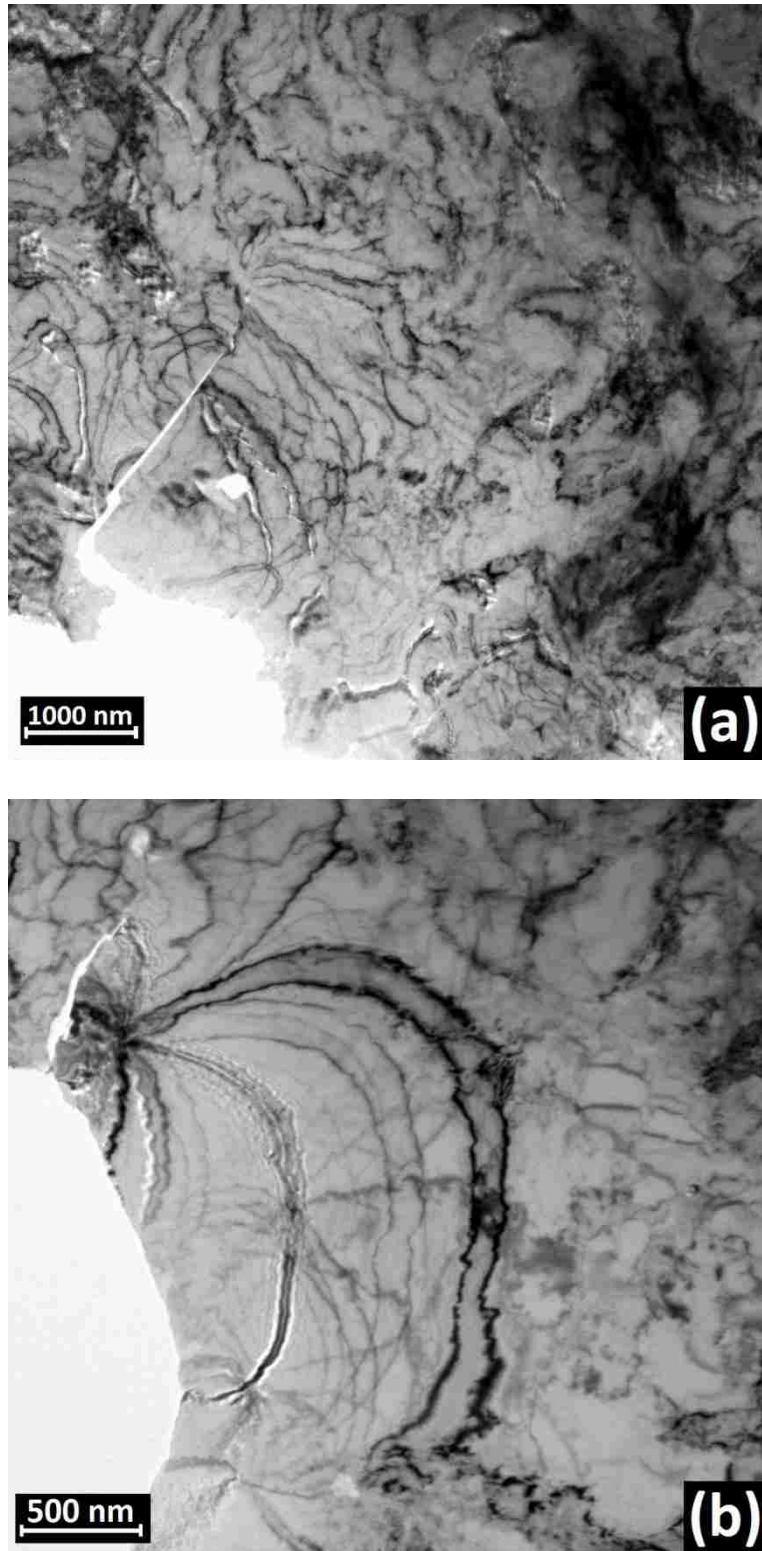


Figure 6-9 Bend contours in DP500 formed in the (a) Nakazima test, and (b) in EHF.

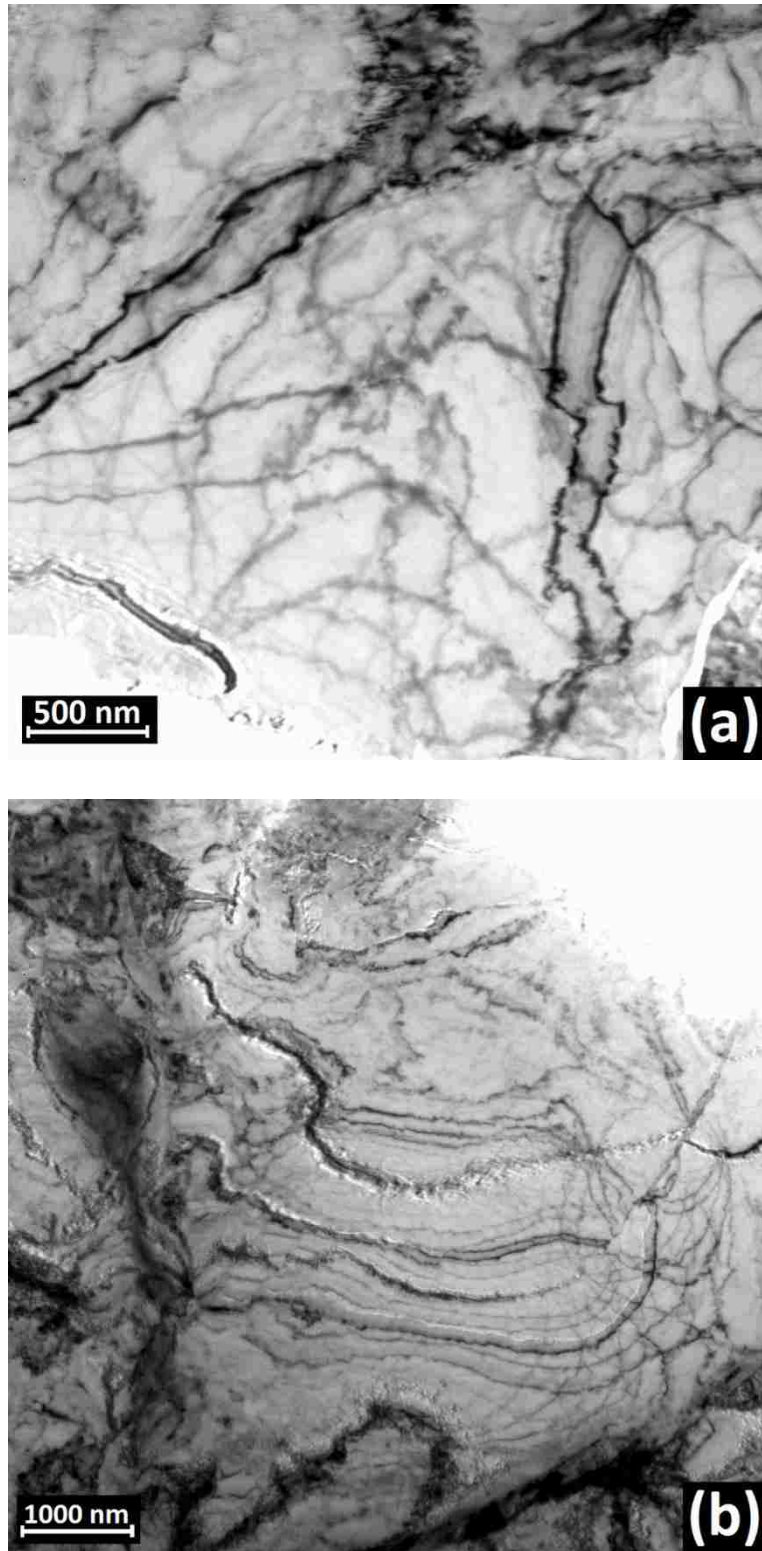


Figure 6-10 Bend contours in DP780 formed in the (a) Nakazima test, and (b) in EHF.

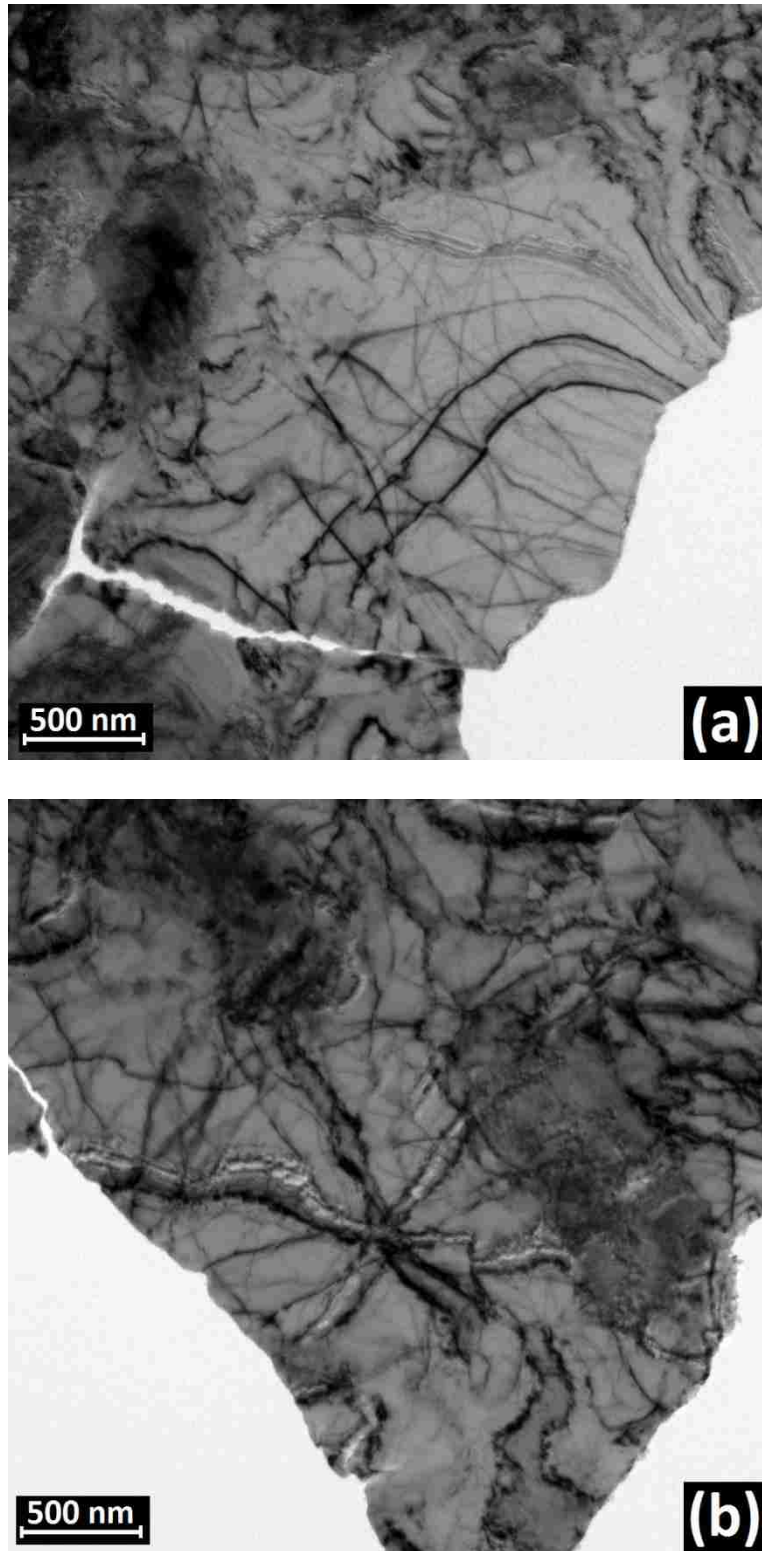


Figure 6-11 Bend contours in DP980 formed in the (a) Nakazima test, and (b) in EHF.

6.3.2 Dislocations under Nakazima test and EHF

The strain rate differs greatly between the Nakazima test and EHF. While the deformation in the Nakazima test was quasi-static, specimens were formed under high strain rates in EHF. As a result, there was sufficient time for dislocations in the Nakazima specimens, to form configurations with lower energies, such as cell structures. However, after forming of the Nakazima specimens, the dislocation density was not sufficient to form dislocation cells with distinguishable walls throughout the ferrite grains. However, as shown in Figure 6-12-a, since a martensite island is an obstacle for mobile dislocations, the accumulation of dislocations near the ferrite/martensite interface increased the dislocation density in this area. As a result, as can be seen in Figure 6-12-b for DP780 formed in the Nakazima test, the dislocation density was substantial in the vicinity of the interface to form some dislocation cells.

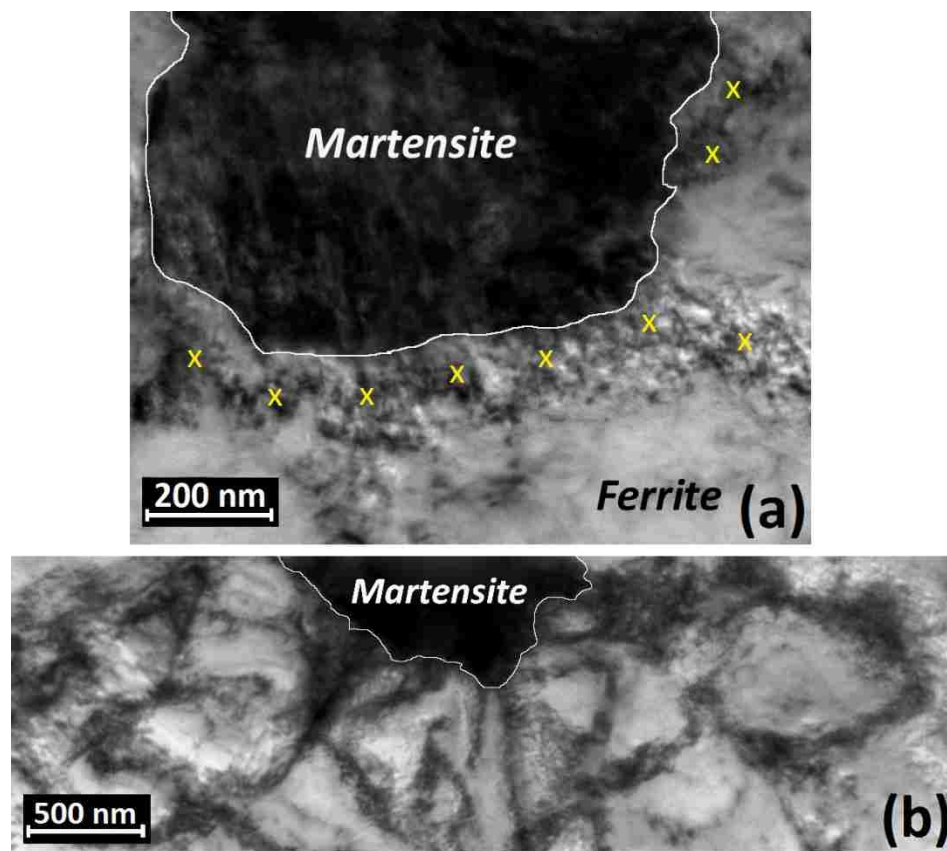


Figure 6-12 DP780 Nakazima specimen: (a) accumulation of dislocations shown by “X” at the ferrite/martensite interface, and (b) dislocation cells in the vicinity of ferrite/martensite interface.

As previously mentioned in Section 6.2.1, quantitative metallography of ferrite grains showed an approximate improvement of 20% in the deformation of ferrite grains under EHF. Although deformation twinning is a major mechanism of deformation in BCC materials formed at high strain rate [240-242], selected area diffraction (SAD) patterns did not show deformation twinning as a principal mechanism of improvement of deformation in the ferrite. Therefore, the mechanism responsible for this formability improvement under EHF should be attributed to dislocations.

As explained in Section 2.4, the motion of dislocations in BCC materials is a function of strain rate. For a mild steel, long range obstacles, short range obstacles, and thermal phonons were mentioned as the main barriers to the motion of dislocation under quasi-static conditions, moderate and high strain rates (below 5000 s^{-1}), and ultrahigh strain rates (above 5000 s^{-1}), respectively. Since the lattice structure of the ferrite and the low carbon martensite phases in the dual phase steels studied in this research are BCC, it is expected that the above descriptions are true for these constituents. Hence, it is important to know the level of strain rate in EHF. As can be seen in Figure 6-13, as was reported by the industrial partner of the current project [236], the strain rate in EHF of a DP590 specimen using a 34° conical die was over $5 \times 10^3 \text{ s}^{-1}$ and could even reach $20 \times 10^3 \text{ s}^{-1}$. It is reasonable to assume, therefore, that the level of strain rate in the DP500, DP780, and DP980 specimens formed under the same EHF condition into the 34° conical die should be in the same order of magnitude.

It is expected that long range obstacles control the motion of dislocations in the ferrite and martensite when the sheet is deformed in the Nakazima test, and thermal phonons and conduction electrons control the motion of dislocations in EHF. In the following, the behaviour of dislocations which resulted in hyperplasticity in EHF is discussed in three sections: nucleation, motion, and multiplication of dislocations.

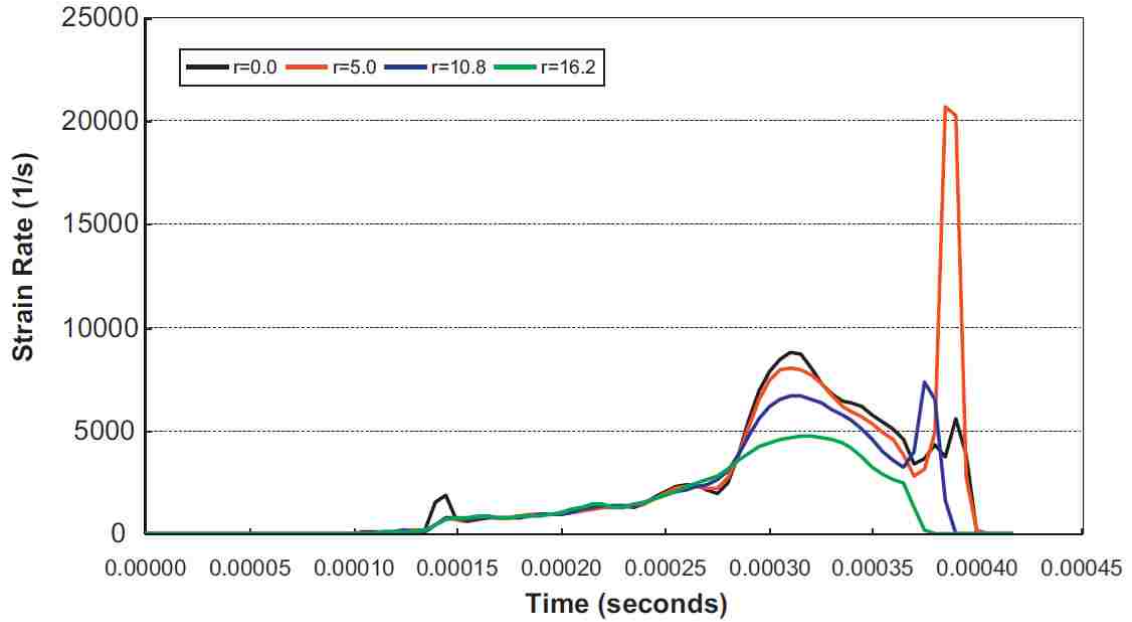


Figure 6-13 Evolution of strain rate across a DP590 specimen formed under EHF using the 34° conical die. r is the Radial distance from the symmetry axis in mm [236].

Nucleation of Dislocations As mentioned in Section 2.4, at high strain rates, when the maximum dislocation velocity is surpassed, plastic deformation is not achieved merely by the movement and multiplication of existing dislocations. A significant number of dislocations are nucleated which result in a rapid increase of dislocation density and a remarkable enhancement of strength. As a mechanism of hyperplasticity, the extensive nucleation of dislocations under EHF is further investigated in Section 6.5.

Multiplication of Dislocations Figure 6-14 shows multiplication of dislocations which were more frequently observed in the EHF specimens. The existence of bend contours made it difficult to distinguish these from dislocation loops. Dislocation loops can be generated by dislocation sources such as Frank-Read sources [243] or by the double-cross slip mechanism that was suggested by Koehler [244] and Orowan [245]. The more frequent multiplication of dislocations may be one reason for hyperplasticity in EHF. The ability to multiply dislocations is greater in EHF compared to quasi-static forming due to the significantly greater shear stresses that are generated by the shock wave, which in turn are able to activate the dislocation sources.

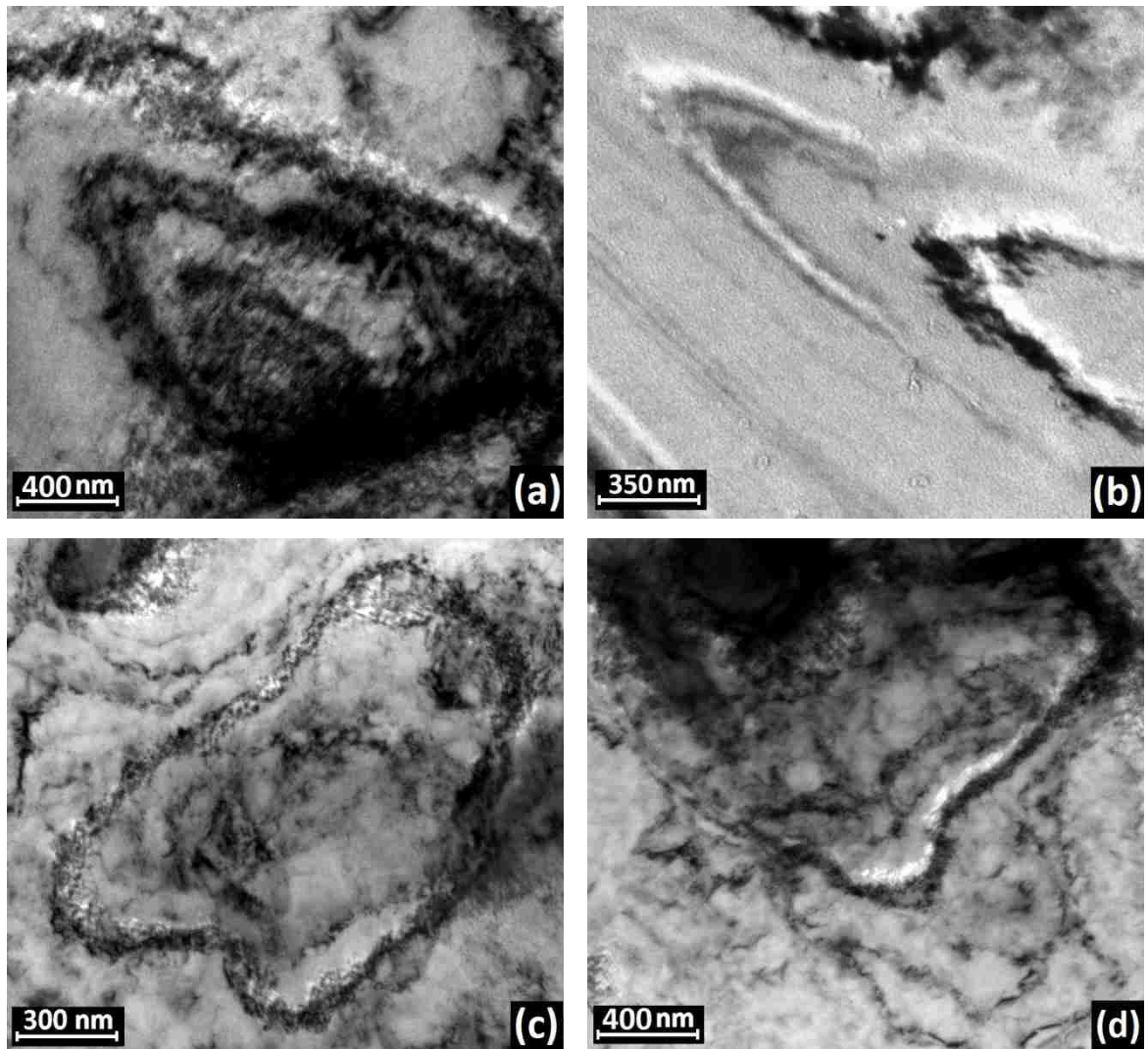


Figure 6-14 Dislocation multiplication inside a ferrite grain in (a) and (b) DP500, and (c) and (d) DP780, formed in EHF process.

6.3.3 Deformation Twinning under Nakazima test and EHF

According to several researchers [240-242], under shock loading such as EHF, deformation twinning effectively participates in the plastic deformation, particularly in bcc materials. The activation energy for deformation twinning is greater than that for slip at low and intermediate stress levels; however, at high stress levels prevalent during high strain rate forming, deformation twinning is more likely to occur. Selected area diffraction (SAD) patterns displayed deformation twinning in the ferrite grains deformed

by EHF; however, due to the limited amount of twinning that was observed, it could not be considered the primary mechanism of hyperplasticity in ferrite.

As mentioned in Section 6.2.1, a relative deformation improvement of approximately 100% was determined in the martensite islands when deformed by EHF. This significant enhancement could not be achieved merely by the motion of dislocations, but as it can be seen in Figure 6-15, deformation twins were widely found in the martensite islands in specimens deformed by EHF. The large amount of deformation twinning which was observed in almost all the TEM images of martensite islands is perhaps the main reason for the remarkable hyperplasticity in the martensite. Hyperplasticity in the martensite also enhances the plastic compatibility between the ferrite and the martensite which further contributes to the hyperplasticity of dual phase steels. This phenomenon is quantitatively discussed in Section 6.4.

The extensive formation of deformation twins in the martensite during EHF contributes toward the significant formability improvement that is observed in dual phase steels. According to Sevillano [246], where deformation twinning is a dominant micro-mechanism of deformation, “geometrically necessary twins” can assist with the accommodation of plastic strain gradients. Deformation twinning in the martensite might be geometrically necessary to accommodate the strain gradient at the ferrite/martensite interface. This helps to minimize decohesion and the nucleation of voids which in turn results in a formability improvement.

The ductility of martensite in DP980 was greater than that of DP500 and DP780 due to the lower carbon content in the martensite in DP980. Hence, extensive formation of twins in the softer martensite in DP980 changed the initial morphology of the martensite in the EHF specimens. As can be seen in Figure 6-16, the deformation of the martensite in a DP980 EHF specimen (Figure 6-16-a) is significant compared to that of the martensite in a DP980 Nakazima specimen (Figure 6-16-b), or even compared to that of the martensite in DP500 and DP780 EHF specimens (Figure 6-16-c and 6-d). In case of EHF specimens, the superior level of deformation in the martensite in DP980 may be

due to the more extensive formation of deformation twins compared to the martensite in DP500 and DP780.

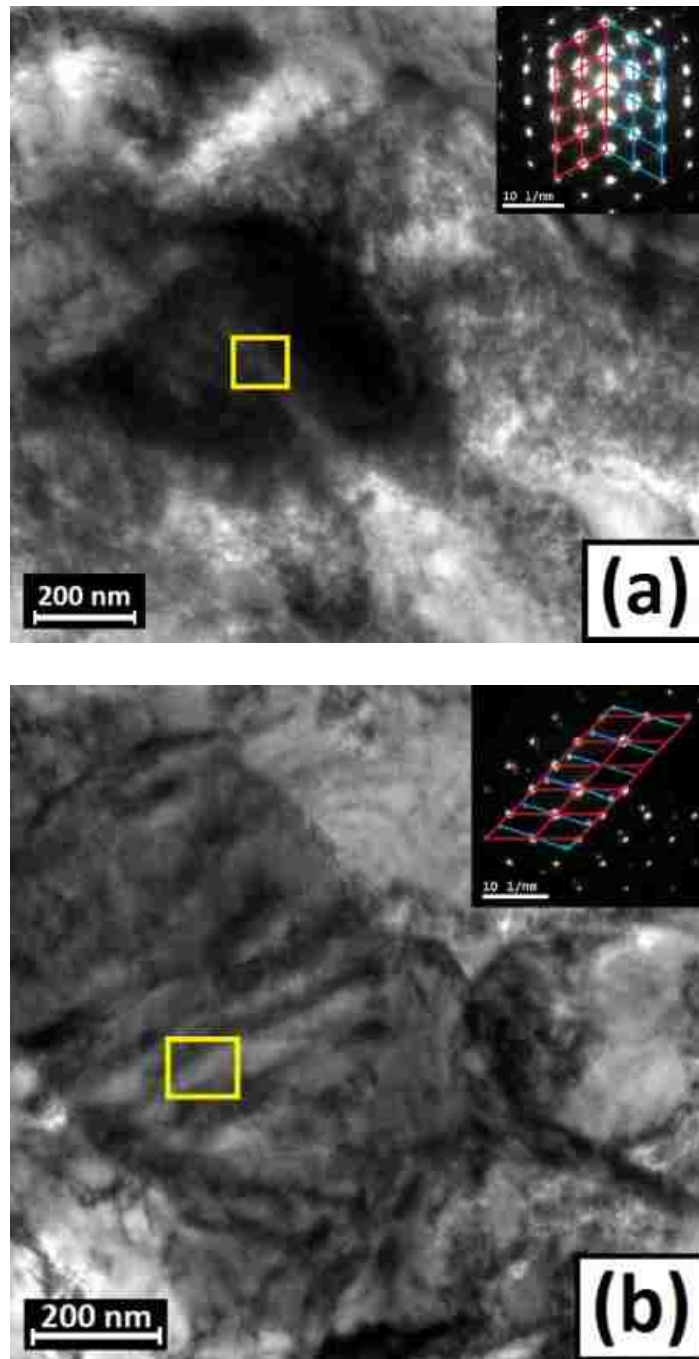


Figure 6-15 Deformation twinning in martensite deformed by EHF in (a) DP780, and (b) DP980. The SAD is shown by the yellow box.

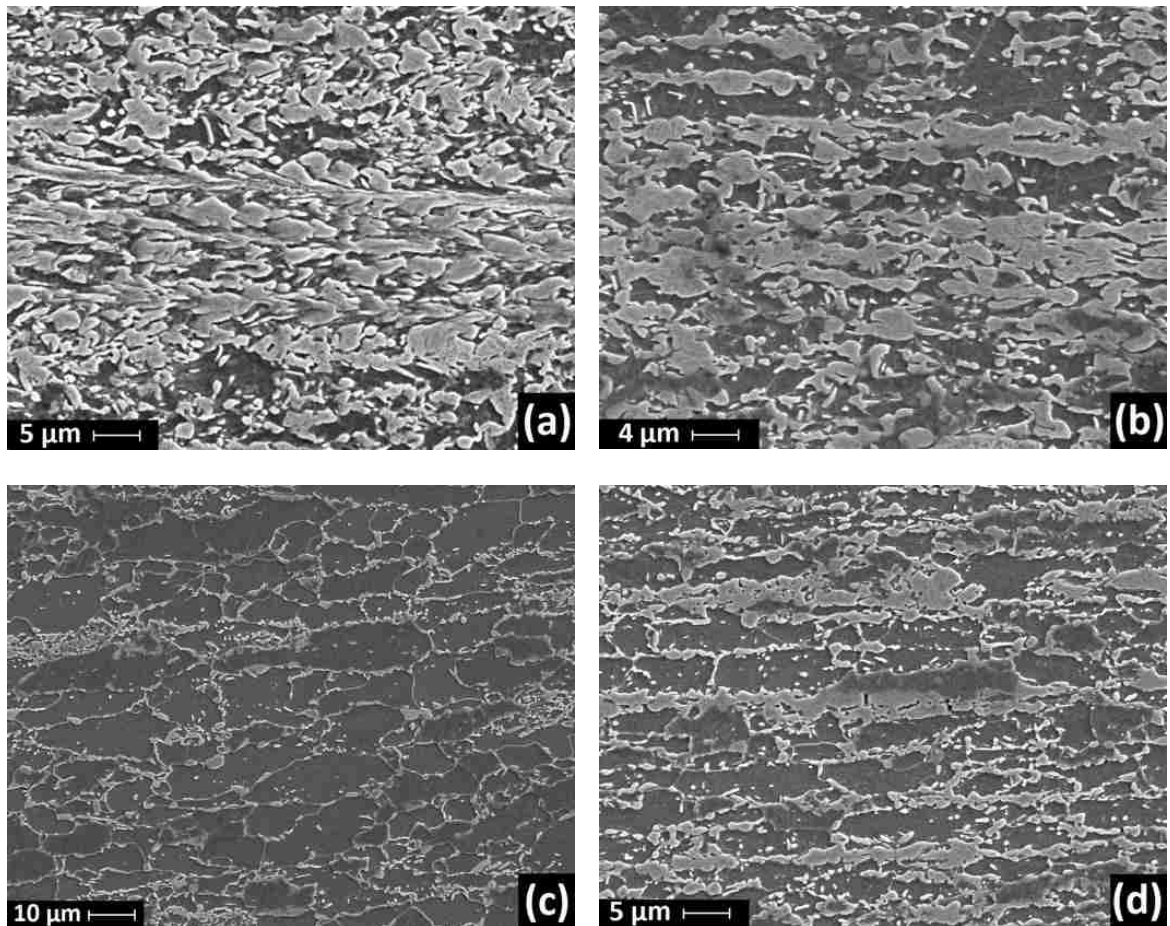


Figure 6-16 Plastic deformation in specimens at approximately 0.30 strain: (a) DP980-EHF, (b) DP980-Nakazima, (c) DP500-EHF, and (d) DP780-EHF.

6.4 Enhanced Plastic Compatibility between Ferrite and Martensite in EHF

One mechanism of hyperplasticity in dual phase steels can be attributed to the enhanced plastic compatibility between the constituent phases which is evidenced by a more homogenized deformation and suppression of decohesion and failure at the ferrite/martensite interface.

In order to investigate the plastic compatibility between ferrite and martensite, the data obtained from quantitative metallography of DP500 and DP780 steels was used to calculate the martensite to ferrite (major and minor) strain ratio (ϵ_M/ϵ_F) at different

strain levels. A strain ratio equal to 1 would mean there is perfect plastic compatibility between the phases.

Under quasi-static forming conditions, the ϵ_M/ϵ_F strain ratio was close to zero because of the limited elongation of the martensite; however due to the significant improvement of relative deformation of the martensite in EHF, the ϵ_M/ϵ_F ratio improved significantly in DP500 and DP780 when subject to EHF. The result of this quantitative investigation on the ϵ_M/ϵ_F ratio is shown in Figure 6-17. As can be seen, the plastic compatibility between the hard martensite and soft ferrite was remarkably enhanced under EHF and the strain gradient across the ferrite/martensite interface is reduced. Consequently, the risk of decohesion at the ferrite/martensite interface is also reduced.

It can also be seen in Figure 6-17 that the ϵ_M/ϵ_F ratio is greater for DP780 compared to DP500; this can be explained by the lower carbon content of the martensite and stronger solid solution hardening of ferrite in DP780 which help to reduce the difference in flow stress and elongation of the constituents.

Furthermore, it can be seen in Figure 6-17 that the ϵ_M/ϵ_F ratio increases with strain, i.e. from the edge to the apex of the specimens. Near the edge of a specimen, the local stress level was not sufficient to induce significant plastic deformation in the martensite, and therefore ϵ_M/ϵ_F remained small. However, the local stress level was greater toward the apex of the specimen, and therefore the martensite elongation was enhanced and the ϵ_M/ϵ_F ratio increased.

On the other hand, as was shown in Figure 6-13, during EHF of sheet specimens into the 34° conical die, the strain rate also increases toward the apex of the die. At the outer edge of the specimen, the deformation is solely carried out by the shock-wave and the strain rate is within the range $5\text{-}20\times 10^3\text{ s}^{-1}$. However, as the sheet material approaches the apex of the cone, the velocity at which the sheet impacts the die surface increases significantly and “inertial ironing” occurs more effectively. Consequently, the strain rate can exceed $20\times 10^3\text{ s}^{-1}$ near the top of the conical specimen. It appears that die impact and greater strain rates are also responsible for enhancing the plastic compatibility between the ferrite and martensite at higher strain levels.

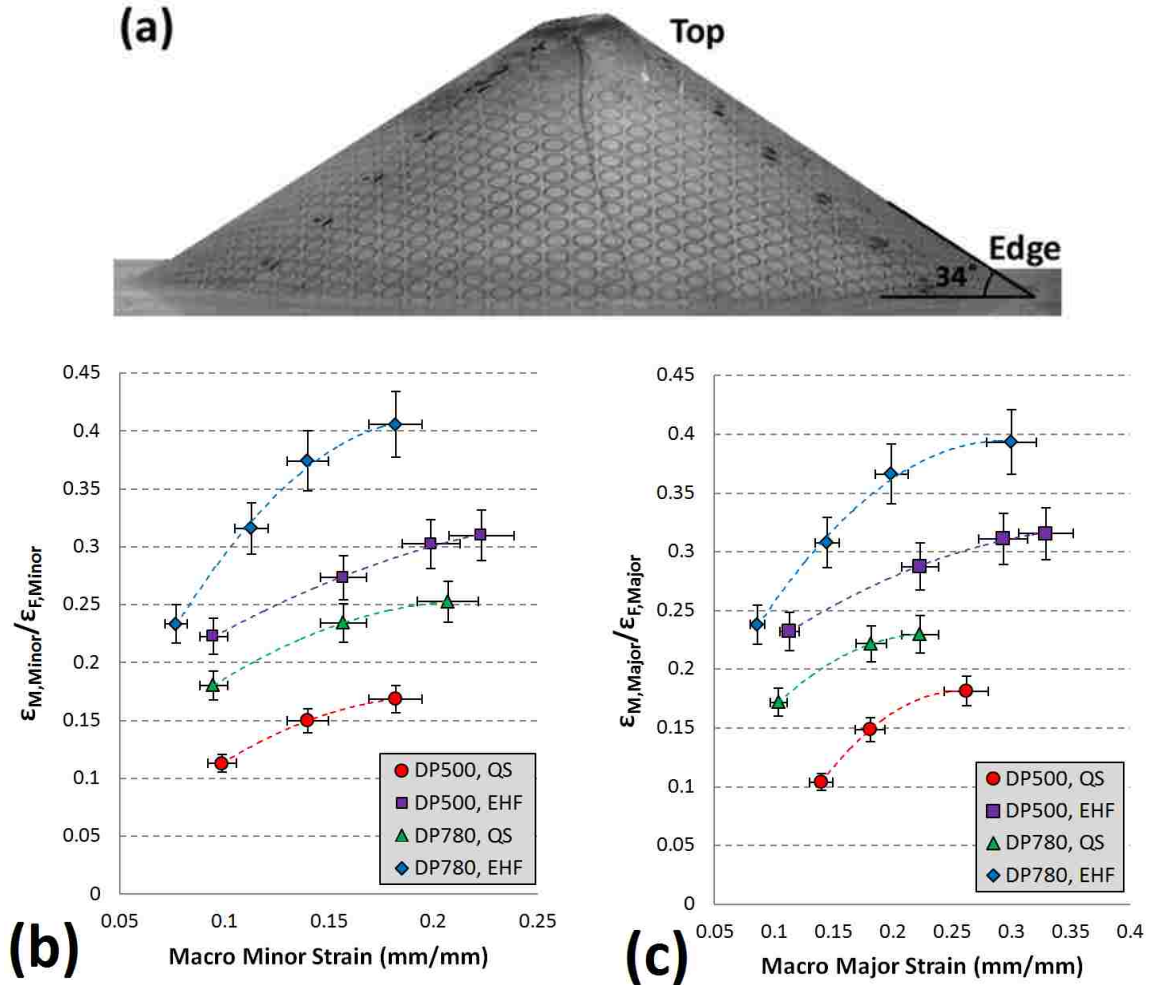


Figure 6-17 (a) Conical specimen formed by EHF, and martensite to ferrite (b) minor and (c) major strain ratio under quasi-static (QS) and high strain rate (EHF) forming conditions. Note that the volume fraction of martensite in DP500 and DP780 was 10% and 23%, respectively.

6.5 Correlation of Work Hardening and Hyperplasticity

Analysis of work hardening in ferrite grains formed under quasi-static and high strain rate conditions was carried out by means of Vickers microhardness. The hardness tests were conducted in a way that the position of indentations was adjusted inside the larger ferrite grains to eliminate the influence of grain boundaries and martensite islands. Figure 6-18, Figure 6-19, and Figure 6-20 present the results of the microhardness tests. As it can be seen, the initial hardness of ferrite in DP780 and DP980 was greater than

that in DP500 due to the greater amount of alloying elements in DP780 and DP980 which made stronger solid solutions.

For the specimens formed under quasi-static and high strain rate conditions, cubic functions were fitted to the data. These curves can be analyzed in terms of the rate of work hardening with respect to strain, i.e. $dH/d\bar{\epsilon}$, where H is the hardness and $\bar{\epsilon}$ is the effective strain. For the Nakazima specimens, there was a small continuous decrease in the work hardening rate of the ferrite grains. However, the curves of the EHF specimens can be divided into two parts: before and after the inflection point. In the first part, the work hardening rate decreases whereas in the second part the work hardening rate starts to increase.

In the ferrite grains of both the Nakazima and EHF specimens, there is a high initial work hardening rate due to the uniform deformation of the ferrite in the vicinity of martensite islands. The initial variation in the hardness of ferrite (up to $\bar{\epsilon} = 0.20$) is shown in Figure 6-21 for DP500, DP780, and DP980 which have martensite contents of 0.10, 0.23, and 0.34 vol%, respectively. As can be seen, the initial enhancement of hardness was greater in dual phase steels with higher martensite content. The reason can be attributed to the greater number of mobile dislocations at the ferrite/martensite interface which were produced during the austenite-to-martensite phase transformation. The number of dislocations was greater when the volume fraction of martensite was higher. The presence of dislocations resulted in the initial deformation and work hardening in ferrite grains.

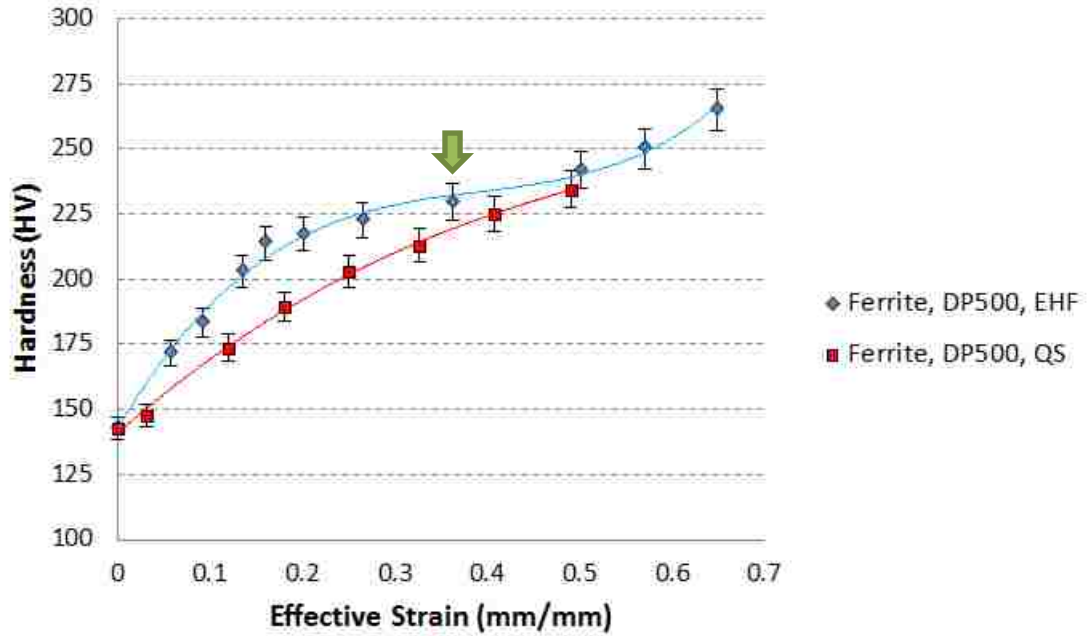


Figure 6-18 Hardness of ferrite in DP500 as a function of effective strain. The arrow shows the inflection point of the hardness curve at which the hardness rate started to increase in EHF.

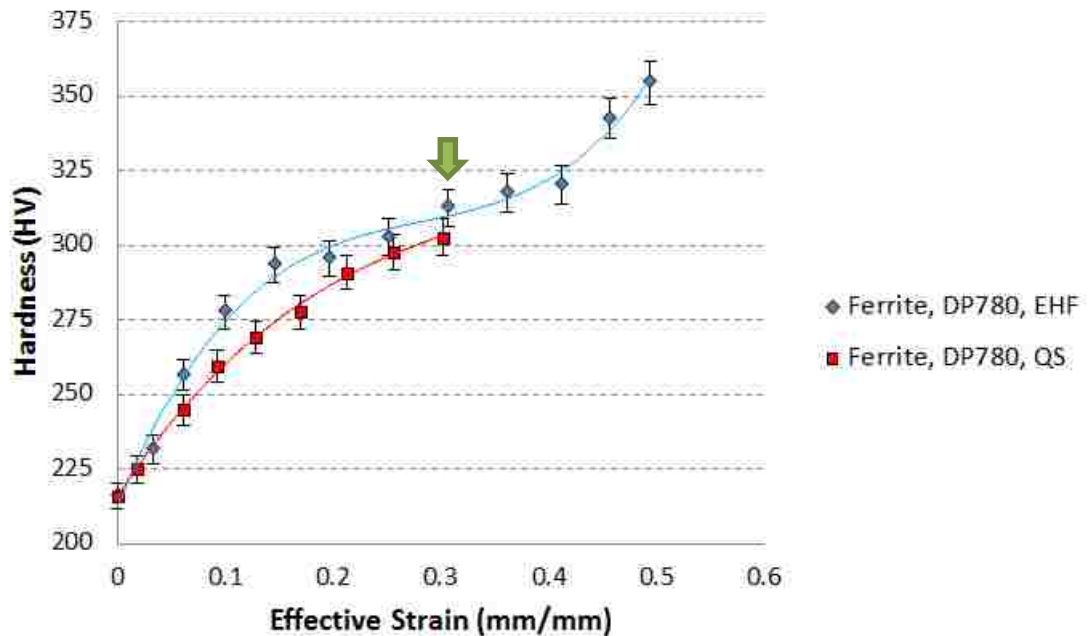


Figure 6-19 Hardness of ferrite in DP780 as a function of effective strain. The arrow shows the inflection point of the hardness curve at which the hardness rate started to increase in EHF.

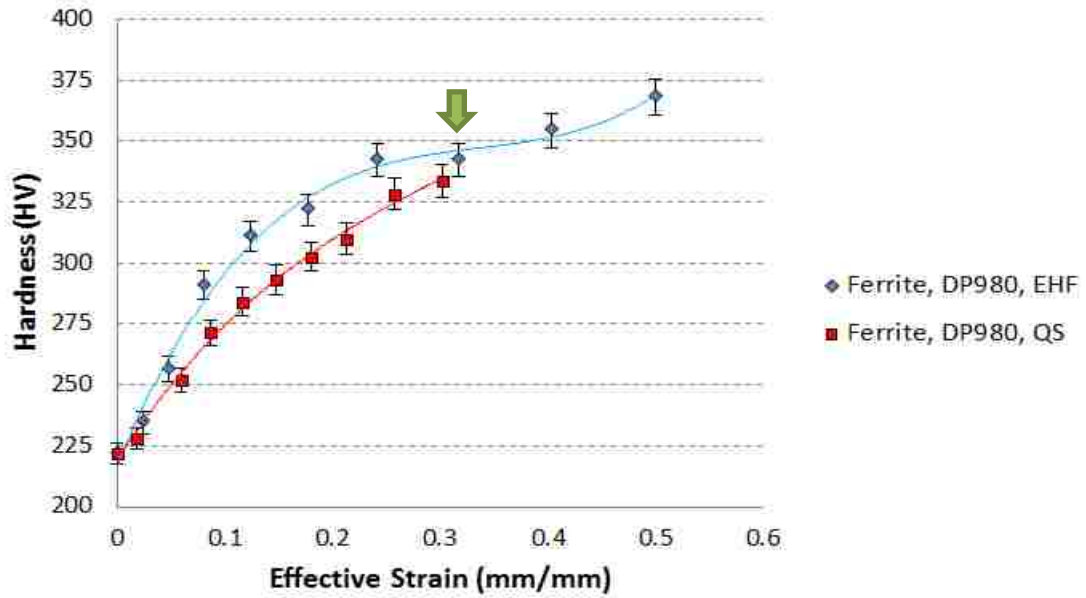


Figure 6-20 Hardness of ferrite in DP980 as a function of effective strain. The arrow shows the inflection point of the hardness curve at which the hardness rate started to increase in EHF.

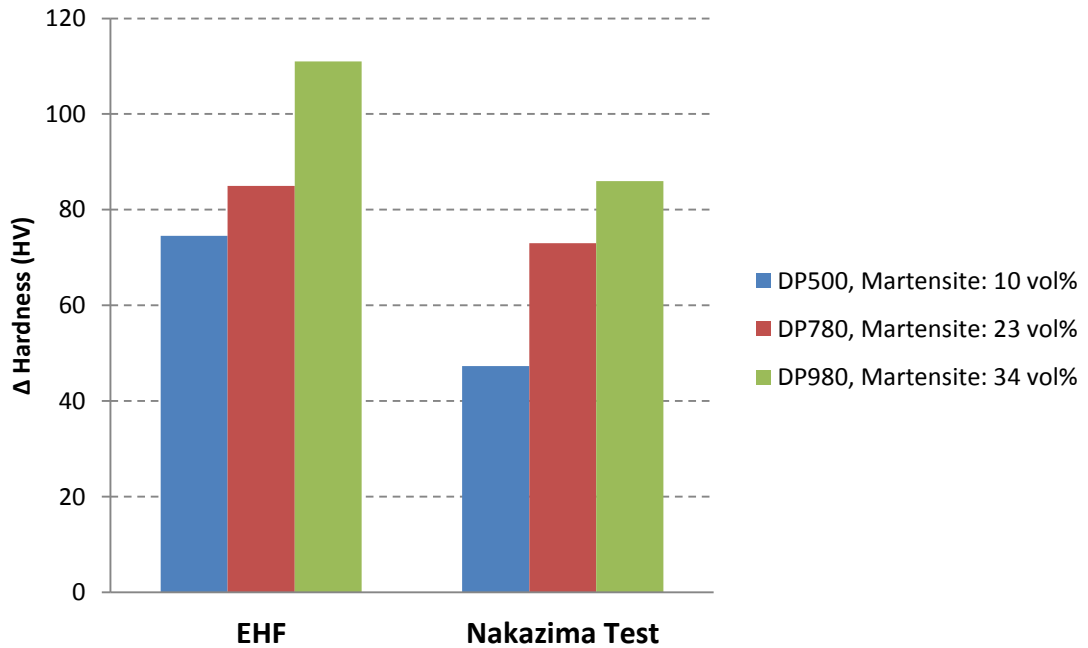


Figure 6-21 Increase in hardness of ferrite grains in dual phase steels up to an equivalent strain of 0.20 (mm/mm).

After the initial work hardening, the rate of work hardening gradually decreased. At this point, when the external loading is increased in a Nakazima test under quasi-static forming condition, there are not sufficient mobile dislocations throughout the microstructure to continue uniform plastic deformation. Consequently, necking begins and micro-cracks form and propagate due to the high localized stress concentrations. However, as mentioned in Section 6.3.2, at the strain level at which necking begins under quasi-static forming, the strain rate in EHF reached over 5000 s^{-1} which results in the nucleation of new mobile dislocations that enable further uniform plastic deformation in the specimens. So, there is a significant increase in dislocation density, and consequently the work hardening rate increases.

Hardness tests were also carried out using greater penetrating loads. Hence, the size of the indentation was large enough to cover a few ferrite grains and martensite islands. These results are shown in Figure 6-22. As can be seen, similar to the hardness of the ferrite grains, the hardness of the steels increases up to a certain level. Then, as it is shown by the arrows, there is an increase in hardness at an effective strain of 0.2-0.3 (mm/mm). This is the strain level at which the contact between the sheet and die becomes so influential that “inertial ironing” starts to participate more effectively and the strain rate exceeded 5000 s^{-1} . As mentioned above, the increases in hardness can be attributed to the nucleation of new dislocations which significantly increase the dislocation density.

In the case of EHF specimens, after nucleation of dislocation began and work hardening started to increase, uniform deformation was continued mostly by the new dislocations. However, eventually, dislocation density reached a saturation level. Therefore, the nucleation of new dislocations is no longer possible, and the material reaches the limit of uniform plastic deformation. Consequently, strains localize, necking begins, and post-uniform deformation proceeds.

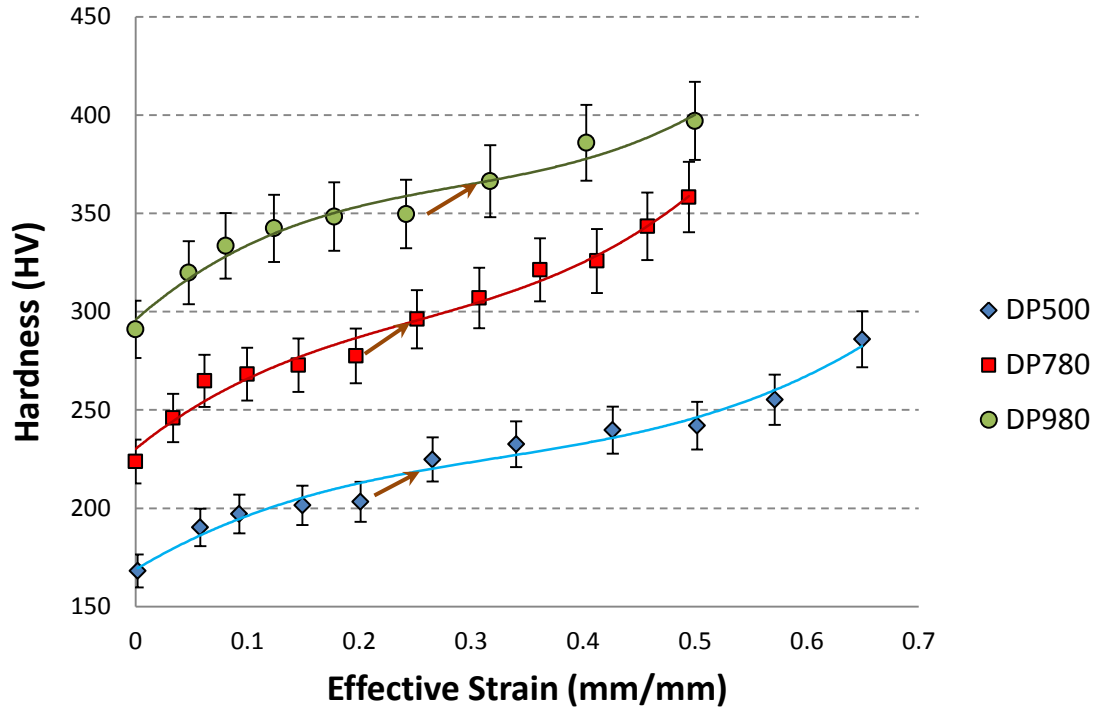


Figure 6-22 Hardness of dual phase steels formed by EHF as a function of effective strain. Arrows show the increase in the hardness of the steels due to the nucleation of dislocations.

6.6 Adiabatic Shear Bands

More than 500 micrographs were taken from the specimens at magnifications of $\times 100$ to $\times 15000$. However, no adiabatic shear bands were observed in these images. It seems that, although significant shear stresses were generated in EHF specimens, they did not result in adiabatic shear bands in these dual phase specimens.

Chapter 7*

7 Characterization of Failure in Dual Phase Steels Subject to EHF

Dual phase steels are known as ductile materials in which failure occurs based on the nucleation and growth of voids. In this chapter, mechanisms of failure in dual phase steels formed under quasi-static and EHF conditions are presented. For this purpose, the nucleation, growth, and volume fraction of voids were studied. Also, fractography was carried out to understand different types of fractures in the three grades of dual phase steels formed under quasi-static and high strain rate conditions. The main objective of this work was to determine how failure was suppressed in the EHF specimens formed in the conical die compared to the Nakazima specimens.

7.1 Nucleation and Growth of Voids

Microscopic analysis of the voids showed that under both quasi-static and high strain rate deformation, voids nucleated in two steps. In the beginning of plastic deformation, at lower strain levels, voids nucleate by cracking and separation of the martensite band. However, at higher strains, voids nucleate at the ferrite/martensite interface due to decohesion of the interface. Meanwhile, voids were found to nucleate inside the martensite islands or bands. In the following sections, the nucleation of voids is investigated in different grades of dual phase steels formed under quasi-static and EHF conditions.

* This chapter contains material that is the outcome of the joint research.

7.1.1 Nucleation of Voids due to Cracking of the Martensite Band

The amount of ferrite in the vicinity of martensite bands is less than the average fraction of ferrite in the overall microstructure. Due to the limited elongation of martensite, the local plastic strain in the vicinity of martensite bands cannot be safely accommodated in the microstructure. Hence, cracking of martensite bands occurred even at low strain levels. This can be seen in Figure 7-1 which shows that voids were created due to martensite cracking.

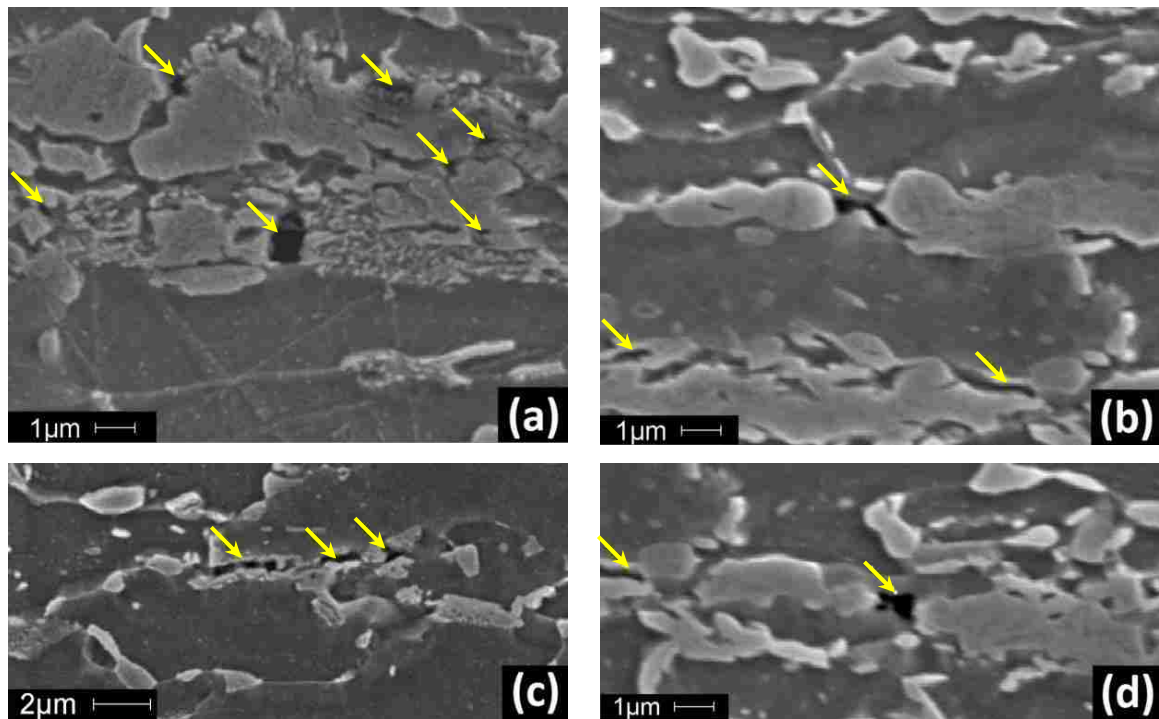


Figure 7-1 Nucleation of voids as a result of cracking and separation in the martensite bands in (a) DP500, and (b) DP780 Nakazima specimens, and (c) DP500, and (d) DP780 EHF specimens.

7.1.2 Nucleation of Voids inside the Martensite Islands and Band

As can be seen in Figure 7-2, nano-size voids were found to exist inside the martensite islands and bands. According to the higher carbon content of martensite in DP500 and DP780, work hardening of martensite in these grades was stronger than in DP980. Hence, the growth of voids that nucleated inside the martensite islands in DP500

and DP780 was very limited. However, due to the somewhat softer martensite in DP980, as it is shown in Figure 7-2-c, partial coalescence of voids was observed (red arrows). In conclusion, the nucleation of voids inside the martensite islands and bands was not found to be a micro-mechanism of failure in dual phase steels due to their limited growth in this hard phase.

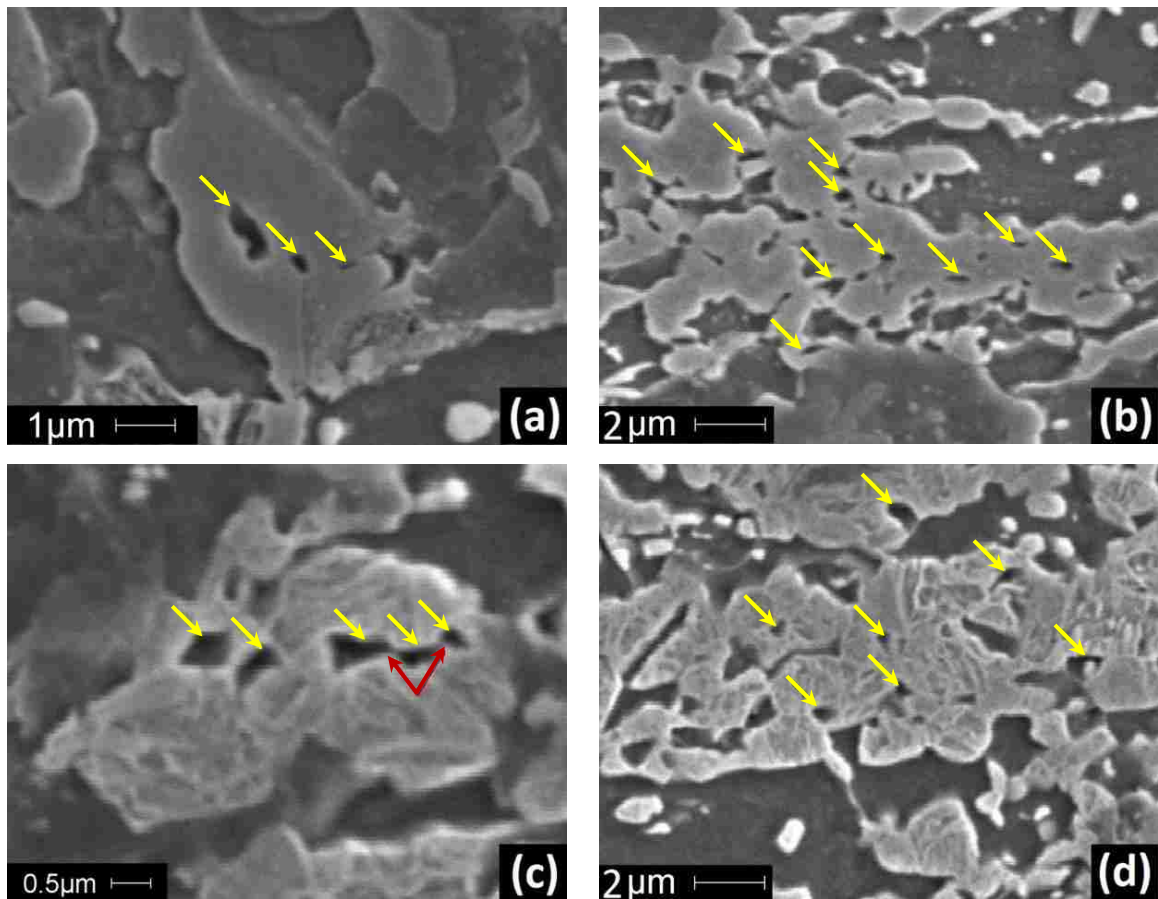


Figure 7-2 Voids inside martensite islands in (a) DP500 formed by EHF, (b) DP780 formed by EHF, (c) DP980 by the Nakazima test, and (d) DP980 formed by EHF.

7.1.3 Nucleation of Voids at the Ferrite/Martensite Interface

At higher strain levels, the accumulation of dislocations at the ferrite/martensite interface significantly increases local work hardening and induces strain gradients. As illustrated in Section 6.4, enhanced plastic compatibility between ferrite and martensite under EHF reduced the strain gradient in the ferrite/martensite interface to some

extent; however, at higher strain levels decohesion eventually did occur. As can be seen in Figure 7-3, nano-voids nucleated at the interface as an atomistic mechanism of strain relaxation. Two types of void growth were recognized depending on the direction of the strain gradient:

- interfacial growth occurred when aggregation of dislocations was along the ferrite/martensite interface, and
- growth into the ferrite grain occurred when dislocation pile-ups existed inside the ferrite grain.

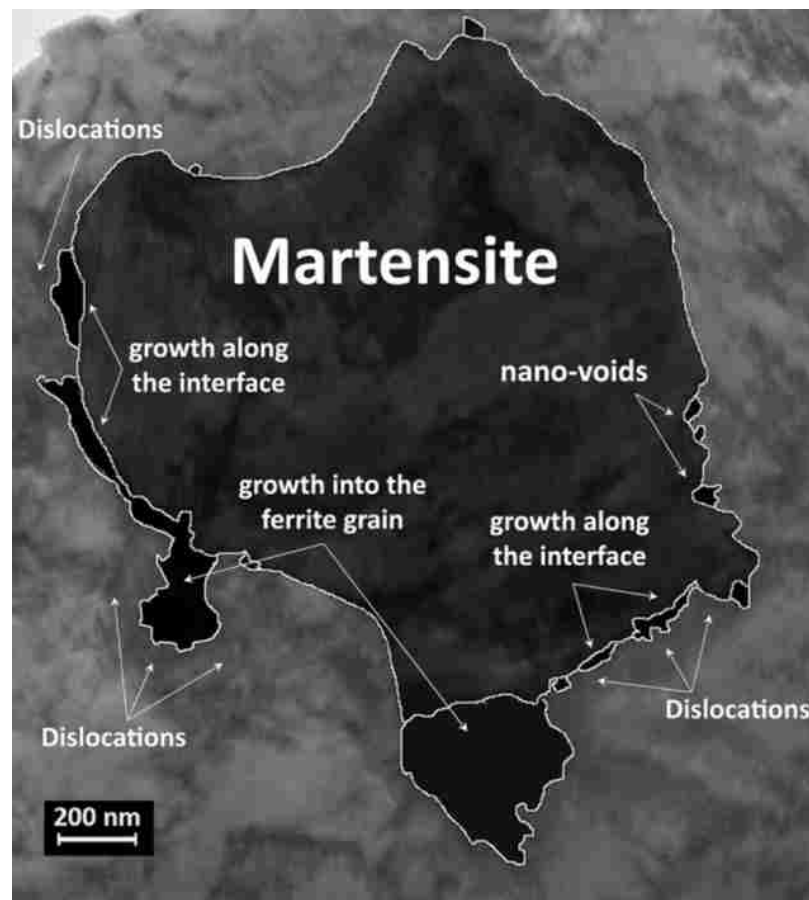


Figure 7-3 TEM image of DP780 specimen formed by EHF. Dislocation accumulation at the ferrite/martensite interface resulted in local strain gradient and decohesion at the interface. As a result of decohesion, nucleation and growth of nano-voids occurred.

According to the observations, growth of the voids along the ferrite/martensite interface was the dominant type of void growth since it resulted in the formation of micro-cracks. Figure 7-4 shows three micro-cracks that occurred at the ferrite/martensite interface.

As a conclusion, qualitative investigations on the initiation of voids in DP500, DP780, and DP980 specimens formed in both the Nakazima test and EHF showed similar sequences and mechanisms of void nucleation. Hence, the quantitative analysis of voids, as the predominant micro-mechanism of failure, was required to understand the reason for the suppression of failure in dual phase steel specimens formed by EHF.

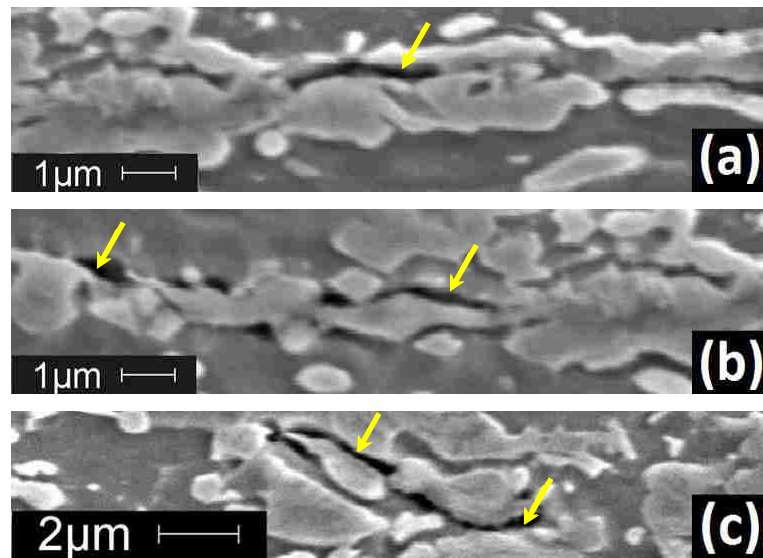


Figure 7-4 Micro-cracks at the ferrite/martensite interface of (a) DP780 Nakazima specimens, (b) DP780 EHF specimen, and (c) DP980 Nakazima specimens.

7.2 Quantitative Analysis of the Voids

In order to understand the effect of EHF on the micro-mechanisms of failure in dual phase steels, void volume fraction was measured across the specimen. For this purpose, several high resolution through-thickness micrographs of the as-polished specimens were taken and analyzed with the image analysis software. As an example, Figure 7-5 shows the voids in the DP500 EHF specimen at different levels of strain. The voids are

shown as black spots in the white matrix. As it can be seen, the density of the voids is higher in the middle of the micrographs where the martensite band lies.

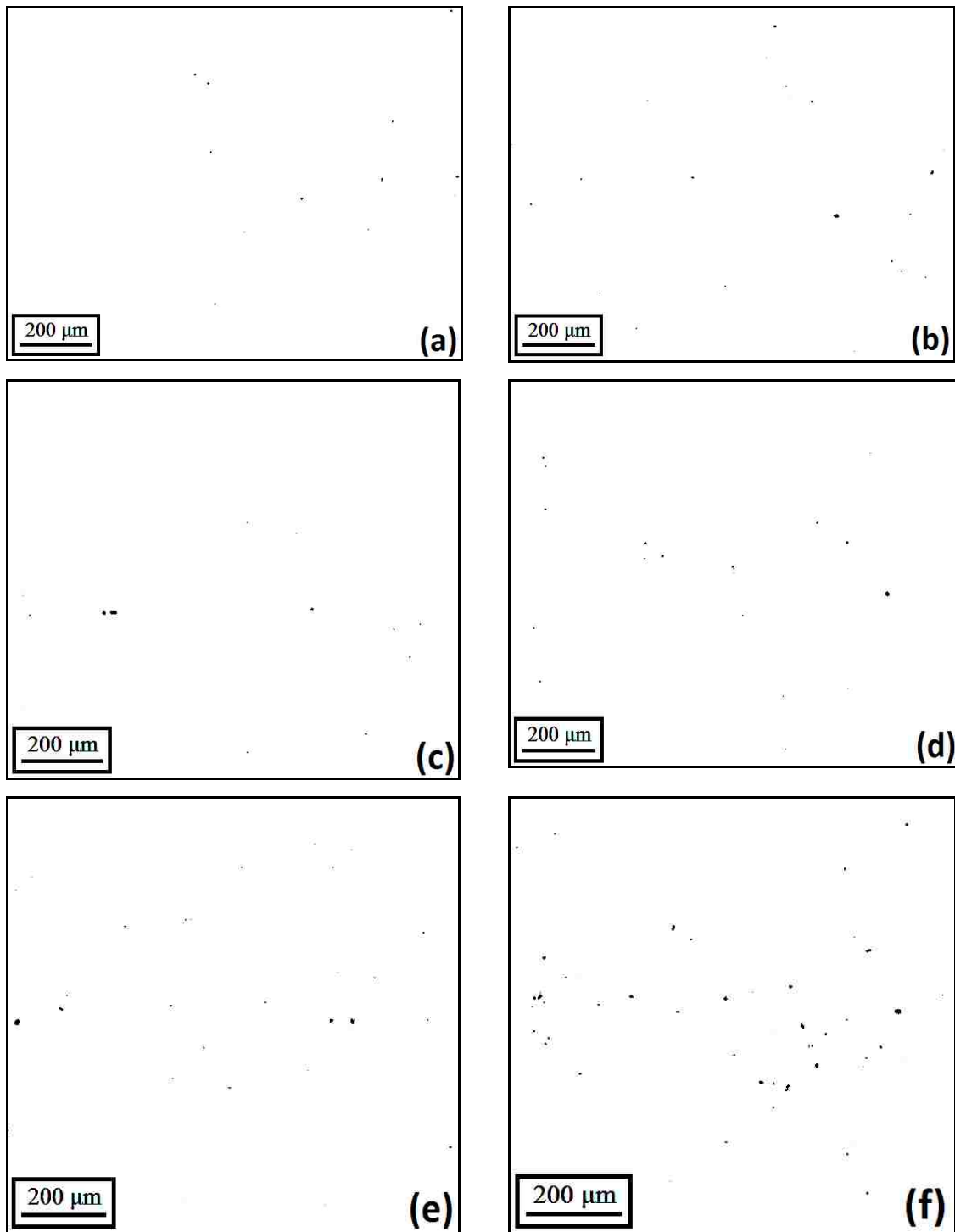


Figure 7-5 Voids in DP500 EHF specimen at strain: (a) 0.1, (b) 0.2, (c) 0.3, (d) 0.4, (e) 0.5, and (f) 0.6 (mm/mm). Black spots are the voids in the white matrix.

Quantitative analysis of the voids was carried out to determine the void volume fraction in the Nakazima and EHF specimens. The image analysis software Clemex Vision Pro was used to determine the void volume fraction in the specimens at different strain levels according to:

$$\text{VoidVolumeFraction} = \frac{\text{Void Area}}{\text{Void Area} + \text{Matrix Area}} \quad (7-1)$$

The surface area of the black and white regions, as it is shown in Figure 7-5, represent the **Void Area** and the **Matrix Area**, respectively. Results are shown in Figure 7-6. As can be seen, at the same strain level, the void volume fraction was lower in the EHF specimens compared to the Nakazima specimens. The reason attributed to the significant compressive and shear stresses due to the impact of the sheet against the die that acts against void growth. Therefore, under EHF, the coalescence of voids to form micro-cracks was postponed to higher strain levels which resulted in a formability improvement.

The mean area of the voids in the specimens at different strain levels was determined by the image analysis software according to:

$$\text{Void Mean Area} = \frac{\text{Void Area}}{\text{Number of Voids}} \quad (7-2)$$

On account of the resolution of the micrographs, the smallest void that was taken into account had a surface area of $0.067 \mu\text{m}^2$. The **Void Mean Area** was a function of both void nucleation and void growth. While the growth of voids increased the mean area of the voids (due to the increase of the **Void Area**), the nucleation of the new small voids decreased it (due to the increase of the **Number of Voids**). The **Void Mean Area** at different strain levels are shown in Figure 7-7.

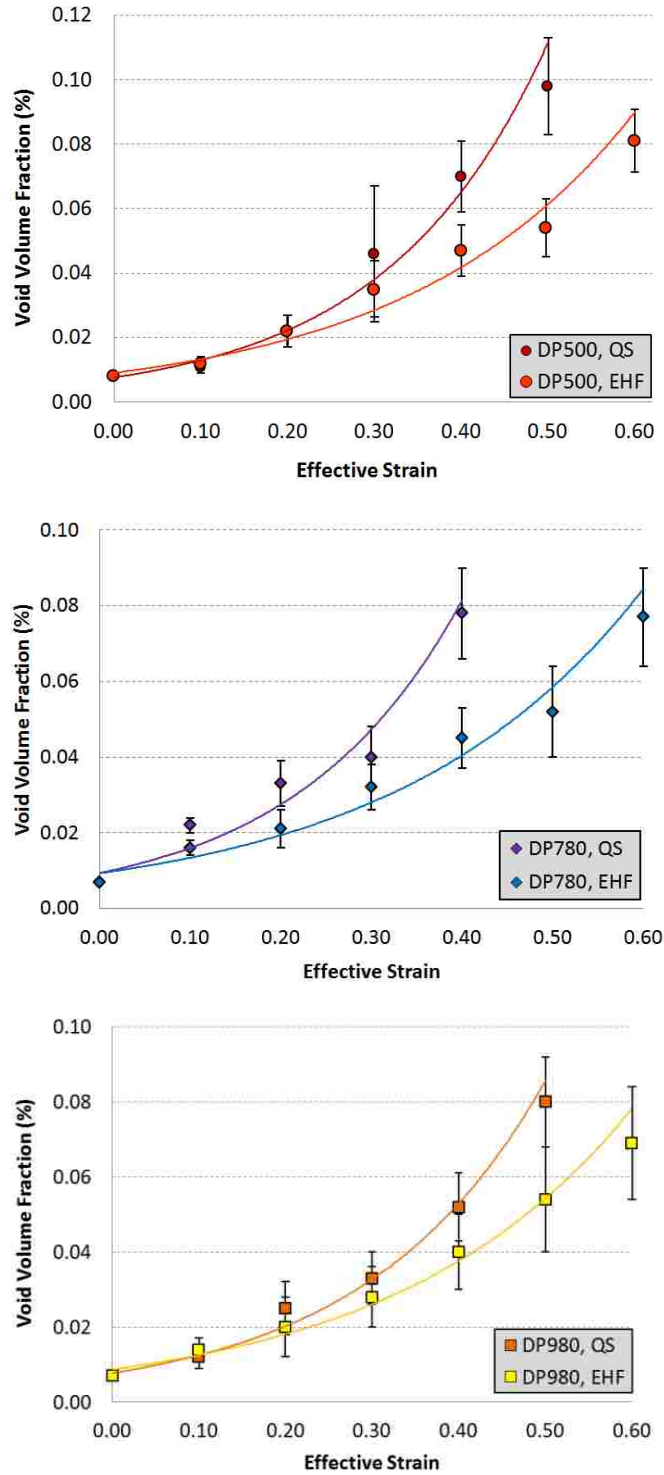


Figure 7-6 Void volume fraction as a function of strain in (a) DP500, (b) DP780, and (c) DP980, formed in a Nakazima test (QS) and by EHF.

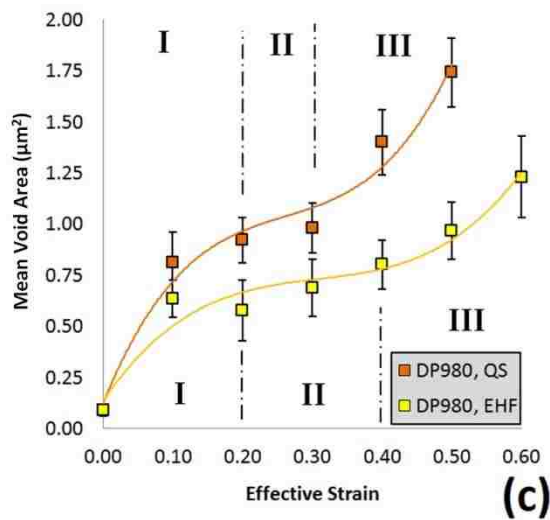
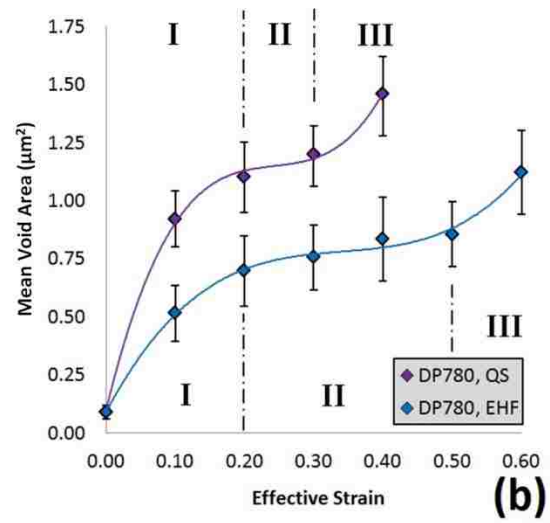
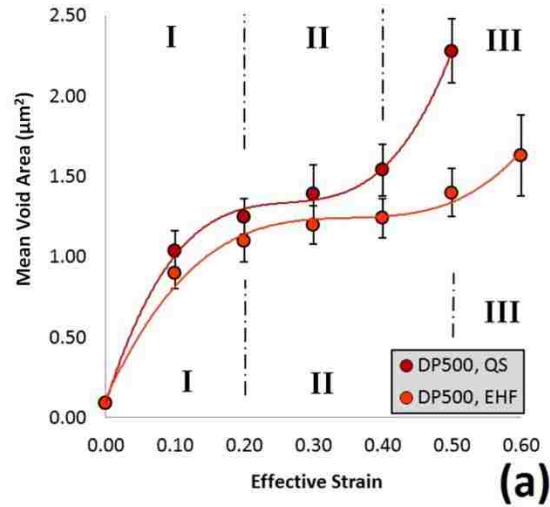


Figure 7-7 Void area as a function of strain in (a) DP500, (b) DP780, and (c) DP980, formed in a Nakazima test (QS) and by EHF.

According to the curves presented in Figure 7-7 and the mechanisms of void nucleation and growth described in Section 7.1, three stages can be recognized in the curves:

- Stage I At effective strains < 0.20 (mm/mm)
Void nucleation and growth mostly inside the martensite and due to the martensite cracking
- Stage II Void nucleation and growth in martensite
Beginning of nucleation and growth of voids at the ferrite/martensite interface
- Stage III Nucleation and rapid growth of voids in the martensite and at the ferrite/martensite interface at high levels of stress

In Stage I, the rate of void growth is greater than the rate of void nucleation. Hence, a rapid increase in the **Void Mean Area** was observed. However, in stage II, the rate of void nucleation increased significantly. There were several new voids nucleated at the ferrite/martensite interface that consequently reduced the increasing rate of **Void Mean Area**. In Stage III, where the flow stress was increased, the rate of **Void Mean Area** started to increase again. The reason may be attributed to the rapid growth of the existing voids at that high stress level, and also due to the beginning of the coalescence of the voids to form micro-cracks.

As can be seen in Figure 7-7, stage II in the EHF specimens extended to higher strain levels compared to the Nakazima specimens. The reason was that in stage II, as the strain increased beyond 0.20, the influence of die impact becomes increasingly more significant. Hence, the compressive and shear stresses generated by the impact against the die inhibited the void growth. On the other hand, as mentioned in Section 6.4, enhanced plastic compatibility between the ferrite and martensite reduced the risk of decohesion at the interface, and consequently the rate of void growth. The delay in void growth can also be considered as another reason for the suppression of failure in the EHF specimens.

Comparing the rate of increase of the **Void Mean Area** in Stage III, between the Nakazima and EHF specimens; although Stage III in the EHF specimens occurred at higher strain levels, the rate of **Void Mean Area** was smaller in the EHF specimens. This may also be a result of compressive stresses due to the impact of the sheet against the die. Reduction of the rate of increase of the **Void Mean Area** in the third stage has a significant effect on the hyperplasticity of the EHF specimens, since it significantly suppresses the coalescence of voids and the formation of micro-cracks.

7.3 Fractography of Dual Phase Steels subject to EHF

High resolution FESEM images were taken to study the fracture surfaces of the Nakazima and EHF specimens. As expected for dual phase steels, ductile fracture was the dominant type of fracture in all of the specimens; however, quasi-cleavage and shear fracture were also observed in the EHF specimens.

Ductile Fracture As shown in Figure 7-8, Figure 7-9, and Figure 7-10, fracture surfaces of the specimens formed under quasi-static as well as high strain rate forming conditions showed ductile fracture with two characteristic features:

- Dimples which covered the background of the images were formed due to the nucleation of voids near the ferrite/martensite interface, and
- Parallel striations existed due to cracking and consequently detachment of the martensite bands from the ferrite matrix.

Quasi-Cleavage Fracture In addition to the ductile fracture, quasi-cleavage fracture was also observed in DP780 and DP980 specimens. Figure 7-11 presents two examples of quasi-cleavage fracture in DP780 specimens formed in the Nakazima test and by EHF. Quasi-cleavage fracture has been defined as follows: “Quasi-cleavage is related but distinct to cleavage fracture. It often exhibits dimples and tear ridges around the periphery of the facets.” [70] The number of cleavage surfaces was greater in DP980 with higher martensite content. Also, it was observed more often in the specimens

formed under EHF where more significant shear stresses existed to create cleavage surfaces.

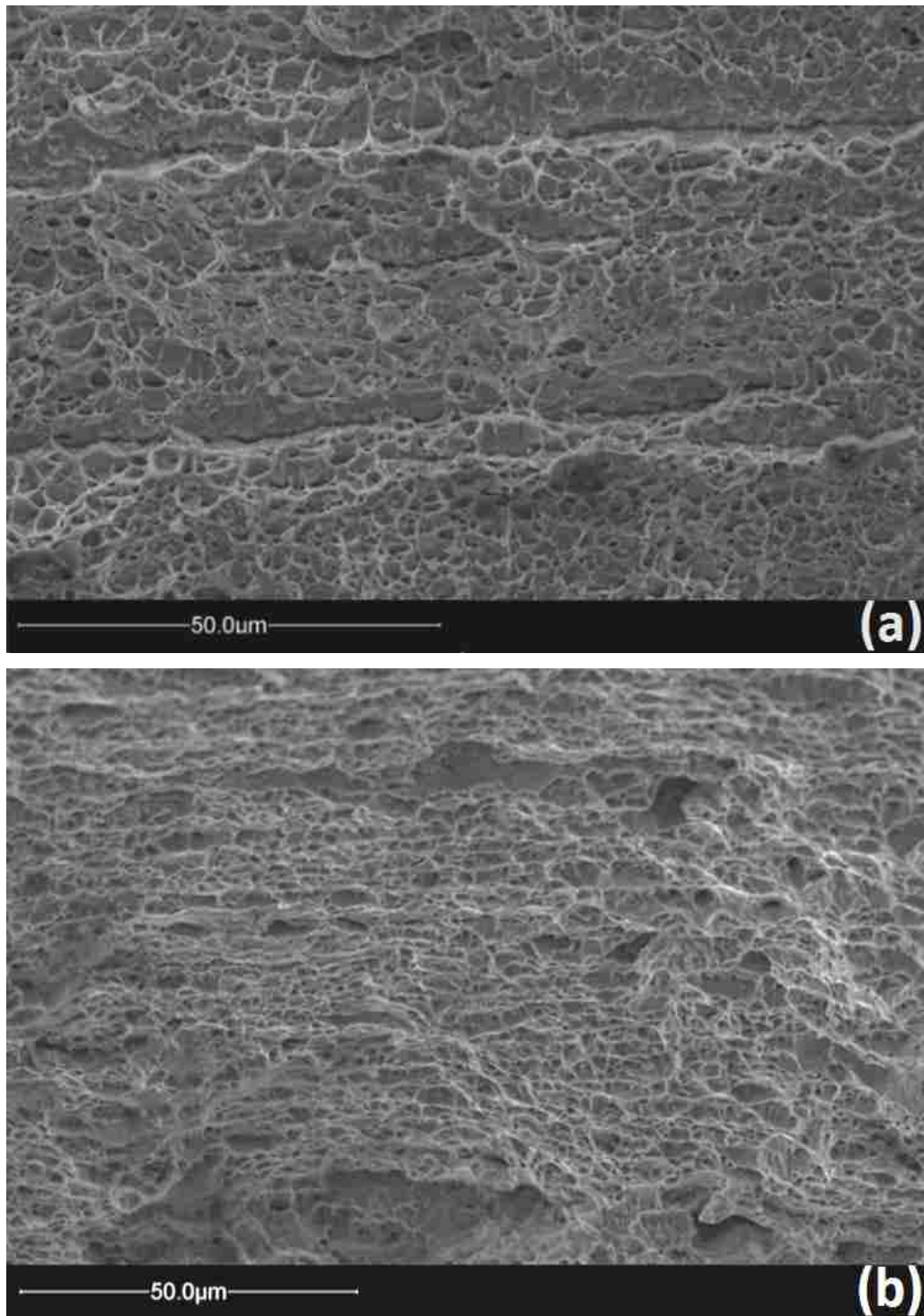


Figure 7-8 Ductile fracture in (a) DP500, and (b) DP780 formed in the Nakazima test.

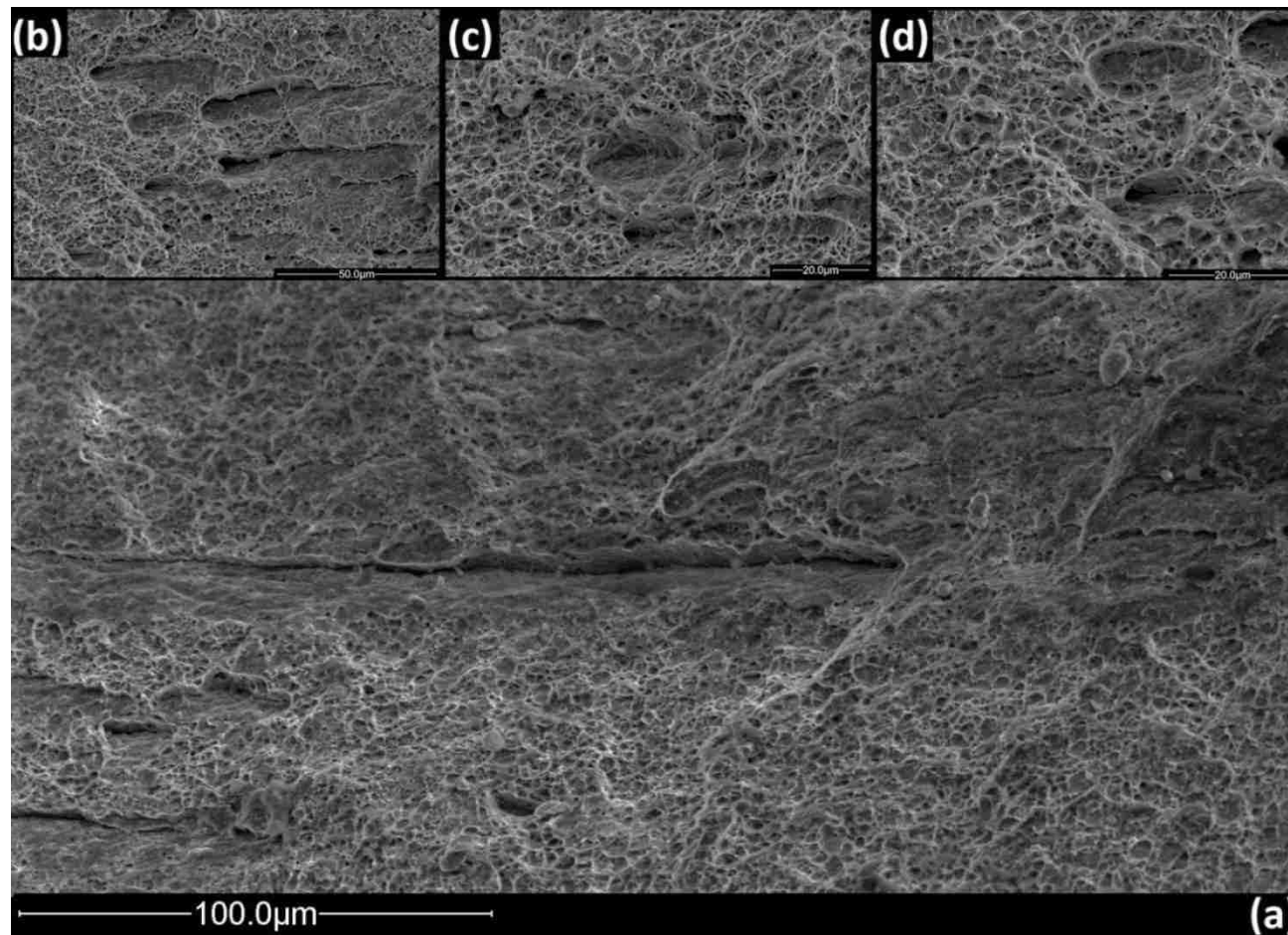


Figure 7-9 Ductile fracture in DP980 formed in the Nakazima test (a) general view, and (b), (c), and (d) detached martensite islands.

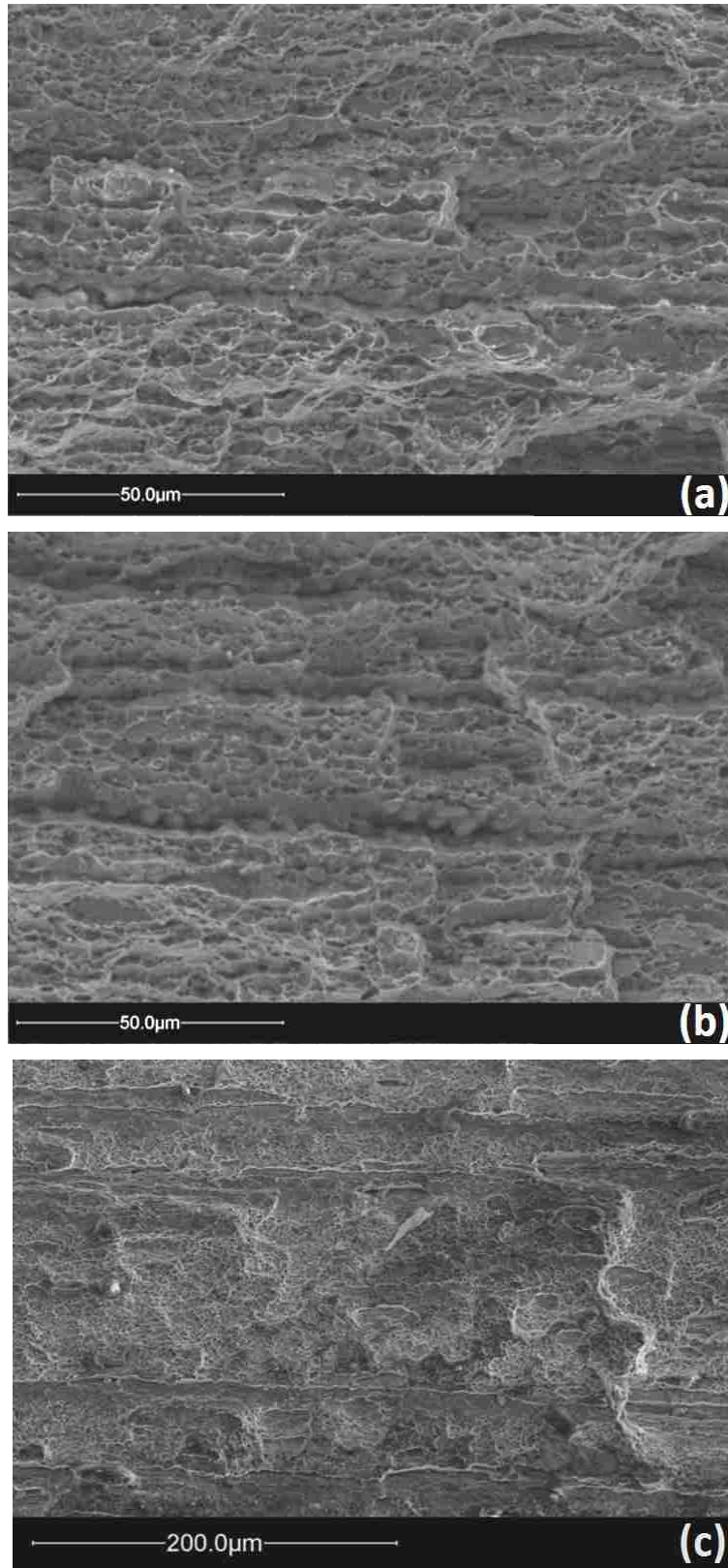


Figure 7-10 Ductile fracture in (a) DP500, (b) DP780, and (c) DP980 formed by EHF.

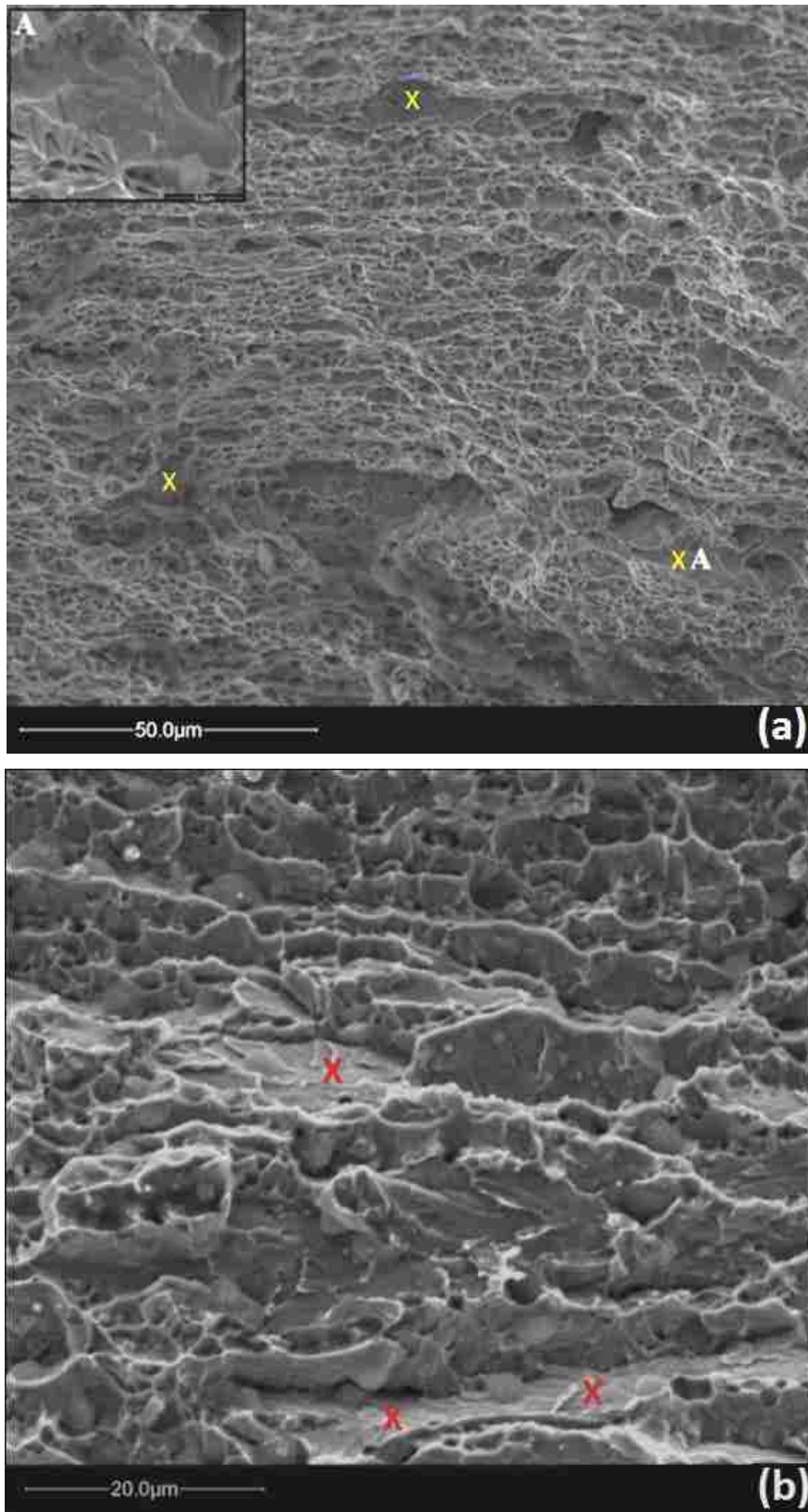


Figure 7-11 Quasi-cleavage fracture in DP780 formed in the (a) Nakazima test, and (b) by EHF.

Shear Fracture Shear fracture was only observed in the EHF specimens. Elongated horseshoe-shaped dimples, which are shown by the arrows in Figure 7-12, are the evidences of shear fracture. A shear fracture occurs as the result of extensive slip on the activate slip plane due to shearing stresses. Hence, the reason for shear fracture in EHF should be mainly attributed to the die effect and specifically “inertial ironing” phenomenon which results in very large shear forces. As can be seen in Figure 7-12, elongation of the dimples was more significant in DP500 compared to DP780 and DP980. The reason is the greater volume fraction of martensite in DP780 and DP980 which resist to the shear forces.

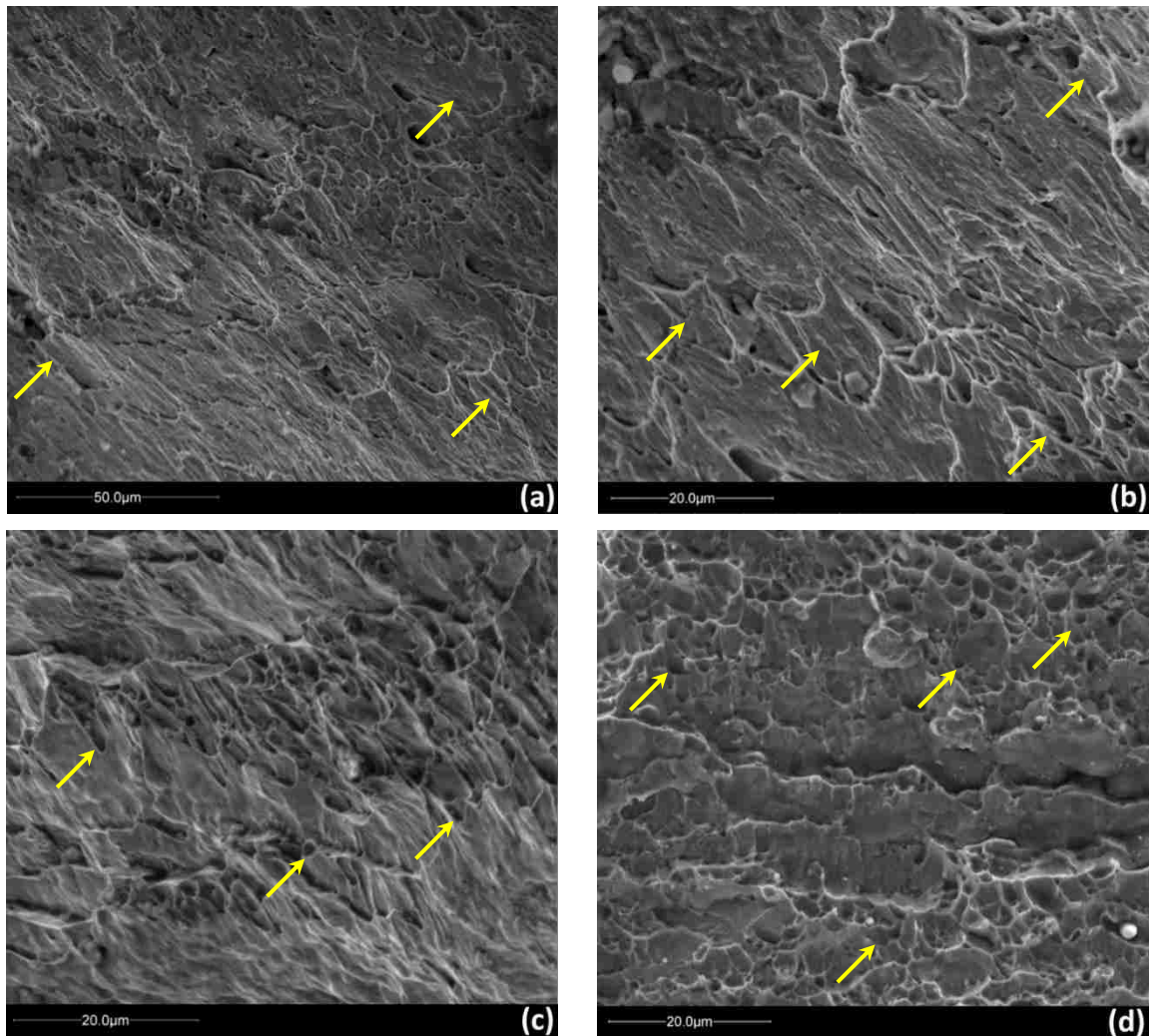


Figure 7-12 Shear fracture in (a) DP500, (b) DP500 with greater magnification, (c) DP780, and (d) DP980 formed by EHF

Chapter 8

8 Conclusions

In this research, three grades of dual phase steel were formed under quasi-static and high strain rate conditions using the Nakazima test and EHF, respectively. Hyperplasticity was observed in the specimens formed under EHF when a 34° conical die was used. The goal of this research was to identify multi-scale mechanisms of hyperplasticity and failure in dual phase steels formed under EHF. The following are the most important results of the research which are categorized according to the scale of observation.

8.1 Macro-scale Conclusions

Formability Improvement Three commercial DP500, DP780, and DP980 dual phase steels were deformed by EHF both without using a die and with a 34° conical die. Comparison of the major vs. minor strains in the specimens with the quasi-static forming limit curves showed a formability improvement for the EHF specimens formed into the conical die; however, there was no formability improvement in the specimens that were formed without using a die. The formability improvement was significant for DP780 and DP980 whereas it was not that significant for DP500 since it already had good formability under quasi-static forming conditions.

Defects Necking and cracking were the common defects in the Nakazima and EHF specimens. However, in the case of the specimens formed by EHF using the 34° conical die, a slight increase in the input energy caused rebounding instead of splitting.

8.2 Micro-scale Conclusions

Relative Deformation Improvement Quantitative metallography was carried out on thousands of ferrite grains and martensite islands in the deformed DP500 and DP780 specimens. Results showed that the safe deformation of the constituents reached significantly greater strains under EHF. Moreover, the level of deformation improvement was greater for the harder martensite phase. The martensite in DP500 and DP780 showed a relative deformation improvement of approximately 100% whereas the improvement in ferrite was only about 20%. This in turn resulted in greater macro-scale formability improvement in DP780 with greater martensite content.

Failure The nucleation and growth of voids in the martensite at lower strain levels and at the ferrite/martensite grain boundary at higher strain levels were found to be the micro-mechanisms of failure in dual phase steels formed in both the Nakazima test and by EHF. However, in terms of micro-mechanisms, failure of the EHF specimens formed into the 34° conical die was suppressed due to enhancement of the ferrite and martensite plastic compatibility which reduced the rate of nucleation and growth of voids at the ferrite/martensite interface. Furthermore, in the case of EHF specimens, the rate of void growth was decreased due to the high velocity impact of the sheet against the die which generated large through-thickness compressive and shear stresses. The effect of these compressive and shear stresses on the reduction of the rate of void growth was significant, specifically in the second stage of the growth. As a result, the formation and propagation of micro-cracks was suppressed, which eventually resulted in formability improvement.

Fracture Fractography of the three dual phase steels showed that ductile fracture was the dominant type of fracture. In all specimens, dimples and parallel striations were observed in the fracture micrographs which were formed due to the interfacial nucleation of voids and cracking and detachment of the martensite bands, respectively. Quasi-cleavage fracture was also observed in the DP780 and DP980 Nakazima and EHF specimens. The amount of quasi-cleavage fracture was greater in the EHF specimens due to the more significant shear stresses which caused cleavage surfaces. Finally, elongated

horseshoe like dimples were found in the fracture surfaces of the specimens formed by EHF as the evidences of shear fracture. The elongation of the dimples was reduced by increasing the martensite content, i.e. DP500>DP780>DP980, because of resistance of martensite to shear forces.

8.3 Nano-scale Conclusions

Dislocations' Configuration TEM observations showed accumulation of dislocations in the vicinity of the ferrite/martensite interface in all the dual phase steel grades formed both in the Nakazima test and by EHF. Hence, dislocation cells were formed in the vicinity of the ferrite/martensite interface in the Nakazima. However, since the duration of the EHF process was in the order of $10^2 \mu\text{s}$, there was not sufficient time for dislocations to form distinguishable configurations in the EHF specimens.

Dislocations and Hyperplasticity Due to the greater level of shear stresses in EHF, the motion and multiplication of dislocations were more feasible which lead to further plastic deformation. However, as the previous theories and the result of hardness test indicated, since the strain rate during EHF exceeded 5000 s^{-1} and increased to the order of $2 \times 10^4 \text{ s}^{-1}$, extensive nucleation of new dislocations occurred which should be mentioned as the main participation of dislocations in the hyperplasticity of dual phase steels in EHF.

Deformation Twinning Although deformation twinning was expected to be a major mechanism of deformation in BCC materials under high strain rate forming, the SAD analysis during TEM observations did not identify the widespread formation of deformation twins in ferrite grains; however, deformation twinning was found to be very prevalent in the harder martensite islands. Deformation twinning was found almost in all the martensite islands formed under EHF. This perhaps the reason for the approximately 100% relative deformation improvement of martensite in EHF.

Nucleation and Growth of Nano-voids Accumulation of dislocations at the ferrite/martensite interface significantly increases local work hardening and induces strain gradients. Hence, as an atomistic mechanism of strain relaxation, nano-voids

nucleate at the interface. Two types of void growth were recognized depending on the direction of the strain gradient: along the interface and toward the inside of the ferrite grains. The former type of growth was found to create interfacial micro-voids. Subsequent growth of the micro-voids formed micro-cracks at the ferrite/martensite interface which eventually resulted in failure.

8.4 Recommendations for Future Research

As mentioned before, the majority of previous investigations on high strain rate forming of dual phase steels were carried out under uniaxial loading conditions such as high speed uniaxial tensile tests and high strain rate forming by means of Split Hopkinson Bar tests. However, in EHF using a die, the state of stress is three-dimensional compared to uniaxial loading condition which affects the mechanisms of deformation and failure. For instance, as mentioned in Chapter 7, coexistence of tension and compression in EHF influenced the rate of the growth of voids. Hence, further investigations are required to achieve a better understanding of the behaviour of dual phase steels under the complex states of stress in EHF.

In this research, dual phase steel sheets were formed in EHF process using a conical die. The strain path in the formed specimens was very close to equibiaxial tension. As a recommendation for future research; it is essential to design different dies or specimens to investigate the formability improvement and micro-mechanical behaviour of dual phase steels along other strain paths, i.e. in different areas of the forming limit diagram.

The second recommendation is to form dual phase steel sheets under EHF from small input energies and gradually increase the energy to find the onset of hyperplasticity in the specimens. It would also be helpful to do these tests under different strain paths.

As a last recommendation, to have a better microscopic understanding of the effect of sheet to die impact as well as the inertial ironing, it is suggested to do EHF tests on dual phase steel sheets with different thicknesses. It may help to understand whether adiabatic shear bands will form in thicker sheets or not.

References

- [1] Williams, E. W., and Davies, L. K., 1963, "Recent developments in annealing," ISI Special Report, 79.
- [2] Hayami, S., and Furakawa, T., 1975, A family of high-strength cold-rolled steels, Union Carbide Corporation, New York.
- [3] Yan, B., and Dennis, U., April 2003, "Characterization of fatigue and crash performance of new generation high strength steels for automotive applications," U.S. Department of Energy.
- [4] Applications, I. I. S. I. C. o. A., 2006, "Advanced high strength steel (AHSS) application guidelines," American Iron and Steel Institute.
- [5] Shaw, J., 2009, "ULSAB-AVC on the road today," American Iron and Steel Institute.
- [6] Davies, R. G., 1978, "Influence of martensite composition and content on the properties of dual phase steels," Metallurgical Transactions A 9(5), pp. 671-679.
- [7] Davies, R. G., 1978, "The deformation behavior of a vanadium-strengthened dual phase steel," Metallurgical Transactions A, 9 (1), pp. 41-52.
- [8] Davies, R. G., 1979, "Early stages of yielding and strain aging of a vanadium-containing dual-phase steel," Metallurgical Transactions A 10(10), pp. 1549-1555.
- [9] Davies, R. G., and Magee, C. L., "Physical metallurgy of automotive high strength steels," Proc. In Structure and Properties of Dual-Phase Steels, R. A. Kot, and J. W. Morris, eds., TMS-AIME, pp. 1-19.
- [10] Speich, G. R., and Miller, R. L., 1979, "Mechanical properties of ferrite-martensite steels, in structure and properties of dual-phase steels," American Institute of Mining, Metallurgical, and Petroleum Engineers, pp. 145-182.
- [11] Speich, G. R., Demarest, V. A., and Miller, R. L., 1981, "Formation of austenite during intercritical annealing of dual-phase steels," Metallurgical transactions A, 12A(8), pp. 1419-1428.
- [12] Speich, G. R., Schwoeble, A. J., and Huffman, G. P., 1983, "Tempering of Mn and Mn-Si-V dual-phase steels " Metallurgical Transactions A, 14(6), pp. 1079-1087.
- [13] Speich, G. R., and Miller, R. L., "Hardenability of austenite after intercritical annealing of dual-phase steels," Proc. International Conference Solid-Solid Phase Transformations, H. I. Aaronson, D. E. Laughlin, R. F. Sekerka, and C. M. Wayman, eds., TMS-AIME, pp. 843-848.
- [14] Balliger, N. K., and Gladman, T., 1981, "Work hardening of dual-phase steels," Metal science, 15(3), pp. 95-108.
- [15] Balliger, N. K., 1982, Advances in physical metallurgy and applications of steels, The Metals Society.
- [16] Cai, X.-L., Feng, J., and Owen, W. S., 1985, "The dependence of some tensile and fatigue properties of a dual-phase steel on its microstructure," Metallurgical Transactions A, 16(8), pp. 1405-1415.
- [17] Cai, X.-L., Garratt-Reed, A. J., and Owen, W. S., 1985, "The development of some dual-phase steel structures from different starting microstructures," Metallurgical Transactions A, 16(4), pp. 543-557.

- [18] Marder, A. R., 1982, "Deformation characteristics of dual-phase steels," Metallurgical transactions A, 13A(1), pp. 85-92.
- [19] Marder, A. R., and Benscoter, A. O., 1982, "Quantitative microanalysis of dual-phase steels," Metallography, 15(1), pp. 73-85.
- [20] Marder, A. R., 1981, "Effect of heat treatment on the properties and structure of molybdenum and vanadium dual-phase steels " Metallurgical transactions A, 12A(9), pp. 1569-1579.
- [21] Samei, J., Green, D. E., Golovashchenko, S., and Hassannejadasl, A., 2013, "Quantitative Microstructural Analysis of Formability Enhancement in Dual Phase Steels Subject to Electrohydraulic Forming," Journal of Materials Engineering and Performance, 22(7), pp. 2080-2088.
- [22] Kim, N. J., and Thomas, G., 1981, "Effects of morphology on the mechanical behavior of a dual phase Fe/2Si/0.1C steel," Metallurgical and Materials Transactions A, 12(3), pp. 483-489.
- [23] Lanzillotto, C. A. N., and Pickering, F. B., 1982, "Structure-property relationship in dual-phase steels," Met Sci 16(8), pp. 371-382.
- [24] Ramos, L. F., Matlock, D. K., and Krauss, G., 1979, "On the deformation behavior of dual-phase steels," Metallurgical Transactions A, 10(2), pp. 259-261.
- [25] Hansen, S. S., and Pradhan, R. R., "Structure/property relationships and continuous yielding behaviour in dual-phase steels," Proc. In Fundamentals of Dual-Phase Steels, A. Kot, and B. L. Bramfitt, eds., TMS-AIME, pp. 113-143.
- [26] Sarosiek, A. M., and Owen, W. S., 1984, "The work hardening of dual-phase steels at small plastic strains," Materials Science and Engineering, 66(1), pp. 13-34.
- [27] Rigsbee, J. M., Abraham, J. K., Davenport, A. T., Franklin, J. E., and Pickens, J. W., 1979, "Structure-processing and structure-property relationships in commercially produced dual-phase steels," In Structure and Properties of Dual-Phase Steels, R. A. Kot, and J. W. Morris, eds., pp. 304-329.
- [28] Kim, S., and Lee, S., 2000, "Effects of martensite morphology and volume fraction on quasi-static and dynamic deformation behavior of dualphase steels," Metallurgical and Materials Transactions A, 12A, pp. 483-489.
- [29] Lee, H. S., Hwang, B., Lee, S., Lee, C. G., and Kim, S. J., 2004, "Effects of martensite morphology and tempering on dynamic deformation behavior of dual-phase steels," Metallurgical and Materials Transactions A, 35A, pp. 2371-2382.
- [30] Hwang, B.-C., Cao, T.-Y., Shin, S. Y., Kim, S.-H., Lee, S.-H., and Kim, S.-J., 2005, "Effects of ferrite grain size and martensite volume fraction on dynamic deformation behaviour of 0.15C–2.0Mn–0.2Si dual phase steels," Materials Science and Technology, 21(8), pp. 967-975.
- [31] Qu, J., Dabboussi, W., Hassani, F., Nemes, J., and Yue, S., 2008, "Effect of microstructure on the dynamic deformation behavior of dual phase steel," Materials Science and Engineering A 479(1-2), pp. 93-104.
- [32] Odeshi, A. G., and Bassim, M. N., 2008, "Evolution of adiabatic shear bands in a dual-phase steel at very high strain rates," Mateirlas Science and Engineering A, 488, pp. 235-240.

- [33] Xia, Y. M., and Zhou, Y. X., 2000, "The effect of strain rate and martensite volume fraction on tensile impact behavior of dual phase steels," *Key Engineering Materials*, 177-180, pp. 231-236.
- [34] Bleck, W., and Schael, I., 2000, "Determination of crash-relevant material parameters by dynamic tensile tests," *Steel Research*, 71, pp. 173-178.
- [35] Beynon, N. D., Oliver, S., Jones, T. B., and Fournalis, G., 2005, "Tensile and work hardening properties of low carbon dual phase strip steels at high strain rates," *Materials Science and Technology*, 21, pp. 771-778.
- [36] Beynon, N. D., Jones, T. B., and Fournalis, G., 2005, "Effect of high strain rate deformation on microstructure of strip steels tested under dynamic tensile conditions," *Materials Science and Technology*, 21, pp. 103-112.
- [37] Huh, H., Kim, S. B., Song, J. H., and Lim, J. H., 2008, "Dynamic tensile characteristics of TRIP-type and DP-type steel sheets for an auto-body," *International Journal of Mechanical Sciences*, 50, pp. 918-931.
- [38] Tarigopula, V., Hopperstad, O. S., Langseth, M., Clausen, A. H., and Hild, F., 2008, "A study of localisation in dual phase high-strength steels under dynamic loading using digital image correlation and FE analysis," *International Journal of Solids and Structures*, 45, pp. 601-619.
- [39] Yu, H., Guo, Y., and Lai, X., 2009, "Rate-dependent behavior and constitutive model of DP600 steel at strain rate from 10^{-4} to 10^3 s $^{-1}$," *Materials and Design*, 30, pp. 2501-2505.
- [40] Kim, S. B., Huh, H., Bok, H. H., and Moon, M. B., 2011, "Forming limit diagram of auto-body steel sheets for high-speed sheet metal forming," *Journal of Materials Processing Technology*, 211, pp. 851-862.
- [41] Wang, W., Li, M., He, C., Wei, X., Wang, D., and Du, H., 2013, "Experimental study on high strain rate behavior of high strength 600-1000MPa dual phase steels and 1200MPa fully martensitic steels," *Materials and Design*, 47, pp. 510-521.
- [42] Nakazima, K., Kikuma, T., and Hasuka, K., 1968, "Study on the formability of steel sheets," *Yawata Technical Report*, pp. 8517-8530.
- [43] Golovashchenko, S. F., Gillard, A. J., Cedar, D. A., and Ilinich, A. M., 2009, "Electrohydraulic forming tool," *US Patent 7516634*, Ford Global Technologies, LLC.
- [44] Lis, J., Lis, A. K., and Kolan, C., 2005, "Processing and properties of C-Mn steel with dual-phase microstructure," *Journal of Materials Processing Technology*, 162-163, pp. 350-354.
- [45] Waterschoot, T., Cooman, B. C., and Vanderschueren, D., 2001, *Ironmaking and steelmaking*.
- [46] Callister, W. D., 2007, *Materials Science and Engineering*, John Wiley & Sons, Inc., US.
- [47] Klaar, H. J., El-Sesy, I. A., and Hussein, A. H. A., 1990, "Microstructure and properties of a C-Mn-Si-dual-phase steel," *Steel Research* 61(2), pp. 85-92.
- [48] Park, K. S., Park, K. T., Lee, D. L., and C. S. Lee, 2007, "Effect of heat treatment path on the cold formability of drawn dual-phase steels," *Materials Science and Engineering A* 449-451, pp. 1135-1138.

- [49] Kuang, S., Kang, Y. L., Yu, H., and Liu, R. D., 2008, "Simulation of Intercritical austenization of a C-Mn cold rolled dual phase steel," *Materials Science Forum*, 575-578, pp. 1062-1069.
- [50] Sun, S., and Pugh, M., 2000, "Manganese partitioning in dual-phase steel during annealing," *Materials Science and Engineering A*, 276(1-2), pp. 167-174.
- [51] Erdogan, M., 2003, "Effect of austenite dispersion on phase transformation in dual phase steel," *Scripta Materialia*, 48(5), pp. 501-506.
- [52] Ajmal, M., Tindyala, M. A., and Priestner, R., 2009, "Effect of controlled rolling on the martensitic hardenability of dual phase steel," *International Journal of Minerals, Metallurgy, and Materials*, 16(2), pp. 165-169.
- [53] Llewellyn, D. T., and Hudd, R. C., 1998, *Steels: metallurgy and Applications*, Butterworth Heinemann.
- [54] Li, L., Ding, H., Du, L., Wen, J., Song, H., and Zhang, P., 2008, "Influence of Mn content and hot deformation on transformation behavior of C-Mn steels," *Journal of Iron and Steel Research*, 15(2), pp. 51-55.
- [55] Rashid, M. S., 1981, "Dual phase steels," *Annual Review of Materials Science*, 11, pp. 245-266.
- [56] Thomas, G., and Koo, J. Y., 1979, *Structure and Properties of Dual-Phase Steels*, R. A. Kot, and J. W. Morris, eds., TMS-AIME, pp. 183-201.
- [57] Smallman, R. E., and Bishop, R. J., 1999, *Modern physical metallurgy and materials engineering: science, process, applications*, Butterworth-Heinemann.
- [58] Zeytin, H. K., Kubilay, C., and Aydin, H., 2008, "Investigation of dual phase transformation of commercial low alloy steels," *Materials Letters*, 62(17-18), pp. 2651-2653.
- [59] Leslie, W. C., 1981, *The physical metallurgy of steels*, Tech Books.
- [60] Gladman, T., 2002, *The physical metallurgy of microalloyed steels*, The Institute of Materials.
- [61] Pickering, F. B., 1978, *Physical metallurgy and the design of steels*, Applied Science Publishers, London.
- [62] Andrews, K. W., 1965, *The Journal of the Iron and Steel Institute*, 203, p. 271.
- [63] Smith, W. F., 1996, *Structure and properties of engineering alloys*, McGraw-Hill Inc.
- [64] Majka, T. F., Matlock, D. K., and Krauss, G., 2002, "Development of microstructural banding in low-alloy steel with simulated Mn segregation," *Metallurgical and Materials Transactions A*, 33(6), pp. 1627-1637.
- [65] Caballero, F. G., García-Junceda, A., Capdevila, C., and Andrés, C. G. D., 2006, "Evolution of microstructural banding during the manufacturing process of DP steels," *Materials Transactions*, 47(9), pp. 2269-2276.
- [66] Fisher, R. M., Speich, G. R., Cuddy, L. J., and Hu, H., "Physical Chemistry in Metallurgy," *Proc. Proceedings of the Darken Conference*, pp. 463-488.
- [67] Park, Y. J., Coldren, A. P., and Morrow, J. W., 1981, "Effect of martensite bands and elongated manganese sulfide inclusions on the formability of dual-phase steels," In *Fundamentals of Dual-Phase Steels*, R. A. Kot, and B. L. Bramfitt, eds., TMS-AIME, pp. 485-497.
- [68] Pickering, F. B., 1992 *Constitution and properties of steels*, Weinheim, Germany.

- [69] Gladman, T., 1997 The physical metallurgy of microalloyed steels, The Institute of Metals, London.
- [70] Dieter, G. E., 1986, Mechanical metallurgy, McGraw-Hill.
- [71] Hertzberg, R. W., 1996, Deformation and fracture mechanics of engineering materials, John Wiley & Sons.
- [72] Hall, E. O., "The deformation and Aging of Mild Steel: III Discussion of Results," Proc. Proceedings of the Physical Society of London, pp. 747-753.
- [73] Petch, N. J., 1953, "The cleavage strength of polycrystals," Journal of the Iron and Steel Institute, 174, pp. 25-28.
- [74] Chang, P. H., and Preban, A. G., 1985, "The effect of ferrite grain size and martensite volume fraction on the tensile properties of dual phase steel," Acta Metallurgica, 33(5), pp. 897-903.
- [75] Jiang, Z., Guan, Z., and Lian, J., 1995, "Effects of microstructural variables on the deformation behaviour of dual-phase steel," Materials Science and Engineering A, 190(1-2), pp. 55-64.
- [76] Korzekwa, D. A., Matlock, D. K., and Krauss, G., 1984, "Dislocation substructure as a function of strain in a dual-phase steel," Metallurgical and Materials Transactions A, 15(6), pp. 1221-1228.
- [77] Fink, W. L., and Campbell, E. D., 1926, "Influence of heat treatment and carbon content on the structure of pure iron carbon alloys," Transactions of the American Society for Steel Treating, 9, pp. 717-752.
- [78] Bain, E. C., and Paxton, H. W., 1966, Alloying elements in steel, ASM, Metals Park, Ohio.
- [79] Owen, W. S., Wilson, E. A., and Bell, T., 1965, High strength materials, John Wiley & Sons, New York.
- [80] Krauss, G., 1978, Hardenability concepts with applications to steel, AIME.
- [81] Krauss, G., 1990, Microstructures, processing, and properties of steels, properties and selection: irons, steels, and high-performance alloys, ASM Handbook, 1, p. 126.
- [82] Bag, A., Ray, K. K., and Dwarakadasa, E. S., 1999, "Influence of martensite content and morphology on tensile and impact properties of high-martensite dual-phase steels," Metallurgical and Materials Transactions A, 30(5), pp. 1193-1202
- [83] Byun, T. S., and Kim, I. S., 1993, "Tensile properties and inhomogeneous deformation of ferrite-martensite dual-phase steels," Journal of Materials Science, 28, pp. 2923-2932.
- [84] Gunduz, S., 2009, "Effect of chemical composition, martensite volume fraction and tempering on tensile behaviour of dual phase steels," Materials Letters, 63, pp. 2381-2383.
- [85] Jiang, Z., Guan, Z., and Lian, J., 1993, "The relationship between ductility and material parameters for dual-phase steel," Journal of Materials Science, 28, pp. 1814-1818.
- [86] Tomota, Y., 1987, "Effects of morphology and strength of martensite on cyclic deformation behaviour in dual-phase steels," Materials Science and Technology 3(6), pp. 415-421.

- [87] Tomita, Y., 1990, "Effect of morphology of second-phase martensite on tensile properties of Fe-0.1C dual phase steels," *Journal of Materials Science*, 25, pp. 5179-5184.
- [88] He, X. J., Terao, N., and Berghezan, A., 1984, "Influence of martensite morphology and its dispersion on mechanical properties and fracture mechanisms of Fe-Mn-C dual phase steels," *Metal science* 18(7), pp. 367-373.
- [89] Sarwar, M., and Priestner, R., 1996, "Influence of ferrite-martensite microstructural morphology on tensile properties of dual-phase steel," *Journal of Materials Science*, 31, pp. 2091-2095.
- [90] K.L. Kim, C. G. L., S. Lee, 1998, "Effects of martensite morphology on dynamic torsional behavior in dual phase steels," *Scripta Materialia*, 38, pp. 27-32.
- [91] Das, D., and Chattopadhyay, P. P., 2009, "Influence of martensite morphology on the work-hardening behavior of high strength ferrite-martensite dual-phase steel," *Journal of Materials Science*, 44, pp. 2957-2965.
- [92] Ahmad, E., Manzoor, T., Ziai, M. M. A., and Hussain, N., 2012, "Effect of martensite morphology on tensile deformation of dual-phase steel," *Journal of Materials Engineering and Performance*, 21, pp. 382-387.
- [93] Erdogan, M., and Tekeli, S., 2002, "The effect of martensite particle size on tensile fracture of surface-carburised AISI 8620 steel with dual phase core microstructure," *Materials and Design*, 23(7), pp. 597-604.
- [94] Ashby, M. F., 1970, "Deformation of plastically non-homogeneous materials," *Philosophical Magazine*, 21(170), pp. 399-424.
- [95] Fleck, N. A., Muller, G. M., Ashby, M. F., and Hutchinson, J. W., 1994, "Strain gradient plasticity: Theory and experiment," *Acta Metallurgica Et Materialia*, 42(2), pp. 475-487.
- [96] Calcagnotto, M., Ponge, D., Demir, E., and Raabe, D., 2010, "Orientation gradients and geometrically necessary dislocations in ultrafine grained dual-phase steels studied by 2D and 3D EBSD," *Materials Science and Engineering A*, 527(10-11), pp. 2738-2746.
- [97] Bourell, D. L., and Rizk, A., 1983, "Influence of martensite transformation strain on the ductility of dual-phase steels," *Acta Metallurgica*, 31(4), pp. 609-617.
- [98] Mondal, D. K., and Dey, R. M., 1992, "Effect of grain size on the microstructure and mechanical properties of a C-Mn-V dual-phase steel," *Materials Science and Engineering*, 149, pp. 173-181.
- [99] Liedl, U., Taint, S., and Werner, E. A., 2002, "An unexpected feature of the stress-strain diagram of dual-phase steel," *Computational Materials Science*, 25, pp. 122-128.
- [100] Liang, X., Li, J., and Peng, Y. H., 2008, "Effect of water quench process on mechanical properties of cold rolled dual phase steel microalloyed with niobium," *Materials Letters*, 69, pp. 327-329.
- [101] Korzekwa, D. A., Lawson, R. D., Matlock, D. K., and Krauss, G., 1980, "Consideration of models describing the strength and ductility of dual-phase steels," *Scripta metallurgica*, 14(9), pp. 1023-1028.
- [102] Chawla, K. K., Rios, P. R., and Guimarães, J. R. C., 1983, "Fractography of a dual phase steel," *Journal of Materials Science Letters*, 2(3), pp. 94-98.

- [103] Jardim, O. R., Longo, W. P., and Chawla, K. K., 1984, "Fracture behavior of a tempered dual phase steel," *Metallography*, 17(2), pp. 123-130.
- [104] Szewczyk, A. F., and Gurland, J., 1982, "Study of the deformation and fracture of a dual-phase steel," *Metallurgical Transactions A*, 13A(10), pp. 1821-1826.
- [105] Erdogan, M., 2002, "The effect of new ferrite content on the tensile fracture behaviour of dual phase steels," *Journal of Materials Science*, 37, pp. 3623-3630.
- [106] Shen, H. P., Lei, T. C., and Liu, J. Z., 1986, "Microscopic deformation behaviour of martensitic–ferritic dual-phase steels," *Materials Science and Technology*, 2(1), pp. 28-33.
- [107] Su, Y. L., and Gurland, J., 1987, "Strain partition, uniform elongation and fracture strain in dual-phase steels," *Materials Science and Engineering*, 95C, pp. 151-165.
- [108] Mazinani, M., and Poole, W. J., 2007, "Deformation behaviour of martensite in a low-carbon dual-phase steel," *Advanced Materials Research* 15-17, pp. 774-779.
- [109] Sakaki, T., Sugimoto, K., and Fukuzato, T., 1983, "Role of internal stress for continuous yielding of dual-phase steels," *Acta Metallurgica*, 31(10), pp. 1737-1746.
- [110] Peng-Heng, C., and Preban, A. G., 1985, "The effect of ferrite grain size and martensite volume fraction on the tensile properties of dual phase steel," *Acta Metallurgica*, 33(5), pp. 897-903.
- [111] Cottrell, A. H., and Bilby, B. A., "Dislocation theory of yielding and strain ageing of iron," *Proc. Proceedings of the Physical Society*, pp. 49-62.
- [112] Gerbase, J., Embury, J. D., and Hobbs, R. M., "Structure and properties of dual-phase steels," *Proc. TMS-AIME*, R. A. Kot, and J. W. Morris, eds., pp. 118-144.
- [113] Pickering, F. B., 1981, *Advances in the physical metallurgy and application of steels*, The Metal Society.
- [114] Crussard, C., 1953, "Relationship between exact form of tensile curves of metals and accompanying changes in their structure," *Revue de Métallurgie*, 50, pp. 697-710.
- [115] Jaoul, B., 1957, "Etude de la forme des courbes de deformation plastique," *Journal of the Mechanics and Physics of Solids*, 5, pp. 95-114.
- [116] Nam, W. J., and Bae, C. M., 1999, "Microstructural evolution and its relation to mechanical properties in a drawn dual-phase steel," *Journal of Materials Science*, 34, pp. 5661-5668.
- [117] Matlock, D. K., Krauss, G., Famos, L. F., and Huppi, G. S., 1979, "A correlation of processing variables with deformation behavior of dual-phase steels," *Structure and Properties of Dual-Phase Steels*, R. A. Kot, and J. W. Morris, eds., TMS-AIME, pp. 62-90.
- [118] Cribb, W. R., and Rigsbee, J. M., "Work hardening behaviour and its relationship to the microstructure and mechanical properties of dual-phase steels," *Proc. Structure and properties of dual-phase steels*, R. A. Kot, and J. W. Morris, eds., TMS-AIME, pp. 91-117.
- [119] Shirasawa, H., and Thomson, J. G., 1987, "Effect of hot band microstructure on strength and ductility of cold rolled dual phase steel," *Transactions of the Iron and Steel Institute of Japan*, 27(5), pp. 360-365.
- [120] Steinbrunner, D. L., Matlock, D. K., and Krauss, G., 1988, "Void formation during tensile testing of dual phase steels," *Metallurgical and Materials Transactions A*, 19A, pp. 579-589.

- [121] Han, S. K., and Margolin, H., 1989, "Void formation, void growth and tensile fracture of plain carbon steel and a dual-phase steel," *Materials Science and Engineering A*, 112 (C), pp. 133-141.
- [122] Ahmad, E., Manzoor, T., Ali, K. L., and Akhter, J. I., 2000, "Effect of microvoid formation on the tensile properties of dual-phase steel," *Journal of Materials Engineering and Performance*, 9(3), pp. 306-310.
- [123] Avramovic-Cingara, G., Saleh, C. A. R., Jain, M. K., and Wilkinson, D. S., 2009, "Void nucleation and growth in dual-phase steel 600 during uniaxial tensile testing," *Metallurgical and Materials Transactions A* 40A, pp. 3117-3127.
- [124] Mairea, E., Bouazizb, O., Michielc, M. D., and Verdua, C., 2008, "Initiation and growth of damage in a dual-phase steel observed by X-ray microtomography," *Acta Materialia*, 56(18), pp. 4954-4964.
- [125] Mazinani, M., and Poole, W. J., 2007, "Effect of martensite plasticity on the deformation behavior of a low-carbon dual-phase steel," *Metallurgical and Materials Transactions A*, 38A, pp. 328-339.
- [126] Ray, R. K., 1984, "Tensile fracture of a dual-phase steel," *Scripta Metallurgica*, 18(11), pp. 1205-1209.
- [127] Uggowitz, P., and Stüwe, H. P., 1982, "The tensile fracture of ferritic-martensitic carbon steels," *Materials Science and Engineering*, 55(2), pp. 181-189.
- [128] Nakagawa, A. H., and Thomas, G., 1985, "Microstructure-mechanical property relationships of dual-phase steel wire," *Metallurgical Transactions A*, 16(5), pp. 831-840.
- [129] Westphal, M., McDermid, J. R., Boyd, J. D., and Embury, J. D., 2010, "Novel thermal processing of dual phase steels II – work hardening and fracture mechanisms," *Canadian Metallurgical Quarterly*, 49, pp. 91-98.
- [130] Avramovic-Cingara, G., Ososkov, Y., Jain, M. K., and Wilkinson, D. S., 2009, "Effect of martensite distribution on damage behaviour in DP600 dual phase steels," *Materials Science and Engineering A*, 516, pp. 7-16.
- [131] Sun, X., Choi, K. S., Soulami, A., Liu, W. N., and Khaleel, M. A., 2009, "On key factors influencing ductile fractures of dual phase steels," *Materials Science and Engineering A*, 526(1-2), pp. 140-149.
- [132] Bayram, A., Uğuz, A., and Ula, M., 1999, "Effects of microstructure and notches on the mechanical properties of dual-phase steels," *Materials Characterization*, 43(4), pp. 259-269.
- [133] Liao, C., Sun, F., and Lan, F., 1979, "An investigation of quasi-cleavage fracture in steel," *Acta Metallurgica Sinica*, 15(2), pp. 259-265.
- [134] Mynors, D. J., and Zhang, B., 2002, "Applications and capabilities of explosive forming," *Journal of Materials Processing Technology*, 125-126, pp. 1-25.
- [135] Daehn, G., 2006, *High-velocity metal forming*, ASM International.
- [136] Benedict, G. F., 1987, *Nontraditional manufacturing processes*, Marcel Dekker Inc.
- [137] Amstead, B. H., Ostwald, P. F., and Begman, M. L., 1987, *Manufacturing processes*, John Wiley and Sons.
- [138] Groover, M. P., 2007, *Fundamentals of modern manufacturing: Materials, processes, and systems*, John Wiley and Sons.

- [139] Kalpakjian, S., and Schmid, S. R., 2006, Manufacturing engineering and technology, Pearson Education Inc.
- [140] Early, C., and Dow, W. G., "Experimental studies and applications of explosive pressures produced by sparks in confined channels," Proc. A.I.E.E.
- [141] Yutkin, L. A., 1950, Elektrogidravlichesky effect, U.S.S.R. State Science and Technology Press for Machine Construction, Moscow.
- [142] Kegg, R. L., 1964, "A study of energy requirements for electrical discharge metal forming," ASME Transaction, 86B, pp. 127-133.
- [143] Kirk, J. W., 1962, "Impulse forming by electrical discharge method," Sheet Metal Industries, 39, pp. 533-540.
- [144] Duncan, J. L., and Johnson, W., 1964, "Comparison of the behaviour of different sheet metals formed by the underwater spark discharge method," Proceedings of the Institution of Mechanical Engineers, 179, pp. 234-239.
- [145] Martin, E. A., 1960, "Experimental investigation of a high energy density, high pressure arc plasma," Journal of Applied Physics, 31, pp. 252-267.
- [146] Bazhenova, T. V., and Soloukhin, R. I., 1961, Pressure field occurring in water during an electrical discharge, Pergamon Press.
- [147] Wakil, S. D. E., 1998, Processes and designed for manufacturing, PWS Publishing Company.
- [148] Rohatgi, A., Stephens, E. V., Davies, R. W., Smith, M. T., Soulami, A., and Ahzi, S., 2012, "Electro-hydraulic forming of sheet metals: Free-forming vs. conical-die forming," Journal of Materials Processing Technology, 212 pp. 1070-1079.
- [149] Sarraf, I. S., Samei, J., Green, D., and Golovashchenko, S., "Strain hardening in dual phase steel sheets formed into a conical die using an electrohydraulic forming process," Proc. Materials Science and Technology Conference and Exhibition (MS&T'13).
- [150] Bambach, M., Hirt, G., and Junk, S., April 2003, "Modelling and experimental evaluation of the incremental CNC sheet metal forming process," VII International Conference on Computational Plasticity, COMPLAS 2003Barcelona
- [151] Kim, T. J., and Yang, D. Y., 2000, "Improvement of formability for the incremental sheet metal forming process," International Journal of Mechanical Sciences, 42(7), pp. 1271-1286.
- [152] Iseki, H., and Kumon, H., 1994, "Forming limit of incremental sheet metal stretch forming using spherical rollers," Journal of the Japan Society for Technology of Plasticity, 35(406), pp. 1336-1341.
- [153] Buffa, G., Campanella, D., and Fratini, L., 2013, "On the improvement of material formability in SPIF operation through tool stirring action," International Journal of Advanced Manufacturing Technology, 66, pp. 1343-1351.
- [154] Golovashchenko, S. F., Bessonov, N. M., and Ilinich, A. M., 2011, "Two-step method of forming complex shapes from sheet metal," Journal of Materials Processing Technology, 211, pp. 875-885.
- [155] Hasebe, T., Imaida, Y., and Yoshida, S., 1996, "Focusing of shock wave by underwater discharge - On nonlinear reflection and focusing effect," Journal of the Society of Materials Science, 45, pp. 1151-1156.

- [156] Manjoine, M. J., 1944, "Influence of rate of strain and temperature on yield stresses of mild steel," *Journal of Applied Mechanics*, 66, pp. A211-A218.
- [157] Pearson, J., and Rinehart, J. S., 1952, "Deformation and fracturing of thick-walled steel cylinders under explosive attack," *Journal of Applied Physics*, 23, pp. 434-441.
- [158] Krasikov, K. I., Veretennikov, S. V., Novobratskii, R. L., Edneral, N. V., Perper, F. A., Polyak, S. M., Umanskii, Y. S., and Epshtein, G. N., 1967, "Structure and mechanical properties of materials after hydroexplosive forming," *Soviet Materials Science*, 3, pp. 512-514.
- [159] Wood, W. W., 1967, "Experimental mechanics at velocity extremes -Very high strain rates - Study covers tensile and compression specimens, spherical bulging and cylindrical bulging for a wide variety of materials," *Experimental Mechanics*, 10, pp. 441-446.
- [160] Johnson, W., Poynton, A., Singh, H., and Travis, F. W., 1966, "Experiments in the underwater explosive stretch forming of clamped circular blanks," *International Journal of Mechanical Sciences*, 8, pp. 237-242.
- [161] Bakhtar, F., and Austin, E. R., 1965, "Relative economics of conventional and high strain-rate forming," *International Journal of Machine Tool Design and Research*, 5, pp. 139-154.
- [162] Dusek, F., 1970, "Plastic deformation at high strain rates," *Czechoslovak Journal of Physics*, 20, pp. 776-789.
- [163] Steichen, J. M., 1973, "High strain rate tensile properties of AISI Type 304 stainless steel," *Journal of Engineering Materials and Technology*, 95, pp. 182-185.
- [164] Winkler, S., Thompson, A., Salisbury, C., Worswick, M., Riemsdijk, I., and Mayer, R., 2008, "Strain rate and temperature effects on the formability and damage of advanced high-strength steels," *Metallurgical and Materials Transactions A*, 39A, pp. 1350-1358.
- [165] Seth, M., Vohnout, V. J., and Daehn, G. S., 2005, "Formability of steel sheet in high velocity impact," *Journal of Materials Processing Technology*, 168, pp. 390-400.
- [166] Lindholm, U. S., and Yeakley, L. M., 1965, "Dynamic deformation of single and polycrystalline aluminium," *Journal of the Mechanics and Physics of Solids*, 13, pp. 41-53.
- [167] Tamhane, A., Altynova, M., and Daehn, G. S., 1996, "Effect of sample size on ductility in electromagnetic ring expansion," *Scripta Metallurgica et Materialia*, 34, pp. 1345-1350.
- [168] Safari, M., Hosseinipour, S. J., and Azodi, H. D., in press, "An investigation into the effect of strain rate on forming limit diagram using ductile fracture criteria," *Meccanica*, pp. 1-9.
- [169] Clyens, S., and Campbell, J. D., 1975, *Behaviour of copper and lead-tin eutectic in torsion at high strain rates*, The Institute of Physics, London.
- [170] Regazzoni, G., and Montheillet, F., 1984, *Influence of strain rate on the flow stress and ductility of copper and tantalum at room temperature*, The Institute of Physics, London.
- [171] Ramezani, M., Ripin, Z. M., and Ahmad, R., 2010, "Plastic bulging of sheet metals at high strain rates," *International Journal of Advanced Manufacturing Technology*, 48, pp. 847-858.

- [172] Giannotta, J. C., Regazzoni, G., and Montheillet, F., 1985, "Deformation of copper at high strain rates," *Journal de Physique*, 46, pp. C5-49.
- [173] Takeda, N., and Kobayshi, A., 1992, *Shock wave and high strain rate phenomena in materials*, Marcel Dekker Inc, New York.
- [174] Shang, J., Wilkerson, L., and Hatkevich, S., 2011, "Hemming of aluminum alloy sheets using electromagnetic forming," *Journal of Materials Engineering and Performance*, 20, pp. 1370-1377.
- [175] Oliveira, D. A., Worswick, M. J., Finn, M., and Newman, D., 2005, "Electromagnetic forming of aluminum alloy sheet: Free-form and cavity fill experiments and model," *Journal of Materials Processing Technology*, 170, pp. 350-362.
- [176] Imbert, J. M., Winkler, S. L., Worswick, M. J., Oliveira, D. A., and Golovashchenko, S., 2005, "The effect of tool-sheet interaction on damage evolution in electromagnetic forming of aluminum alloy sheet," *Journal of Engineering Materials and Technology*, 127, pp. 145-153.
- [177] Balanethiram, V. S., and Daehn, G. S., 1992, "Enhanced formability of interstitial free iron at high strain rates," *Scripta Metallurgica et Materiala*, 27, pp. 1783-1788.
- [178] Balanethiram, V. S., and Daehn, G. S., 1994, "Hyperplasticity: Increased forming limits at high workpiece velocity," *Scripta Metallurgica et Materiala*, 30, pp. 515-520.
- [179] Balanethiram, V. S., Hu, X., Altynova, M., and Daehn, G. S., 1994, "Hyperplasticity: Enhanced formability at high rates," *Journal of Materials Processing Technology*, 45, pp. 595-600.
- [180] Rohatgi, A., Stephens, E. V., Soulami, A., Davies, R. W., and Smith, M. T., 2011, "Experimental characterization of sheet metal deformation during electro-hydraulic forming," *Journal of Materials Processing Technology*, 211, pp. 1824-1833.
- [181] *Metals Handbook*, 1979, 9th edition, 2, ASM Metals Park, OH, 183.
- [182] Kohara, S., Katsuta, M., Aoki, K., and Suzuki, K., 1984, "Advanced Technology of Plasticity," K. Lange, ed., Springer-Verlag, p. 765.
- [183] Dariani, B. M., Liaghat, G. H., and Gerdooei, M., 2009, "Experimental investigation of sheet metal formability under various strain rates," *Journal of Engineering Manufacture*, 223, pp. 703-712.
- [184] Jie, M., Cheng, C. H., Chan, L. C., and Chow, C. L., 2009, "Forming limit diagrams of strain-rate-dependent sheet metals," *International Journal of Mechanical Sciences*, 51, pp. 269-275.
- [185] Rajendran, A. M., and Fyfe, I. M., 1982, "Inertia effects on the ductile failure of thin rings," *Journal of Applied Mechanics*, 49, pp. 31-36.
- [186] Regazzoni, G., Johnson, J. N., and Follansbee, P. S., 1986, "Theoretical study of dynamic tensile test," *Journal of Applied Mechanics, Transactions ASME*, 53, pp. 519-528.
- [187] Hu, X., and Daehn, G. S., 1996, "Effect of velocity on flow localization in tension," *Acta Materialia*, 44, pp. 1021-1033.
- [188] Hollomon, J. H., 1945, "Tensile Deformation," *Transaction AIME*, 162, pp. 269-290.
- [189] Johnson, G. R., and Cook, W. H., "A constitutive model and data for metals subjected to large strains, high strain rates, and high temperatures," *Proc. Proceedings 7th International Symposium on Ballistics*, pp. 541-547.

- [190] Zerilli, F. J., and Armstrong, R. W., 1987, "Dislocation mechanics based constitutive relations for material dynamics calculations," *Journal of Applied Physics*, 61, pp. 1816-1825.
- [191] Kleemola, H. J., and Ranta-Eskola, A. J., 1979, "Effect of strain rate and deformation temperature on the strain hardening of sheet steel and brass in uniaxial tension," *Sheet Metal Industries*, 56, pp. 1046-1057.
- [192] Hashmi, M. S. J., 1980, "Strain rate sensitivity of mild steel at room temperature and strain rates of up to 10^5 s^{-1} ," *Journal of Strain Analysis for Engineering Design*, 15, pp. 201-207.
- [193] Wagoner, R. H., 1981, "A new description of strain-rate sensitivity," *Scripta Metallurgica et Materiala*, 15, pp. 1135-1137.
- [194] Wagoner, R. H., and Wang, N. M., 1983, "Operant strain-rate sensitivity during tensile necking," *Metallurgical Transactions A*, 14, pp. 2395-2406.
- [195] Follansbee, P. S., and Kocks, U. F., 1988, "A constitutive description of the deformation of copper based on the use of the mechanical threshold stress as an internal state variable," *Acta Metallurgica*, 36, pp. 81-93.
- [196] Campbell, J. D., 1967, "Plastic instability in rate-dependent materials," *Journal of the Mechanics and Physics of Solids*, 15, pp. 359-370.
- [197] Duncombe, E., 1972, "Plastic instability and growth of grooves and patches in plates or tubes," *International Journal of Mechanical Sciences*, 14, pp. 325-337.
- [198] Ghosh, A. K., 1977, "Tensile instability and necking in materials with strain hardening and strain-rate hardening," *Acta Metallurgica*, 25, pp. 1413-1424.
- [199] Hart, E. W., 1967, "Theory of the tensile test," *Acta Metallurgica*, 15, pp. 351-355.
- [200] Hutchinson, J. W., and Neale, K. W., 1977, "Influence of strain-rate sensitivity on necking under uniaxial tension," *Acta Metallurgica*, 25, pp. 839-846.
- [201] Jonas, J. J., and Baudalet, B., 1977, "Effect of crack and cavity generation on tensile stability," *Acta Metallurgica*, 25, pp. 43-50.
- [202] Jonas, J. J., Holt, R. A., and Coleman, C. E., 1976, "Plastic stability in tension and compression," *Acta Metallurgica*, 24, pp. 911-918.
- [203] Nichols, F. A., 1980, "Plastic instabilities and uniaxial tensile ductilities," *Acta Metallurgica*, 28, pp. 663-673.
- [204] Chung, K., and Wagoner, R. H., 1988, "Effects of work-hardening and rate sensitivity on the sheet tensile test," *Metallurgical Transactions A*, 19, pp. 293-300.
- [205] Lin, I. H., Hirth, J. P., and Hart, E. W., 1981, "Plastic instability in uniaxial tension tests," *Acta Metallurgica*, 29, pp. 819-827.
- [206] Semiatin, S. L., Ghosh, A. K., and Jonas, J. J., 1985, "A simplified numerical analysis of the sheet tensile test," *Metallurgical Transactions A*, 16, pp. 2291-2298.
- [207] El-Magd, E., 1997, "Influence of strain rate on ductility of metallic materials," *Steel Research*, 68, pp. 67-71.
- [208] Lee, W. S., Lin, C. F., and Liu, T. J., 2007, "Impact and fracture response of sintered 316L stainless steel subjected to high strain rate loading," *Materials Characterization*, 58, pp. 363-370.

- [209] Baron, H. G., and Henn, R. H., 1964, "Spring-back and metal flow in forming shallow dishes by explosives," *International Journal of Mechanical Sciences*, 6, pp. 435-444.
- [210] Taylor, J. W., Harlow, F. H., and Amsden, A. A., 1978, "Dynamic plastic instabilities in stretching plates and shells," *Journal of Applied Mechanics, Transactions ASME*, 45, pp. 105-110.
- [211] Fressengeas, C., and Molinari, A., 1985, "Inertia and thermal effects on the localization of plastic flow," *Acta Metallurgica*, 33, pp. 387-396.
- [212] Fyfe, I. M., and Rajendran, A. M., 1980, "Dynamic pre-strain and inertia effects on the fracture of metals," *Journal of the Mechanics and Physics of Solids*, 28, pp. 17-26.
- [213] Hu, X., Wagoner, R. H., Daehn, G. S., and Ghosh, S., 1994, "The effect of inertia on tensile ductility," *Metallurgical and Materials Transactions A*, 25, pp. 2723-2735.
- [214] Needleman, A., 1991, *The effect of material inertia on neck development*, AM Press, Ann Arbor, US.
- [215] Shenoy, V. B., and Freund, L. B., 1999, "Necking bifurcations during high strain rate extension," *Journal of the Mechanics and Physics of Solids*, 47, pp. 2209-2233.
- [216] Altynova, M., Hu, X., and Daehn, G. S., 1996, "Increased ductility in high velocity electromagnetic ring expansion," *Metallurgical and Materials Transactions A*, 27A, pp. 1837-1844.
- [217] Tamhane, A. A., Altynova, M., and Daehn, G. S., 1996, "Effect of sample size on ductility in electromagnetic ring expansion," *Sripta Materialia*, 34(8), pp. 1345-1350.
- [218] Priem, D., Marya, S., and Racineux, G., 2007, "On the forming of metallic parts through electromagnetic and electrohydraulic processing," *Advanced Materials Research*, 15-17, pp. 655-660.
- [219] Oliveira, D. A., 2002, "Electromagnetic forming of aluminum alloy sheet: experiment and model," *Masters of Applied Science*, University of Waterloo.
- [220] Marchand, A., and Duffy, J., 1988, "An experimental study of the formation process of adiabatic shear bands in a structural steel," *Journal of the Mechanics and Physics of Solids*, 36(3), pp. 251-283.
- [221] Schoenfeld, S. E., and Wright, T. W., 2003, "A failure criterion based on material instability," *International Journal of Solids and Structures*, 40(12), pp. 3021-3037.
- [222] Odeshi, A. G., Al-Ameeri, S., and Bassim, M. N., 2005, "Effect of high strain rate on plastic deformation of a low alloy steel subjected to ballistic impact," *Journal of Materials Processing Technology* 162-163, pp. 385-391.
- [223] Zurek, A. K., 1994, "The study of adiabatic shear band instability in a pearlitic 4340 steel using a dynamic punch test," *Metallurgical and Materials Transactions A*, 25(11), pp. 2483-2489.
- [224] Meyers, M. A., and Wittman, C. L., 1990, "Effect of metallurgical parameters on shear band formation in low-carbon (approx. 0.20 wt pct) steels," *Metallurgical transactions A*, 21A(12), pp. 3153-3164.
- [225] Meyers, M. A., Xu, Y. B., Xue, Q., Pérez-Prado, M. T., and McNelley, T. R., 2003, "Microstructural evolution in adiabatic shear localization in stainless steel," *Acta Materialia*, 51(5), pp. 1307-1325.

- [226] Orowan, E., 1940, "Problems of plastic gliding," Proceedings of the Physical Society, 52, pp. 8-22.
- [227] Gupta, Y. M., G.E. Duvall, and G.R. Fowles, 1975, "Dislocation mechanisms for stress relaxation in shocked LiF," Journal of Applied Physics, 46, pp. 532-546.
- [228] Meyers, M. A., and Chawla, K. K., 1999, Mechanical Behaviour of Materials, Prentice Hall, New Jersey.
- [229] Hahn, G. T., 1962, "A model for yielding with special reference to the yield-point phenomena of iron and related bcc metals," Acta Metallurgica, 10, pp. 727-738.
- [230] Campbell, J. D., and Ferguson, W. G., 1970, "The temperature and strain-rate dependence of the shear strength of mild steel," Philosophical Magazine, 21(169), pp. 63-82.
- [231] International, A., 2010, "Standard test methods for determining average grain size using semiautomatic and automatic image analysis."
- [232] International, A., 2011, "Standard test method for Knoop and Vickers hardness of materials."
- [233] International, A., 2005, "Standard test methods for determination of carbon, sulfur, nitrogen, and oxygen in steel, iron, nickel, and cobalt alloys by various combustion and fusion techniques."
- [234] International, A., 2005, "Standard guide for direct current plasma atomic emission spectrometry analysis."
- [235] International, A., 2005, "Standard practice for describing and specifying inductively-coupled plasma atomic emission spectrometers."
- [236] Golovashchenko, S. F., Gillard, A. J., and Mamutov, A. V., 2013, "Formability of dual phase steels in electrohydraulic forming," Journal of Materials Processing Technology, 213, pp. 1191-1212.
- [237] Hopperstad, O. S., Borvik, T., Langseth, M., Labibes, K., and Albertini, C., 2003, "On the influence of stress triaxiality and strain rate on the behaviour of a structural steel Part I. Experiments," European Journal of Mechanics A/Solids, 22, pp. 1-13.
- [238] Noble, J. P., Goldthorpe, B. D., Church, P., and Harding, J., 1999, "The use of the Hopkinson bar to validate constitutive relations at high rates of strain," Journal of the Mechanics and Physics of Solids, 47, pp. 1187-1206.
- [239] Fultz, B., and Howe, J. M., 2013, Transmission electron microscopy and diffractometry of materials, Springer.
- [240] Christian, J. W., and Mahajan, S., 1995, "Deformation twinning," Progress in Materials Science, 39 (1-2), pp. 1-157.
- [241] Kaspar, J., Luft, A., and Skrotzki, W., 2000, "Deformation modes and structure evolution in laser-shock-loaded molybdenum single crystals of high purity," Crystal Research and Technology, 35(4), pp. 437-448.
- [242] Ogata, S., Li, J., and Yip, S., 2005, "Energy landscape of deformation twinning in bcc and fcc metals," Physical Review B, 71(22), p. 224102.
- [243] Frank, F. C., and Jr., W. T. R., 1950, "Multiplication Processes for Slow Moving Dislocations," Physical Review, 79(4), pp. 722-723.
- [244] Koehler, J. S., 1952, "The nature of work-hardening," Physical Review, 86(1), pp. 52-59.

[245] Orowan, E., 1954, Dislocations in metals, American Institute of Mining and Metallurgy Engineering, New York.

[246] Sevillano, J. G., 2008, "Geometrically necessary twins and their associated size effect," Scripta Materialia, 59, pp. 135-138.

VITA AUCTORIS

NAME Javad Samei

PLACE OF BIRTH Tehran, Iran

YEAR OF BIRTH 1983

EDUCATION

B.Sc. Metallurgical and Materials Engineering

Iran University of Science and Technology

2001-2005

M.Sc. Materials Engineering

K.N.Toosi University of Technology

2005-2008